Thesis for the Master's degree in chemistry

Francesca Bleken

The effect of acid strength on the MTO reaction

- ***Conversion of methanol to hydrocarbons over H-SAPO-34 and high silica Chabazite (H-SSZ-13)***

60 study points

DEPARTMENT OF CHEMISTRY
Faculty of mathematics and natural sciences
UNIVERSITY OF OSLO 12/2007

Abstract

The Methanol-to-Olefins (MTO) process for the production of polymer-grade olefins is a possible step in the upgrading of natural gas. The preferred MTO catalyst is the microporous silicoaluminophosphate H-SAPO-34 (CHA topology). In the present work, H-SAPO-34 is compared with H-SSZ-13 which has the same topology and density of acid sites, but is slightly more acidic due to the framework composition. This is a one-parameter study where the effect of acidity on the MTO-process is investigated. Both materials are very similar as catalysts for the conversion of methanol, the effluent and retained hydrocarbons contain mainly the same compounds. It is found that H-SSZ-13 has a lower total conversion capacity than H-SAPO-34. Both catalysts displayed an optimum temperature, but under the same conditions (Weight Hourly Space Velocity=6.2 hr^{-1}) the optimum temperature of H-SSZ-13 (350° C) was 50°C below that of H-SAPO-34 (400° C). The production of retained hydrocarbons was faster in H-SSZ-13, which also produced larger ring compounds than H-SAPO-34 at the same conditions. Upon flushing with He it was possible to discriminate between the active and non-active compounds in the retained material. The more methylated benzenes were the most reactive ones in both catalysts. In H-SAPO-34 at 350° C only penta- and hexamethylbenzene were active, while also tetramethylbenzene was active in H-SSZ-13. When decreasing the temperature to 300°C, tetramethylbenzene was no longer protonated in H-SSZ-13, so it appears that higher acid strength has an effect comparable to increasing the temperature. Changing WHSV had a great impact on the catalyst properties, such as optimum temperature and conversion capacity. Halving WHSV increased the optimum temperature of H-SAPO-34 to 450° C.

A theoretical study of the adsorption of methanol and CO on the acid sites of the two catalysts is also presented in this thesis. Frequency calculations for the adsorption of CO showed that H-SSZ-13 was slightly more acidic than H-SAPO-34, in good agreement with experimental results reported in the literature. The calculated methanol adsorption energies were higher than reported in previous studies, Furthermore, the calculations indicated that methanol tends to point into the cage rather than the 8-rings of the structure. This is not in agreement with studies reported earlier.

Acknowledgements

This thesis is the result of experimental and computational studies performed at the Department of Chemistry at the University of Oslo, 2006-2007. I would like to acknowledge all my supervisors, Prof. Unni Olsbye, Assoc. Prof. Stian Svelle, Assoc. Prof. Morten Bjørgen (NTNU), Prof. Trygve U. Helgaker and Prof. Karl Petter Lillerud, for giving me the chance to follow this project and for all the help and support provided in these 2 years in the catalysis group. Thank you very much for leading me into the world of science and making it fun and interesting. Special thanks to Unni Olsbye for always explaining with a smile. Stian Svelle's presence in the lab has been invaluable, without, I would still be roaming aimlessly around among reactors and GCs. Morten Bjørgen never said no when I had a problem or a question, and always brought chocolate and jokes to the lab. Stian Svelle and Trygve Helgaker allowed me to do calculations during my thesis. I am very grateful that you took the time to explain these wonderful and complicated things to me. Without Karl Petter Lillerud's great lectures in inorganic chemistry I would never have become a chemist.

I want to thank the catalysis group for providing such a nice environment to learn in, especially Kai for always wanting to help when something did not work in the lab. Un ringraziamento particolare va alla mia amichetta Federica, con la quale ho condiviso i molti momenti allegri, pensierosi e frustranti in questa tesi. Sopratutto di pausa :)

Senza le discussioni con Simone sarei ancora indecisa su quale tesi scegliere. Il tuo aiuto, specialmente per i calcoli di questa tesi, è stato inestimabile. Grazie anche per le numerose cene che mi hai preparato e le telefonate in cui mi hai sopportato :)

Ian og Janes evne til å adspre og underholde meg den siste tiden vil jeg alltid huske med et smil. Takk til Ian som alltid har tid til en kaffe, med en god latter som minner meg om hvor flott livet er. Det blir rart, etter 11 år, å ikke studere med deg lenger.

Mamma og pappa, Marina og Håkon Bleken, fortjener en spesiell takk nå som jeg endelig er ved slutten av studiene. Hjemme har jeg alltid blitt oppmuntret til å søke kunnskap og mette min nysgjerrighet. Jeg er heldig som kan søke inspirasjon hos dere, og jeg håper dette eplet ikke faller langt fra stammen!

Contents

Preface

This thesis consists of one experimental and one computational part. By experiments, the effects of acidity on the Methanol-to-Olefins (MTO) process were investigated, using two catalysts that only differ in acidity. The zeolite H-SSZ-13 and the silicoaluminophosphate H-SAPO-34 both have the same crystalline structure, but variations in the framework atoms provide different acid strength.

Density Functional Theory was made use of in performing computational studies on the acidity of the two materials, by modeling adsorption of methanol and CO on the catalytic sites.

In the first four chapters theoretical background for the work in this thesis is described. In chapter 1 catalysis and zeolites are introduced, while chapter 2 considers in more detail the Methanol-To-Hydrocarbons (MTH) reactions, where specific zeolites act as catalysts. The theoretical background of the various instruments employed in the experimental work is presented in chapter 3. Chapter 4 briefly addresses the theory related to the computational work.

The experimental setup is described in chapter 5. The results of the experimental work of this thesis are presented and discussed in chapter 6, including a section on sources of error. The results are also discussed in relevance to reports in the literature, and some suggestions for further work are listed. The conclusions of the experimental work are presented in chapter 7.

The results of the computational work are described and discussed in chapter 8, together with comparisons with results from literature.

Chapter 1

Catalysis and zeolites

1.1 Catalysis

In a general chemical reaction, reactants A and B react to form a product P, with a reaction barrier E_a (Fig. 1.1).

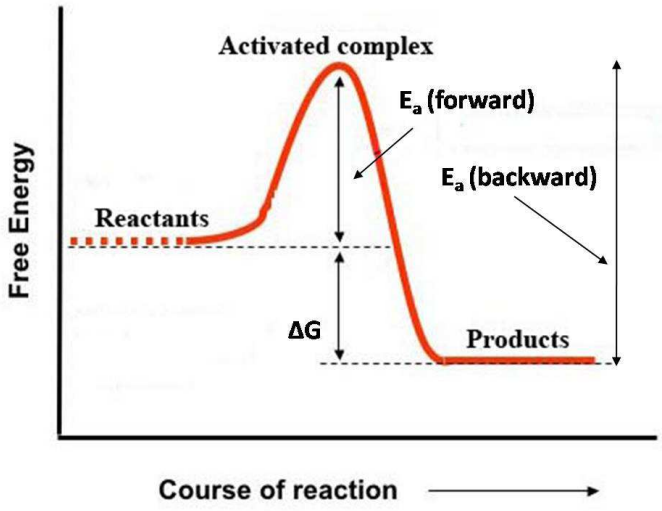

Figure 1.1: In almost all chemical reactions there is an energy barrier E_a. Activation energies for the forward and the backward reactions are different. ΔG denotes the free energy for the forward reaction, the negative of this value is the free energy for the reverse reaction

In many reactions E_a is very high and the use of a suitable catalyst may serve to lower this barrier

by enabling a different reaction path. In a chemical reaction, the role of a catalyst is to change the reaction path so that the activation energy is lowered and the reaction is accelerated. Figure1.2 shows an example of the steps in a catalyzed reaction compared to the uncatalyzed reaction.

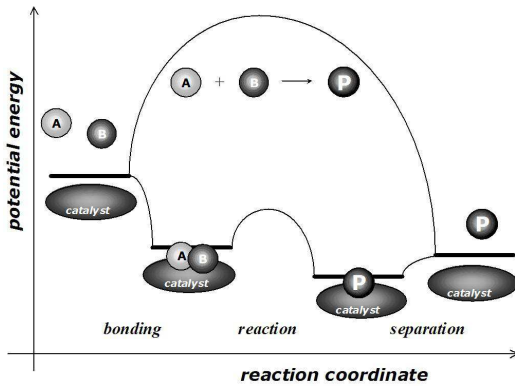

Figure 1.2: Schematic representation of a catalyzed versus a non-catalyzed reaction. The total energy of the system is lowered upon adsorption of the reactants to the catalyst surface. The reaction barrier for the reaction on the catalyst is lower than the reaction barrier in the gas phase. Energy is required for desorption of the product. Figure adapted from [1]

The catalyst is involved in the reaction, but remains unaltered in the end and does not take part in the overall stoichiometric equation. Figure 1.2 represents a heterogeneous catalytic system with a solid catalyst. The reactants, which are in a liquid or gaseous phase, adsorb on the catalyst in an exothermic reaction. Once the adsorbed reactants are close enough they react to form an adsorbed product. The desorption of the product is endothermic. The mechanism of catalytic reactions may have more intermediate steps, but the energy barrier for each step is lower than for the direct route from reactants to products.

It is important to notice that a catalyst only changes the kinetics of a reaction, not the overall thermodynamics. This means that the thermodynamically most stable product will be the same with and without catalyst. It may however be impossible to reach the thermodynamically most favorable state within a feasible time range without the catalyst. Also, the catalyst lowers the energy barrier equally much in both directions of the reaction and thus it increases the rate towards equilibrium. This means that designing a catalyst for an uphill reaction (thermodynamically unfavorable) is an impossible task.

Catalysis is divided into two categories; homogeneous and heterogeneous catalysis. A homogeneous catalyst is in the same phase as the reaction mixture, while a heterogeneous catalyst is in a different

phase than the reaction mixture. The work in this thesis concentrates on a specific field of heterogeneous catalysis, the conversion of methanol to higher hydrocarbons, using zeolites and zeotype materials as catalysts. Depending on the desired product distribution, different materials and reaction conditions are employed.

1.1.1 Heterogeneous catalysis

Heterogeneous catalysis is of fundamental importance for society as most of our base and intermediate chemicals, as well as petrol (gasoline) etc., are produced using solid catalysts. Without these catalysts many products would be impossible to make within a reasonable time scale and in most cases the reactions would be economically untenable due to high energetic costs. With the use of catalysts, reactions may be carried out at the most favorable thermodynamic conditions, and also at lower temperatures and pressures. Catalysts are designed to optimize the selectivity towards desired products while suppressing formation of side- and waste-products. A great advantage of heterogeneous catalysis with solid catalysts compared to solution catalysts is that it is trivial to separate solid catalyst from liquid and gaseous reaction mixtures. Often, solid catalysts are also more stable at working temperatures and also at the higher temperatures usually needed for regeneration [2].

Solid acids are the most important catalysts in terms of volume and number of commercial processes. The first solid acid catalysts were amorphous materials, but with the development of crystalline aluminosilicates as zeolite solid acids, the latter have become increasingly more important. Zeolite catalysts have well defined pore topologies and acid sites of reasonably uniform strength and for this reason their use has increased tremendously.

1.2 Zeolites

Zeolites and zeotype materials are a subclass of the molecular sieves, which are porous solids with pores of molecular dimensions 3-20 Å in diameter. Zeolites are well-defined crystalline materials with uniform pore-sizes throughout the structure[3]. Since the pores and cavities are regular and

well-defined, zeolites function as shape-selective catalysts that can distinguish shapes and sizes at the molecular level.

The primary building block in zeotype materials are TO_4 tetrahedra where the central T atom can be any element that is four-coordinated to oxygen. The tetrahedra are linked through the oxygen atom at the vertices as exemplified in Figure 1.3. The properties depend much on the T-atoms in the framework. One such property is the Brønsted acidity described in section 1.2.4. In zeolites the T-atoms are Si and Al.

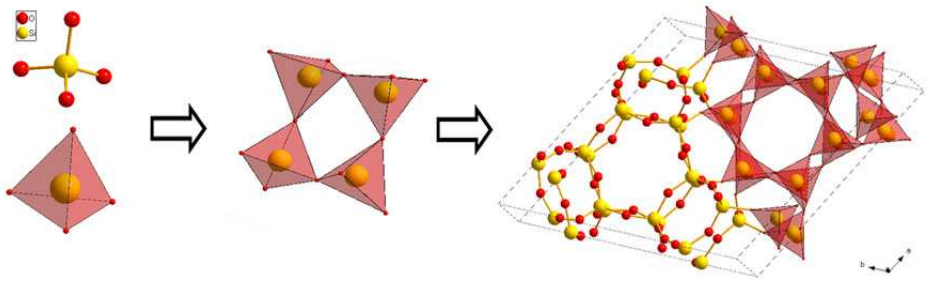

Figure 1.3: SiO_4 and AlO_4 tetrahedra build up the structure, from British Zeolite Organization www.bza.org

The AlO_4 and SiO_4-tetrahedra are assembled into bigger blocks which repeated give the whole structure. The pore-sizes, which are of particular importance for the molecular sieve property of the structure, are characterized by the rings formed by the tetrahedra. Typically these rings consist of 8 (e.g. zeolite A), 10 (e.g. zeolite ZSM-5), 12 (e.g. zeolite Y) and 14 (e.g. zeolite UTD-1) T-atoms. The size of these ”windows” determines which molecules can pass through the pores. 8-rings are considered small openings while 12-rings are considered rather big. Usually, nature tends to form structures with densely packed atoms. Open structures are formed by using organic templates in the synthesis gel. Although the structure of each zeolite is well-defined, the shape and size of the pores vary according to temperature and guest-species inside the pore.

1.2.1 Historical overview

The first zeolite mineral, stilbite, was discovered in 1756 by the Swedish mineralogist Cronstedt [3]. He called the new mineral zeolite from the Greek ”zeo”, to boil, and ”lithos”, stone, because upon heating it gave off water as if boiling. The discovery of other natural zeolites followed and by the mid-1930's the ion exchange, adsorption, molecular sieving and structural properties of zeolite minerals were studied and also several syntheses of zeolites were reported. However, the early synthetic work remains unsubstantiated because of difficulties in reproducibility and poor characterization of the materials. Barrer started working on zeolite adsorption and synthesis in the mid-1930's and in 1945 he presented the first classification of the then known zeolites based on molecular size considerations [4]. In 1948 he reported the first definite synthesis of mordenite [5] and also another zeolite which he states “does not appear to occur naturally” [6]. Following Barrer's work, industry became interested in the synthetic zeolites and Milton of the Linde Division of Union Carbide Corporation initiated studies in the synthesis of zeolites with the aim of separation and purification of air. This lead to the discovery of several synthetic zeolites, and the earliest applications were the drying of refrigerant gas and natural gas. In 1962 Mobil Oil introduced the use of synthetic zeolite X as cracking catalyst and a high research activity thus started in zeolites as catalysts in the realm of oil products.

Now the major applications areas of industrial synthetic zeolites are as adsorbents, catalysts and ion-exchange materials. This includes detergents where mostly zeolite A functions as an ion exchanger. Also natural zeolites have industrial applications, e.g. chabazite, erionite, mordenite and clinoptilolite have been commercialized for adsorbent applications.

1.2.2 Structure and properties

The term *zeolite* strictly refers to aluminosilicates, and *zeotype*s are closely related materials where other elements are synthetically incorporated into the same frameworks, thus altering the properties of the zeolites. Names used for zeolites and some zeotypes are given in Table 1.1.

Zeolites and zeotype materials all belong to different framework types (topologies) [3]. The topology

Table 1.1: T-atoms in zeolites and zeotypes.

Zeolite	T-atoms	Zeotype	T-atoms
Aluminosilicate	Si, Al	Aluminophosphate (ALPO)	Al, P
		Silicoaluminophosphate (SAPO)	Si, Al, O

describes the connectivity of the T-atoms without reference to the chemical composition. It determines the size and shape of the pore openings, the dimensionality of the channel system and the volume and arrangement of the cages. Considering the vast amount of different possible chemical compositions, it is clear that the number of different zeotype materials is immense and it is therefore of particular interest to study how their properties vary systematically. The central T-atom can be any tetrahedrally coordinated atom. However, it is important to keep the charge balance and therefore the exchange of T-atoms often introduce cation sites in the zeolites. The framework structure is relatively open and characterized by specific channels and cavities. Although the frameworks are different, they are often built up from similar smaller structures, and the most common of these are given specific names, for instance *n*-rings defined by the *n* number of T-atoms in the ring. The rings give the upper limit for the size of the molecules that may pass into the channels and cavities and diffuse through the structures. An 8-ring is considered a small opening, a 10-ring medium and a 12-ring big. Figure 1.4 shows some recurring units in the framework types.

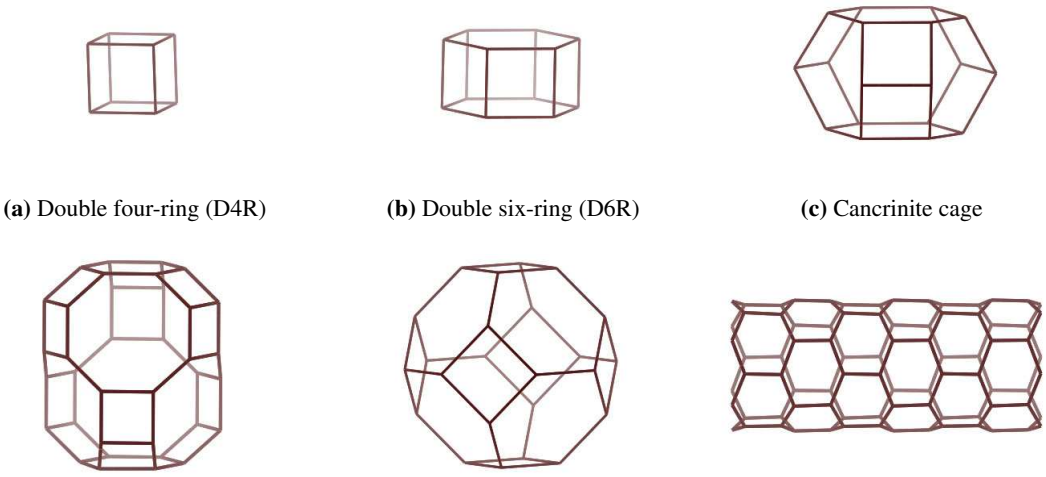

(a) Double four-ring (D4R) **(b)** Double six-ring (D6R) **(c)** Cancrinite cage

(d) Chabazite cage **(e)** Sodalite cage **(f)** AFI channel

Figure 1.4: Different subunits occurring as building blocks in zeolites

SAPO-34 (Chabazite topology) has 8-ring openings and is considered a small pore material, while for instance ZSM-5 (MFI) has 10-ring channels and zeolite β (BEA) 12-rings. Which molecules can diffuse through the structures is determined by the size and shape of the pores and channels. Figure 1.5 shows the structures of zeolite ZSM-5 (MFI) and zeolite β (BEA), which are shown looking down one of two intersecting channels. The 12-ring channels of zeolite β are somewhat bigger than the 10-ring channels of ZSM-5, so that hexamethylbenzene (HMB) easily diffuse through β, while the only tetramethylbenzene (TetraMB) that can diffuse through the ZSM-5 channels is durene (C_{2v}) [2].

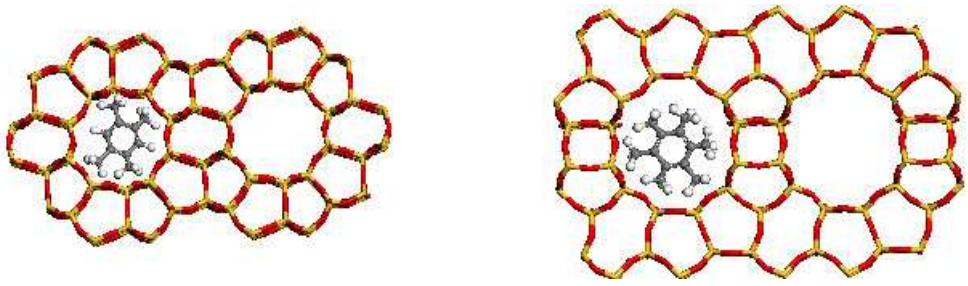

(a) (b)

Figure 1.5: The structures of (a) ZSM-5 and (b) zeolite β. Both frameworks have channels, but with different sizes, as shown by the methylated benzenes that can pass through the channels. In ZSM-5 1,2,4,5-tetramethylbenzene is the biggest polymethylated benzene that can diffuse through the structure, while hexamethylbenzene easily passes through zeolite β.

Zeolites and zeotype materials are not characterized by a systematic nomenclature, as the discoverers of a new framework assign a three-letter code to the structure. But all materials with the same framework will carry the same three letter code, so that they more easily can be identified and compared. For example is the zeolite ZSM-5 of the MFI structure while the zeolite SSZ-13 (Chabazite) and the zeotype SAPO-34 have the CHA connectivity. Information on the different structures can be found in the *Atlas of Zeolite Framework Types* [7].

1.2.3 Chabazite and SAPO-34

Chabazite is a naturally occurring zeolite with a cage-structure (Fig. 1.6a). The cages of about 1 nm are interconnected through windows of diameter 0.38 nm. H-SAPO-34 is a silico-aluminophosphate in the chabazite topology (CHA). Figure 1.6b shows how the T-atoms change from Si to alternating Al and P in the silicoaluminophosphate. One acid site is introduced in each figure.

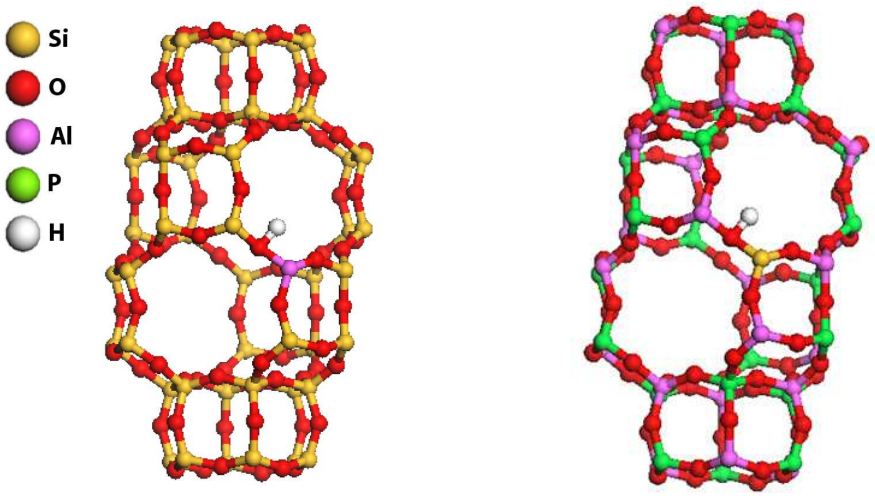

(a) (b)

Figure 1.6: The cage in (a) H-SSZ-13 and (b) H-SAPO-34.

Although there are relatively large pores in the material, the windows between the cages are smaller and hence big molecules cannot diffuse in and out of the crystals. This also means that big molecules that may be formed within the cages during reaction will be trapped inside. H-SSZ-13 is a zeolite with a Si/Al ratio of 11, equivalent to one Al per cage. Since H-SAPO-34 and H-SSZ-13 have the same topology, their only difference lie in the framework composition. This leads to differences in acidity which will be further addressed when acidity has been introduced in the next section.

1.2.4 Acid strength

Among the properties that vary with chemical composition is the acid strength. Solid acidity is a very ambiguous term, difficult to define and measure [2]. There is a distinction between Brønsted acid (proton donor) and Lewis acid (electron pair acceptors) sites. Several solid acid catalysts have a large number of Lewis acid sites (e.g. sulfated zirconia), but an ideal zeolite without defects in the crystal lattice has only Brønsted sites. Lewis sites can be introduced in a zeolite by ion-exchange or steaming to create defect sites associated with extra-framework aluminum. Acidity can both refer to acid strength or to acid site density (number of acid protons). As shown in Figure 1.7, substitution of silicon with aluminum in an aluminosilicate creates an acid site (proton on the oxygen-bridge between

the T-atoms).

The composition of the zeolite framework is frequently reported as the silicon to aluminum ratio (Si/Al) or the silica to alumina ratio (SiO_2/Al_2O_3) and the acid site density is inversely proportional to these quantities. In silico-aluminophosphates (SAPO's) the acid site density is often lower because of clustering of the silicon T-atoms.

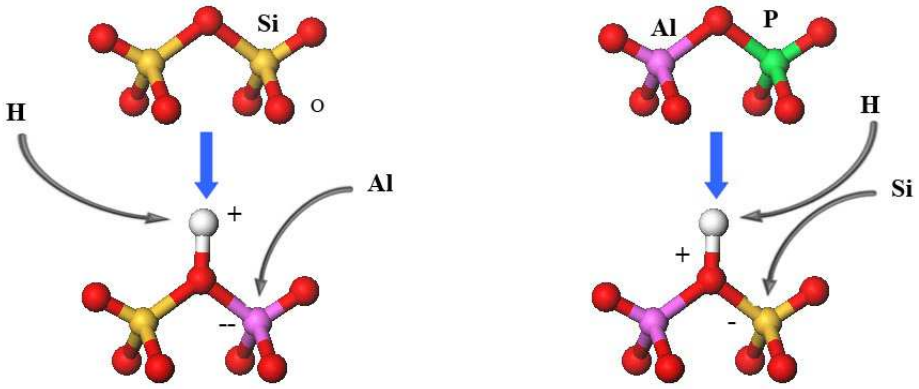

(a) silicate **(b)** aluminophosphate

Figure 1.7: Substituting one Si with Al in pure silicate creates a Brønsted acid site, while the same effect is obtained in an aluminophosphate by substituting P with Si. NB: The environment of the acid site is not equal in the two materials, as seen in figure 1.6.

The substitution of one Si with one Al in the chabazite structure introduces four topologically distinct acid sites (Fig. 1.8 O1, O2 and O3 are oxygens in 8-rings, and therefore the attached hydrogen (or other cation) is exposed to two cages. This is because each 8-ring the the chabazite structure connects two cages. The O4 position is in a six-ring, and therefore the attached cation is only exposed to one cage. It is important to note that in the pure silicate, all Si-atoms are topologically equivalent. This means that the insertion of one defect in the unit cell only gives rise to four different cation-sites. The same is true in the alumino-phosphate, were all P-atoms are topologically equivalent and all Al-atoms likewise.

Brønsted acid sites are essential for the catalytic activity of zeolites, and the acid site density and strength are decisive for the properties of each material. For instance secondary reactions may be more important on a catalyst with high acid density or strength. H-ZSM-5 with little or no Lewis

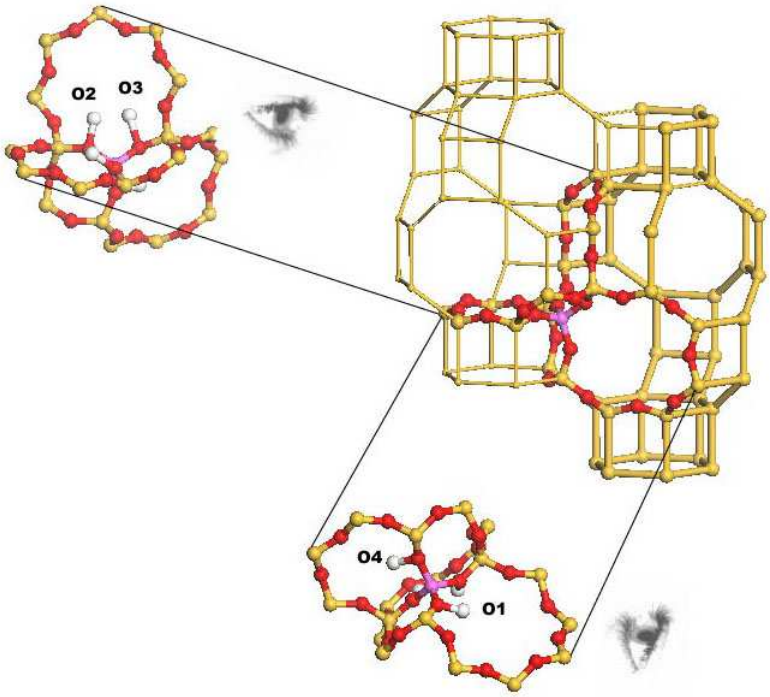

Figure 1.8: The chabazite structure, two cages and and the four acid site positions introduced with the exchange of one Si with Al.

acidity is one of the strongest solid acid catalysts, which indicates that Brønsted acidity is the most important type of acidity in these structures.

It is also important to note how framework atoms may change the acidity of a material. Since the framework of H-SAPO-34 and H-SSZ-13 is the same, only the composition of the T-atoms influences the acidity. The effects of Brønsted acidity can thus be studied, and this thesis is specifically concerned with this.

As previously stated, H-SSZ-13 (pure silicon-aluminum framework) has a Si/Al ratio of 11, which gives one acid site per cage. H-SAPO-34, which has the same structure, will have the same acid site density with an (Al+P)/Si ratio of 11. H-SAPO-34 with this acidity is less acidic than H-SSZ-13, as shown by Bordiga et al. They found that while there is a strong protonation of H_2O in H-SSZ-13, the H_2O protonation is a minor feature of H-SAPO-34. Because of this, methanol interacts strongly with the Brønsted sites in H-SSZ-13, and at high coverage protonated species are formed. In contrast, in the less acidic H-SAPO-34 only strong H-bonding was observed. H-SSZ-13 also has a strong acidity compared to H-ZSM-5 and H-β, which are zeolites with more open frameworks [8, 9].

1.2.5 Catalysis in zeolites

Zeolites are used in a wide variety of applications, and amongst these is the use as catalysts in the petrochemical industry. Zeolite Y is the most widely used cracking catalyst in oil refineries, while other zeolites are used for the conversion of methanol to higher hydrocarbons. Pore size and shape as well as accessibility to the pores are decisive for the selectivities of the reactions. Pore and shape selectivities are commonly subdivided into three types, reactant selectivity, product selectivity and transition state shape selectivity (Fig. 1.9) [3]. Reactant selectivity takes place when the zeolite cata-

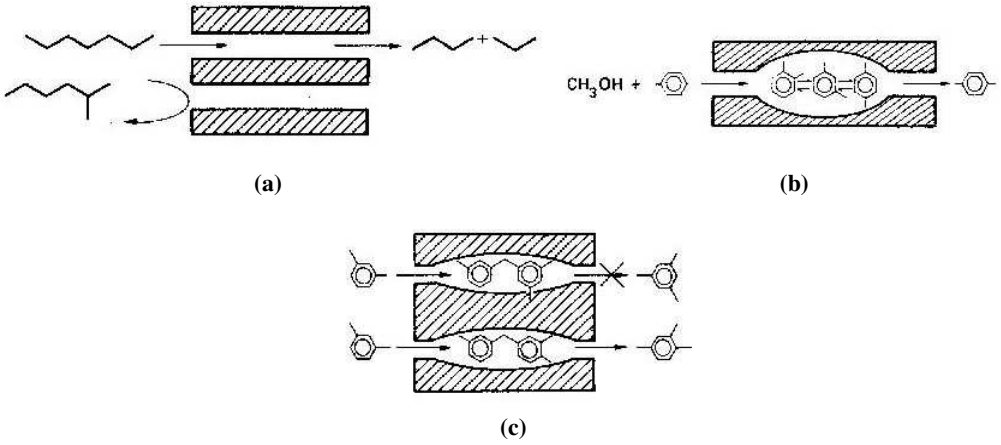

Figure 1.9: Shape selectivities in zeolites, using the CHA structure as an example (a) reactant selectivity, (b) product selectivity and (c) transition state shape selectivity.

lyst acts as a molecular sieve and only small enough molecules are allowed to enter the structure. This type of selectivity is not of interest in the conversion of pure methanol because it is small enough to freely diffuse into both the MFI and CHA structures. 1,2,4,5-tetramethylbenzene is the largest methylated benzene that can theoretically diffuse into the MFI structure, the other tetramethylbenzenes are to big too enter. When the selectivity is controlled by the formation and diffusion of the molecules, the term product selectivities is used. Not only does the size of the pores and openings decide which products can diffuse out of the crystal. Also the size of the crystal may have an influence on the diffusivity of the different products. The last selectivity type is transition state shape selectivity. The pore size and shape of the zeolite may not allow all possible transition states and reaction intermediates to be formed.

Chapter 2

Methanol-to-Hydrocarbons (MTH)

2.1 History and industrial applications

In the early 1970s researchers C. Chang and T. Silvestri at Mobil Central Research discovered that methanol was converted to higher hydrocarbons over the zeolite H-ZSM-5 [10, 11]. These hydrocarbons were a mixture of aromatic compounds, olefins and paraffins, giving a fine grade of gasoline. The first commercially available process became the methanol-to-gasoline (MTG) process which Mobil ran in New Zealand during the 80's. The production of gasoline was later stopped since the crude oil prices dropped, causing gasoline production to become economically unfavorable, and only the methanol synthesis continued. Other processes in the demonstration stage are the UOP/Norsk Hydro Methanol-To-Olefins process (MTO), Mobil's Olefin-To-Gasoline/Distillate (MOGD) process and Haldor Topsøe's Integrated Gasoline Synthesis (TIGAS) process. The TIGAS process was demonstrated on a pilot scale in the mid-1980s, but it was not implemented on an industrial scale since energy prices did not permit this. The UOP/Norsk Hydro process is a process that produces polymer-grade ethene and propene from methanol, and also this process has been demonstrated on a pilot plant. A similar process, the Lurgi/Statoil Methanol-To-Propylene (MTP), has also been developed. These processes are collectively called Methanol-To-Hydrocarbon processes (MTH). None of these are run at full-scale today, but commercial interest in MTG is now again increasing due to the changes in the

crude oil market. As crude oil resources are being depleted attention is moved more towards natural gas and coal as hydrocarbon sources. Improved methanol production plants also make the processes economically better alternatives than previously.

Even though these processes are not yet fully operative on an industrial scale considerable research has been put into understanding the reaction, both in academia and in industry. The Methanol-to-Hydrocarbons reaction (MTH) has been intensively studied, including the closely related Methanol-to-Olefins process (MTO) which can be regarded as MTH reaction stopped at the primary products. The MTO process has become of increasing interest as it may be commercialized to meet the increasing demand of polyolefins [10].

2.2 Catalysts

The catalysts used in the MTH-processes are zeolites, in particular H-ZSM-5 and H-SAPO-34 (Table 2.1).

Table 2.1: Some of the most important industrial MTH-processes and their catalysts

Process	Catalyst
Mobil's MTG	H-ZSM-5
TIGAS	H-ZSM-5
Lurgi's MTP	H-ZSM-5
UOP/Hydro MTO	H-SAPO-34

The catalyst for the MTG and MTP reactions is H-ZSM-5 which has the MFI topology. This shows that changing parameters other than the catalyst itself strongly influences the product distribution. The catalyst in the UOP/Hydro MTO process is called H-SAPO-34, and is of a very different character, both in topology and chemical composition. H-ZSM-5 is a zeolite, while H-SAPO-34 is a silicoaluminophosphate. The H-ZSM-5 MFI framework is a channel structure, with straight channels in one direction and sinusoidal channels in another, the H-SAPO-34 CHA framework is a cage structure.

2.3 Reaction mechanism

The reactant methanol is produced from synthesis gas (syn-gas), which is a mixture of H_2, CO and CO_2, and is produced by steaming methane (natural gas) or coal [2]. The syn-gas is then converted to methanol over a $Cu/ZnO/Al_2O_3$ catalyst.

The general stoichiometric equation in the MTH processes can be written as

$$CH_3OH \longrightarrow "CH_2" + H_2O \tag{2.1}$$

The mechanism of the MTH reaction has proved to be very complicated. Figure 2.1 shows a much simplified, without much mechanistic insight, scheme of the steps in the reaction. It is convenient

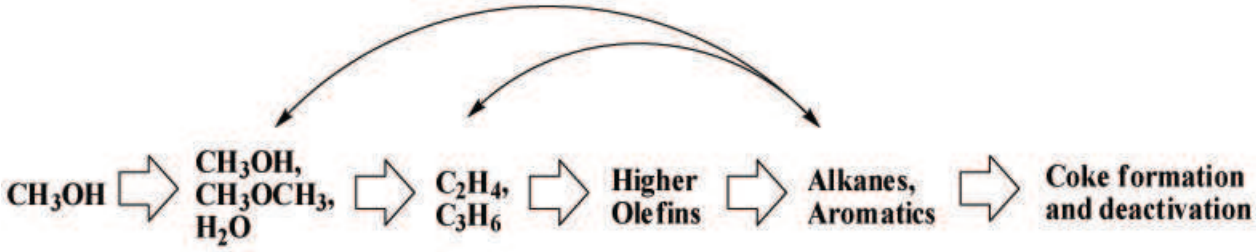

Figure 2.1: Schematic presentation of the MTH-reaction. Adapted from [12]

to, at least initially, describe the MTH process in five steps[12, 10]. The first step is the equilibration of methanol (MeOH) with dimethyl ether (DME). The second step is the kinetic induction period in which there is little conversion and the formation of light olefinic products. Secondary olefinic reaction may then occur, forming higher olefins and then also alkanes and aromatics. Eventually coke will be formed leading to deactivation of the catalyst. The scheme proposed is however much simplified; the MTH reactions do not proceed by such a consecutive mechanism. The curved arrows indicate that both methanol/DME and olefins may react with the aromatics, as well as being formed through aromatic compounds. As previously mentioned the methanol-to-olefins process may be regarded as MTH stopped at the olefins, but aromatic compounds and coke are produced in the catalyst as will be presented both in this introduction and in the results of this thesis. Therefore the steps in Figure 2.1 should not be taken as indication of the MTH mechanism, but rather be used as a reminder of the

different types of organic material present during the reaction.

2.3.1 Direct mechanism

Early research on the MTH-mechanism was focused on the formation of the first carbon-carbon bond. According to Støcker more than 20 mechanisms have been proposed for the reaction [13, 14]. Some of these reactions are shown in abbreviated form in Figure 2.2.

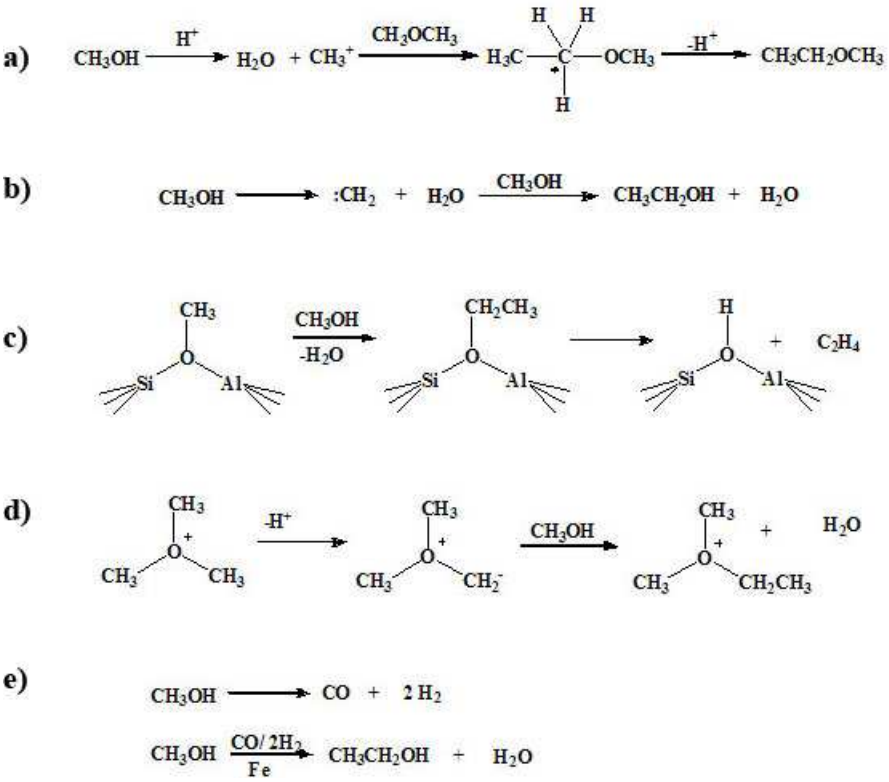

Figure 2.2: Some of the classical "direct" mechanisms for the conversion of methanol/DME to olefins (or a direct precursor): (a) A pathway showing a carbenium ion alkylating DME to form a carbonium ion. (b) A carbene pathway. (c) An alkoxy chain growth process occurring on a framework site. (d) An abbreviated oxonium-ylide route. (e) A proposed mechanism featuring CO, showing a role for the transition- metal impurities. [10].

The first proposal was that methanol might be activated on the catalyst to form carbenium ion, CH_3^+, or carbene $:CH_2$. Several free radical routes were also suggested as possible mechanisms for the direct conversion of methanol to a species with a "first" carbon-carbon bond. It has been shown that methanol can react with zeolite acid sites to form framework bound methoxy species, but chain growth has never been observed [10]. Later, indirect mechanisms for the formation of C-C bonds

were considered in more detail (Fig 2.3), and it is now widely accepted that such mechanisms prevail in the MTH-processes.

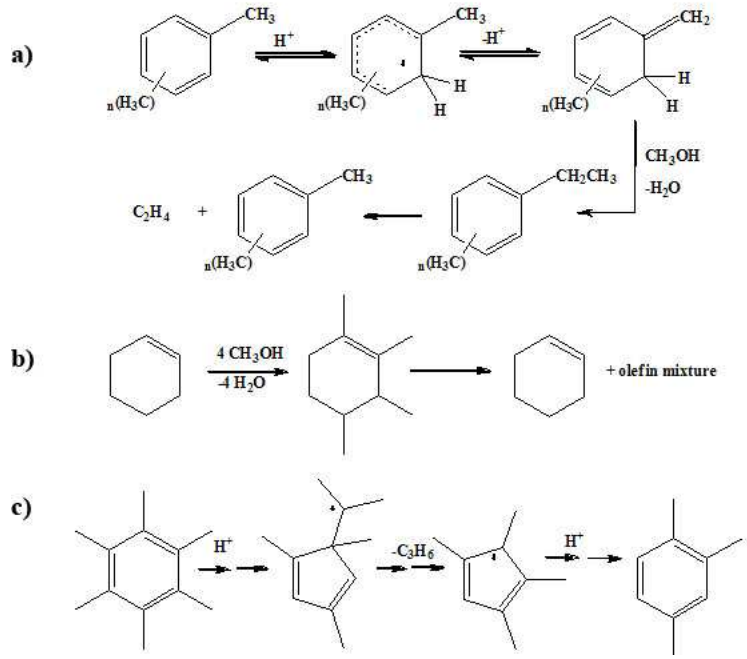

Figure 2.3: Early proposals that have significantly shaped current thinking about the hydrocarbon pool mechanism (a) Mole's 1983 mechanism of methylbenzene side-chain alkylation (b) Langer's proposal (c) The paring reaction in highly abbreviated form [10].

2.3.2 Hydrocarbon pool

The hydrocarbon pool mechanism (Fig 2.4) is entirely different from the suggested mechanisms for direct C-C bond formation [15, 16, 17, 18, 19]. This mechanism was first proposed by Dahl and Kolboe in the mid 1990's as a phenomenological scheme, without much details in the constituents of the pool. The key idea is that hydrocarbon species on the catalyst are essential for methanol conversion to olefins, and thus act as co-catalysts in the reaction.

Dahl and Kolboe showed by isotopic labeling that ethene and propene are very little reactive compared to the methanol in H-SAPO-34 [15, 16]. Ethene thus showed to be a quite inert primary product, so that a consecutive-type mechanism, with ethene as primary product, to give higher hydrocarbons by being methylated by MeOH/DME is untenable. Svelle et al. however found that at elevated propene or n-butene partial pressures, alkene + alkene reactions are not insignificant for the H-ZSM-5 system

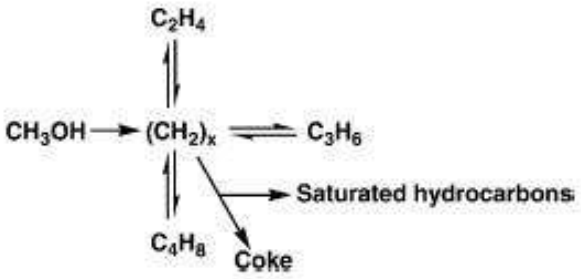

Figure 2.4: Schematic presentation of the hydrocarbon pool from [15]. Methanol is added to the pool where light olefins are formed. The olefins may react further to form other (bi)products such as saturated hydrocarbons and coke.

[20]. The degree of the alkene inter-conversion reaction increased with decrease in temperature. But in the presence of methanol the alkene inter-conversions were strongly suppressed in agreement with Dahl and Kolboe's results.

The MTH/MTO reaction was first considered to be an auto-catalytic reaction, however it has later been shown that there is an induction period and thereafter no evidence of auto-catalysis [17, 21]. Later Mole and co-workers showed that aromatic hydrocarbons function as co-catalysts for methanol conversion [22, 23], and these findings are consistent with the proposed hydrocarbon-pool mechanism. Arenes are the dominant molecules confined, formed in parallel with the MTH reaction. These are not only spectator byproducts, but do take part in the reaction as penta- and hexamethylbenzenes (PMB and HMB) are strongly reduced when flushing with carrier gas [24, 25]. This study was made in SAPO-34 which has small pores such that the smaller arenes also are confined in the cavities.

The hydrocarbon pool mechanism is based on the presence of hydrocarbons on the catalyst, that continuously add on methanol and split off small olefins. It has become clear that the main constituents of the hydrocarbon pool are polymethylated benzenes, polymethylated naphtalenes and polymethylated cyclopentenyl ions. However different ring-structures and aromatics are particularly active in different zeolites, which indicates the importance of the zeolite pore and channels as shape-selective for the intermediates (Table 2.2).

In zeolite β, HeptaMB$^+$ is an active part of the hydrocarbon pool, as shown by Bjørgen et al. [26]. HeptaMB$^+$ is the terminal benzene methylation product, and there are two proposed mechanisms for its role in the hydrocarbon pool [26]. The first is the "paring reaction", in which heptaMB$^+$ is

Table 2.2: Active species in the hydrocarbon pool of different catalysts

Zeolite/Zeotype	Hydrocarbon pool species
H-β	Heptamethylbenzenium ion
H-ZSM-5	cyclopentenyl ion + lower methylated benzenes
H-SAPO-34	hexamethylbenzene + dicyclopentadiene

believed to split off olefins after appropriate rearrangements under formation of lower methylbenzenes that again are re-methylated by methanol. The second mechanism is based on the formation of an exocyclic double bond after deprotonation of heptaMB$^+$. Subsequent methylations of this exocyclic double bond by methanol result in formation of an alkyl group that may be eliminated as an alkene. The initial reactant was pure heptaMB$^+$ fed as its corresponding base 1,2,3,3,4,5-hexamethyl-6-methylene-1,4-cyclohexadiene. It was found that the product spectrum had a close resemblance to that formed when methanol or HMB were the reactants, and thus heptaMB$^+$ is a plausible reaction intermediate in this system. HeptaMB$^+$ has only been detected by co-feeding experiments and not with only methanol as feed, and it is therefore not certain that the actual MTH reaction in zeolite β involves this compound. However it might still be so, and the reason for it not being observed is could be short lifetime and small concentrations at all times. Arstad et al. carried out quantum chemical calculations to investigate intra-molecular isomerization reactions and eliminations of small alkenes from heptaMB$^+$ isomers, starting from two different reaction pathways: ring contraction and ring elimination [27, 28, 29]. They showed that the methylation of methylbenzenes on a zeolitic acid site becomes easier as the number of methyl substituents on the benzene ring increases. In the absence of steric constraints, formation of heptamethylbenzenium ion is likely and this result suggested that the ion plays an important role in the MTH reaction. By theoretical models they also calculated that carbon atom scrambling and alkene formation in the MTH reaction take place via the same intermediates.

In H-SAPO-34 hexa- and pentamethylbenzenes are main constituents in the hydrocarbon pool. Studies of the molecules confined to the different cavities after short time on stream (TOS) have been done by Arstad et al. [25]. These studies where done mainly at 325 °C, which is about 100 °C below optimal temperature for converting methanol to hydrocarbons, because at this temperature the reactions are so slow that the changes in the molecules confined in the cavities can be monitored. The reaction

was stopped and the catalyst quenched between 30 to 120 seconds on stream. They showed that the methylated aromatics confined in the cavities are not merely stable spectator byproducts, but do actually take part in the reaction. This was shown by flushing with carrier gas after the methanol feed was stopped and monitoring the content of the cavities [24]. HMB and PMB disappeared, thus indicating that they do play an active role in the reaction, while xylenes and trimethylbenzenes (TriMB) increased correspondingly. The latter are smaller and their increase indicates that they are unreactive and that none of the molecules diffuse through the catalyst. That HMB and PMB disappear must therefore have decomposition as cause.

Another ring structure that has been investigated is the cyclopentenyl cation and its role in the synthesis of hydrocarbons from methanol on zeolite catalyst H-ZSM-5 [19]. Haw et al. state that these cyclopentenyl cations form during the induction period from small amounts of olefins, and that on zeolite H-ZSM-5 the principal role of the induction reaction is to synthesize the cyclopentenyl cations that characterize the working catalyst. The cations are stable species on zeolite acid sites, and the cyclic dienes obtained by their deprotonation are only slightly less stable. The cations form cyclic dienes which are more easily methylated than propene and ethene, and by side chain methylation and skeletal isomerization they may form cations with alkyl substituents, that may eliminate C2 and C3 olefins.

2.3.3 Competing mechanisms

Not only ring structures can be reactive in zeolites. In addition to methylating carbon ring structures and aromats in pores, methanol may also methylate alkenes present in the catalyst. Thus higher alkenes are produced which again may be further cracked to smaller alkanes. This cyclic process might be a competing reaction path, and knowledge of the rate of alkene methylation is therefore an important issue [30]. Svelle et al. recently published a detailed study on the hydrocarbon pool in H-ZSM-5. Their results suggest two partially separated reaction cycles, one for the formation of olefins, and one for the formation of higher alkanes and alkenes [31, 32]. For the MTO process, the primary reaction that gives small olefins (ethene and propene) should be where the reaction stops. However, if the solid acid is sufficiently strong also secondary olefin reactions are important [12],

e.g. propene may trimerize or be methylated and then crack into butenes and pentenes. The SAPO's are of moderate acid strength, and thus tend to reduce secondary reactions. Also, SAPO-34, with its cages connected by relatively small windows, is very selective towards the formation of ethene and propene and is considered the most promising catalyst for the MTO process. The narrow 8-ring pores prevent any branched molecules to diffuse out of the catalyst particles into the surrounding phase [30].

Figure 2.5 gives an outline of a proposed hydrocarbon pool mechanism by Haw [12]. Propene trimerizes to trimethylcyclohexanes, which are promptly dehydrogenated by additional propene to yield trimethylbenzenes and propane. The methylbenzene is methylated to the far more active hexamethylbenzene. The latter is further methylated to ethylbenzene or isopropylbenzene derivatives. These then lose ethene or propene to give pentamethylbenzene which then regenerates HMB by methylation from methanol, thus completing the catalytic cycle.

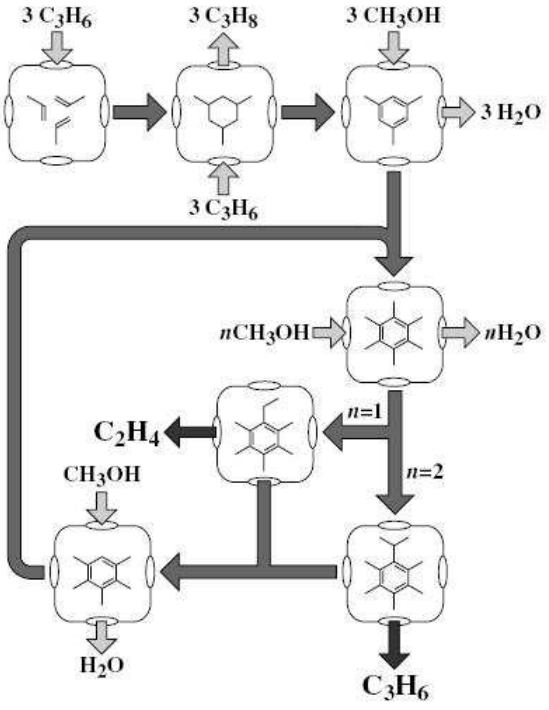

Figure 2.5: Outline of the hydrocarbon pool mechanism for MTO catalysis using schematic nomenclature for a supramolecular site [12]

Svelle et al. have performed a theoretical study on the methylations of alkenes with methanol over zeolites with varying acidic strength, concluding that the barrier of reaction is lowered with increased acidity [33]. They also studied the reactivity of methanol and DME, giving that DME is slightly

more reactive than methanol [34]. There is also a theoretical study of the dimerization of linear alkenes catalyzed by acidic zeolites which indicates that this direct mechanism cannot be completely neglected while considering only the hydrocarbon pool [35].

Adamantane chemistry

According to Engler et al. Lewis acid catalyzed isomerizations are highly successful methods for the preparation of adamantane, diadamantane and diamonoid molecules [36]. However there are many possible reaction pathways, and no mechanism has been fully elucidated.

Anderson et al. studied the formation of adamantanes from the reaction of 1-hexene over H-SAPO-34 [37]. They found that at low temperatures (240°C), the weight percent of adamantanes in the retained residue increased from 8 wt% after one hour of 1-hexene feed to 42 wt% after 28 hours, indicating that the adamantanes are non-primary products. Anderson et. al also found (alkyl)cyclopentadienyls to be a substantial products class in the retained material. Tetrahydrocyclopentadiene(endo) is a standard precursor for the formation of adamantanes by acid-catalyzed isomerization. Anderson therefore proposed the generalized pathway:

$$\text{1-hexene} \rightarrow \text{cyclopentadienes (CPDs)} \rightarrow \text{CPDs-dimer} \rightarrow \text{tetrahydroCPDs dimer} \rightarrow \text{adamantanes} \tag{2.2}$$

Anderson et al. did not observe the formation of adamantanes over H-ZSM-5, but they did detect CPDs. Adamantanes were neither found in ultra-stable zeolite Y. Since H-SAPO-34 is slightly less acidic than H-ZSM-5 is it plausible to think that shape-selectivity is the cause. The shape of the adamantanes fits strikingly into the cages of H-SAPO-34, like a hand in a glove. This is also the reason why adamantane derivatives are used as templates in the synthesis of H-SSZ-13, the zeolite analogue to H-SAPO-34.

These different molecules are undoubtedly present and active in the hydrocarbon pool of the zeolite where they have been studied. Thus, there is an indication that the hydrocarbon pool is different, depending on the shape and size of the pores in the crystal. This complies with the idea of shape-

selectivity for intermediates and transition states in the reaction. However, it must not be forgotten that a non-detected organic molecule is not equivalent to non-existing organic molecule.

2.3.4 Inorganic-Organic Hybrid Catalyst

For the very important MTO catalytic process, the working zeolite catalysts can be viewed as hybrid materials with both organic and inorganic components. The inorganic framework regulates mass transport and provides Brønsted acidity, and it also holds the active organic component in place near the acid site. The organic component, an unsaturated cyclic organic species with methyl groups, provides a site where C-C bonds can be formed and broken without having to pass by high energy species like CH_3^+, carbene or oxonium ylides. Since the active site seems to be an adsorbate aromatic molecule, the hydrocarbon pool mechanism proposes that the real catalyst in the MTH reactions is an organic-inorganic hybrid material.

This thesis concentrates on differences and similarities between H-SSZ-13 and H-SAPO-34 as catalysts for the MTO reaction. Previously, is has been reported that initial selectivity seems to be similar for both catalysts, and also to be independent of acid site density [38, 39]. However, deactivation rates are critically dependent on the acid site density, with Chabazite deactivating much faster than H-SAPO-34. Yuen et al. showed that borosilicates are not acidic enough to catalyze the reaction, although ppm levels of aluminum in the sieve dramatically affect the catalysis, driving forward a sequence of dehydration and carbon-carbon bond formation reactions. This suggests that there is an optimum acid density which has not yet been established [38].

The hydrocarbon pool mechanism for conversion of methanol is now widely accepted, but the question of how the first carbon-carbon bond is synthesized cannot be explained by this mechanism, neither the formation of the pool. There could be a possibility that another much slower route, which is negligible compared to the hydrocarbon pool once in action, provides this first step. Song et al. used highly purified methanol/DME to show that it was unreactive on the pure catalyst, hence there has to be some impurities inserted for the reaction to occur [40]. They state that even reagent methanol samples contain more than enough organic impurities to create a hydrocarbon pool on microporous

solid acids, and thus that if there is a direct route it is negligible.

2.4 Activation of catalyst

As the presence of aromatic compound in the feed have been shown to enhance the reaction, it is of interest to see how treating the catalyst with an aromatic compound before the methanol feed begins changes the catalytic activity. Mole et al. did a series of investigations using pulses of methanol with varying aromatic compounds as feed [22]. They showed that on their H-ZSM-5 catalyst the ethylene yield increased with pulse number, and also that when pulses were stopped for 40 minutes and then resumed, the conversion again increased with pulse number, but much more rapidly. This suggests that an activation of the catalyst, pretreating it with some aromatic compound, may increase its activity.

2.5 Deactivation of catalyst

Following Haw et al's division of the MTO process into five parts, the fifth stage is the catalyst deactivation. In H-SAPO-34 this process is partly understood. With time on stream, methylbenzenes are converted to pyrene through methylnapthalenes and phenanthrene derivatives [10]. Pyrene is the largest aromatic ring system that can be accommodated in the nanocages of the catalyst, and hence growth stops here. Since the windows are so small, these big molecules cannot diffuse out, and furthermore their presence in the cages hinders mass transport of reactants and products through the catalyst. The fraction of cages that are filled up will eventually become so big that the catalytic activity dies out as presented in Figure 2.6. In industrial use, spent catalyst can be regenerated by

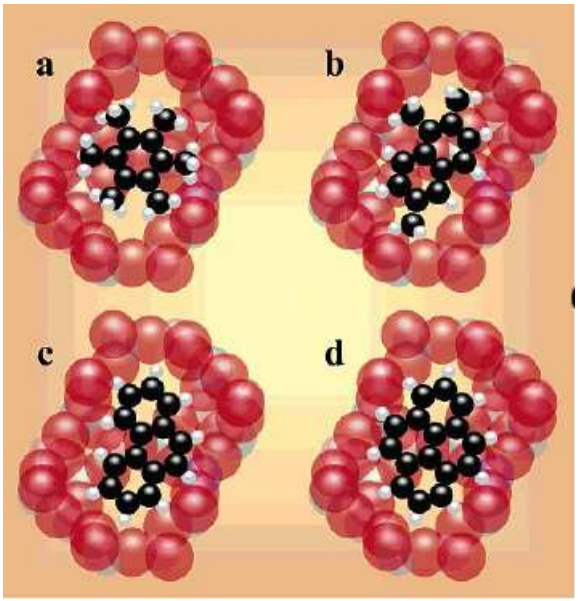

Figure 2.6: Molecular view of MTO catalyst deactivation shown for the specific case of H-SAPO-34 (a) Hexamethylbenzene and other methylbenzenes are present in a few percent of cages in active MTO catalyst. (b) With increasing time on stream, some of the methylbenzenes age into methylnaphtalenes. (c) Further aging into phenanthrene causes a loss of MTO activity and (d) the largest ringsystem to form in H-SAPO-34 is pyrene [10].

heating with air to burn trapped organic compounds.

Bjørgen et al. studied the precursors of coke formation and the deactivation in zeolite β [41]. The paring reaction is named so because of the apparent paring (peeling) of methyl groups from hexamethylbenzene (HMB), and they showed that this is a quite complex reaction. Besides having a reaction where HMB is transformed into small aliphatics and less methylated benzenes (especially

pentamethylbenzene (PMB)) there is a quite rapid formation of dihydro-triMN (MN = methylnaphtalene), which by methylation then splits off hydrogen to give hexaMN. The more important route may however be a self-condensation to produce much larger aromatic compounds, coke. In any methylating environment inside an acidic zeotype material there is a tendency for forming HMB, and if the pore-system is wide enough polyaromatic coke can be formed via naphtalenes. Figure 2.7 summarizes a possible mechanism for formation of coke precursors in a catalytic system like zeolite H-β. Co-reaction of [^{12}C]benzene and [^{13}C]methanol over H-β shows that if the pores in the zeolites are wide enough heptaMB$^+$ is easily formed from hexaMB, and here the hepta-species is of significant importance to the reaction speed [42].

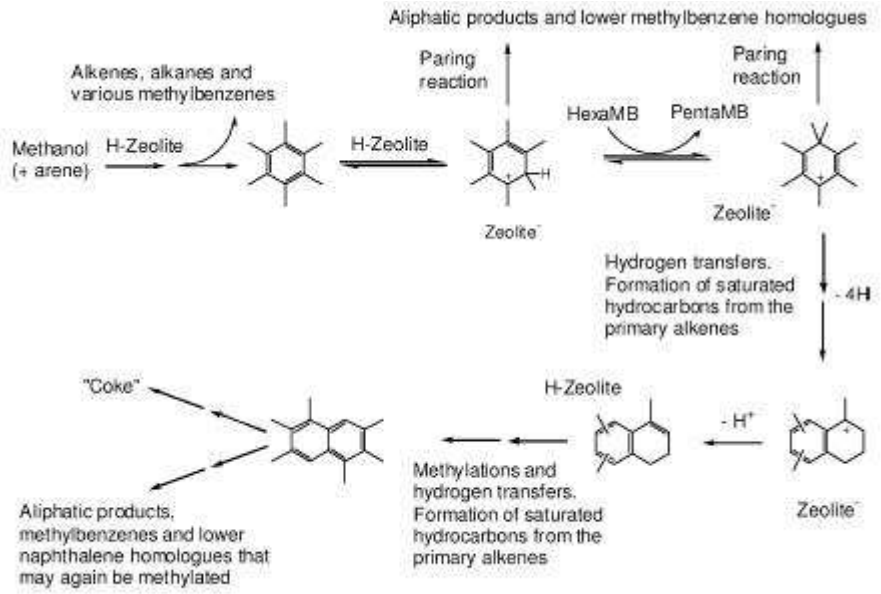

Figure 2.7: Summary of the reaction mechanism for formation of coke precursors from [41]

The exact reaction mechanism must be different for different zeolite frameworks as the structures determine what molecules can be formed in and occupy the pores.

Chapter 3

Background for experimental techniques

3.1 Gas Chromatography - GC

Chromatography is a method for separation of different compounds so that they can be analyzed one by one [43]. The basis for the technique is that the compounds will be distributed differently in two different phases in contact, the stationary and mobile phase. In gas chromatography (GC) the mobile phase is a gas, most often He or N_2. The gas carries the analytes through a column, and the stationary phase is on the inside of this column. The different analytes will interact differently with the stationary phase; those that interact more strongly will be more retained and be eluted later than the other compounds. When the interaction is due to van der Waal forces between the analytes and the stationary phase, the analytes will be eluted according to boiling point. A stronger van der Waal interaction means that the analyte will be attached to the stationary phase for a longer period, and thus the analytes with the higher boiling point will be eluted last. Thus smaller hydrocarbons will be eluted before the bigger hydrocarbons. Figure 3.1 shows a diagram of a GC.

In the flame ionization detector (FID) the eluate is burned in a mixture of hydrogen and air. Organic compounds form CHO^+ ions under reducing conditions in the flame.

$CH + O \longrightarrow CHO^+ + e^-$

This separation of charge sets up a current from the anode to the cathode and the current is the

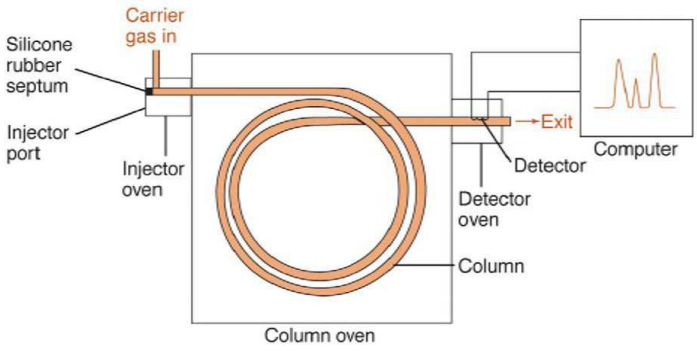

Figure 3.1: Schematic diagram of a GC [44]

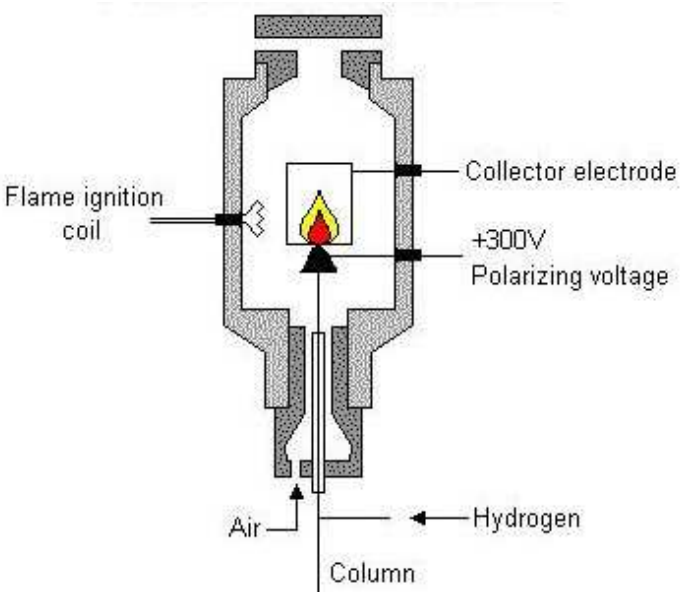

Figure 3.2: The flame ionization detector (FID) [43]

detector signal. The FID is thus a detector for carbon atoms. The carbon atoms in hydrocarbons have approximately the same response factor regardless of the type and size of the compound. Carbon atoms in oxygen containing compounds will have a different response factor and thus a calibration is required. The FID is schematically presented in Figure 3.2

3.2 Mass Spectroscopy - MS

Mass Spectroscopy (MS) is a technique that enables the study of the fragments of molecules and atoms. The molecules to be analyzed are passed through an electron beam, which strips of electron

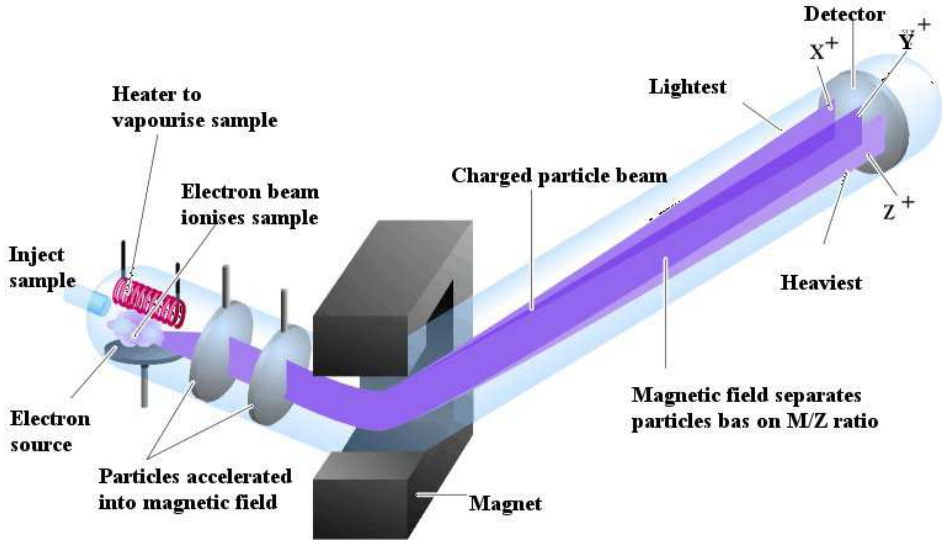

Figure 3.3: The principle of the Mass Spectrometer [45]

producing molecular ions, and also fragments the molecules into smaller parts:

$$A- > A^+ + e^- \tag{3.1}$$

$$A- > A^{2+} + 2\ e^- \tag{3.2}$$

$$A- > B^+ + C^+ + 2\ e^- \tag{3.3}$$

$$\tag{3.4}$$

The ions that are produced can also be fragmented further

$$A- > B^+ + C^+ + 2\ e^- \tag{3.5}$$

$$B^+- > D^+ \tag{3.6}$$

This fragmentation produces a complex spectrum which is unique for each molecule. The ions produced are then passed through an analyzer tube to the electron multiplier detector. In the analyzer tube the ions are subject to a magnetic field which bends the path of the ions according to the mass to charge ratio (M/Z). Varying the magnetic strength thus enables the collection of all the ions in a given range. Figure 3.3 shows the principle of Mass Spectrometry.

In connection to a GC a Mass Spectrometer may be used as a detector (GC/MS), and with reference to a database, the eluted peaks can thus be identified. In a GC/MS the whole spectrum of M/Z values are analyzed. It is also possible to chose only certain M/Z values to be monitored, called Selected Ion Monitoring. This is useful in for example analyzing the effluent of a catalytic reaction, when the products and reactants are known, but not the amount. In such a case, the analytes are not separated prior to analysis with the MS, and therefore the selected ions to be monitored should be chosen carefully. For example will the molecular ions of methanol and oxygen interfere, since both have mass 32. Methanol can be monitored with mass=31 (CH_3O^+ ion), which is non-existent in the O_2 spectrum. Selected ion monitoring improves the sensitivity of the technique by decreasing the response to all other ions (i.e. by reducing background noise) [46].

3.3 Scanning Electron Microscopy (SEM)

In scanning electron microscopy (SEM) the image is produced by an electron beam which is scanned across a sample, and then a signal which is produced by the interaction between the beam and the specimen is collected. The electron beam is focused on the surface and scanned in a series of lines and frames, which in total produce and image. There are different types of detectors, but once the signal is converted to an electric signal and amplified, it is displayed on a screen. The magnification is controlled by the strength of the lenses.

The beam path in a SEM is shown in Figure 3.4. The accelerating voltage is the voltage applied to the filament, which is the source of the electrons (when applied together with a small current). The accelerating voltage is usually in the range 5 kV to 20 kV. Conductive samples are most easily analyzed with SEM. If they are not conductive a negative charge on the electron beam might accumulate on the surface of the sample and thus affect the image, thus if the sample is not a good conductor, high voltages may not be used, since this will enhance surface charging. The electrons may be elastically reflected, without loss of energy (backscattered electrons), or absorbed, giving rise to the emition of secondary electrons of low energy + x-rays.

When preparing a sample it is important to make sure that the specimen is stuck on the carbon tape

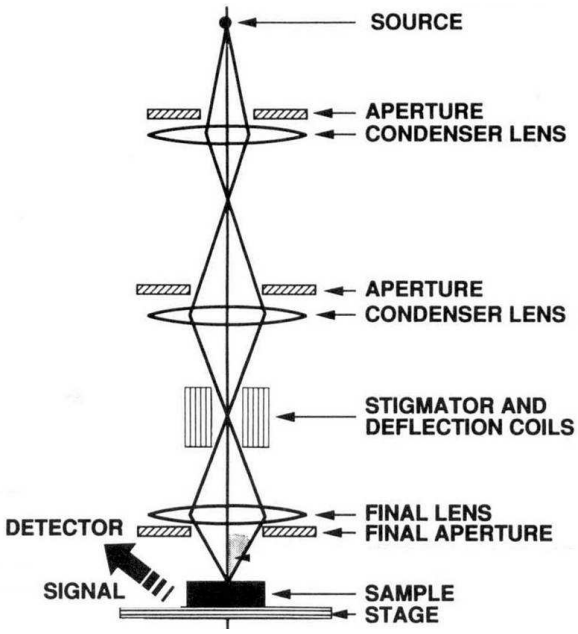

Figure 3.4: Schematic drawing of the lenses/beam-path in a SEM [47]

(or similar). Once the pressure is lowered in the chamber the sample may disappear from the sample-holder if it is not properly fastened. It is also important not to touch the sample since grease from the fingers may contaminate and change the surface of the specimen. Since the SEM uses electrons to produce an image, most conventional SEMs require that the samples be electrically conductive.

Zeolites are supramolecular sieves where the atoms are connected through covalent bonds. This means that there are no conductive electrons as in metals, and there is a risk of charge-up of the specimen when studying zeolites.

3.3.1 Energy Dispersive X-ray Spectroscopy(EDS)

When the electron beam hits the sample, characteristic x-rays are formed. The incoming electron interact with a core electron, providing enough energy for it to be emitted from the atom. The atom will then relax again by filling the resulting core hole with a valence electron, which will therefore reach a lower energetic state, and the surplus energy is released as x-rays. These x-rays have energies specific to the element since the energy-levels are element-specific. With an EDS detector, the intensity of x-rays at the different energies can be measured, and this gives a quantitative analysis of the different

elements in the sample.

3.4 Thermogravimetric Analysis (TGA)

By thermogravimetric analysis, the weight of a sample is monitored upon temperature change in controlled atmospheres. In an inert atmosphere, the decomposition of the material, as temperature is increased, may be studied. In this work O_2 was used to oxidize hydrocarbons to CO_2 and H_2O, and the scope of the analysis was to determine the amount of hydrocarbons deposited on the catalyst.

3.5 Reactors

There are several choices of reactors depending on the reaction conditions [49]. In a batch reactor catalyst and reactants are mixed in a closed tank (Figure 3.5). The reaction mixture might be stirred, but no reactants are added nor products removed during reaction. The concentration of reactants decreases with time. This type of reactor is most often used in homogeneous catalysis when the catalyst is not easily removed from the reaction mixture. A continuously stirred tank reactor (CSTR) is a batch reactor where reactants are added while products are removed continuously (Figure 3.6). In this reactor steady state conditions are obtained. The concentration ratios of reactants and products can be tuned by changing the flow in and out of the reactor. When reducing the flow the reactants stay longer in the reactor and have more time to react. The conditions should be adjusted depending on the rates of the primary and secondary reactions. The batch reactor and the CSTR are mostly used in homogeneous catalysis. When the CSTR reactor is used in heterogeneous catalysis the catalyst particles are very small and usually dispersed in liquid.

In heterogeneous catalysis the most common reactors are the fixed bed and the fluid bed reactors. In a fixed bed reactor the catalyst is deposited on a grid forming a bed and the reactants are fed through the bed from top to bottom. The length of a fixed bed reactor is analogous to time in a perfectly stirred batch reactor. This means that concentration of reactants decreases through the bed. The assumption is that each segment (in height) is completely stirred so that steady state conditions are present [50].

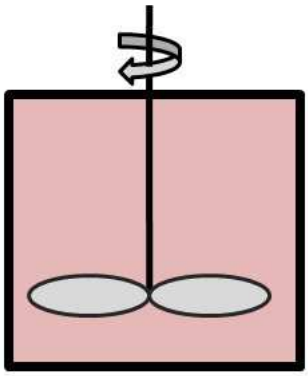

Figure 3.5: Batch reactor

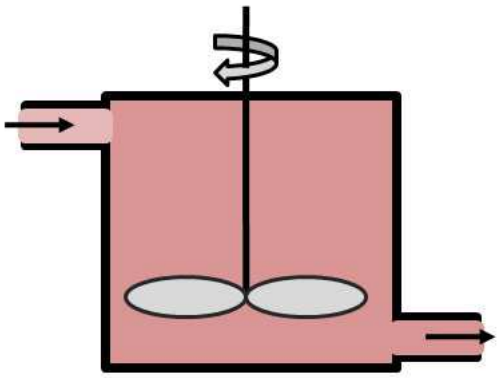

Figure 3.6: CSTR reactor

The advantages of a fixed bed reactor is that it is in theory a simple scale-up, that there is little back mixing of reactants and products, a simple low cost production and little mechanical stress on the catalyst. Disadvantages are poor heat control and a large pressure drop if the catalyst particles are too small. Also removing of spent catalyst for regeneration is not trivial without shutdown of the plant. Figure 3.7 show a simple diagram of a fluidized bed reactor.

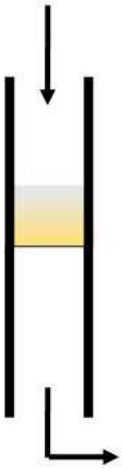

Figure 3.7: A fixed bed reactor

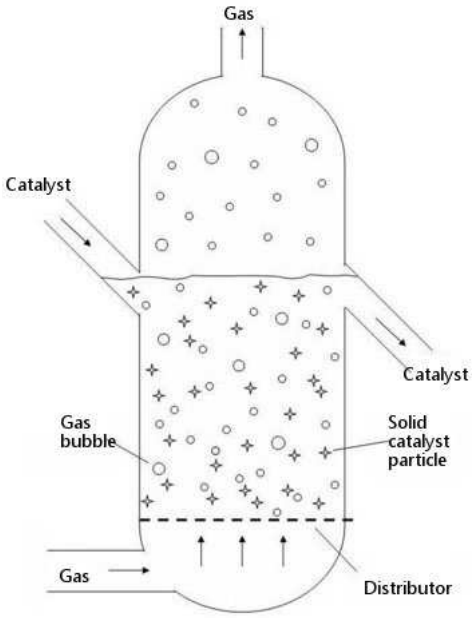

Figure 3.8: A fluidized bed reactor [51]

In the fluidized bed reactor the reactant gas flows from the bottom, making the catalyst powder behave like a boiling fluid with good mixture (Fig. 3.8). Effluent gas is removed from the top. Advantages with this reactor is that catalyst back mixing leads to high mechanical and thermal contact, and to

low temperature gradients. Also, the pressure drop over the catalyst bed is limited to the weight of the catalyst powder so that small particles may be used. Regeneration of the catalyst is easier in the fluidized bed reactor since the catalyst can be transferred to an external regenerator. Disadvantages of the fluidized bed reactor is that there is high mechanical erosion on catalyst and equipment as well as difficulties in scale-up. Other possible reactors are the monolith reactor and the reversible flow reactor.

The shape and size of the particle must be adjusted to the reactor type. For instance in a fluidized bed reactor the catalyst particles should be spherical to resist mechanical stress better. In a fixed bed reactor the catalyst particles should be big in order to minimize pressure drop over the bed.

Also, the catalyst should not plug the reactor, and diffusion paths should not be too long.

The above mentioned reactors are used on industrial scale. For a solid catalyst the fixed bed reactor is the most convenient reactor on the laboratory scale. The fluidized bed reactor is very difficult to make on a small scale, while the fixed bed is easily constructed also for very small systems.

Chapter 4

Background for calculations

The background for most quantum mechanical calculations in chemistry is the time-dependent Schrödinger equation

$$\hat{H}\,|\Psi\rangle = i\hbar\frac{\partial\,|\Psi\rangle}{\partial t} \tag{4.1}$$

In this equation $\hat{H}$ is the Hamiltonian which gives the total energy of the system when operated on the wavefunction of the system, $|\Psi\rangle$. The wavefunction contains *all* information about the system. The time-dependent Schrödinger equation describes the time-evolution of the system, and $|\Psi\rangle$ is a function of both position and time, $|\Psi\rangle = |\Psi(r,t)\rangle$. For many real systems the Hamilton operator does not depend on time, in which case equation 4.1 can be separated into a time-dependent and a time-independent part, i.e. the wavefunction can be separated such that $|\Psi(r,t)\rangle = |\psi(r)\rangle\,|\phi(t)\rangle = |\psi\rangle\,|\phi\rangle$. The time-dependent part of the wavefunction is given as

$$|\phi\rangle = e^{\frac{-iEt}{\hbar}} \tag{4.2}$$

The spatial part of the wavefunction can be solved through the time-independent Schrödinger equation

$$H\,|\psi\rangle = E\,|\psi\rangle \tag{4.3}$$

Equation 4.3 can be solved analytically for very few systems, in almost all cases it is not possible to find the exact solution. It should be mentioned that the energy E is a parameter for both the time-dependent and time-independent part of the wavefunction, so the time-dependency is more complicated than first suggested.

The variational principle states that

Theorem 1 *Given any approximate wavefunction satisfying the boundary conditions of the problem, the expectation value of the energy calculated from this function will always be higher than the true energy of the ground state. [52]*

Thus when comparing two possible wavefunctions the one with the lowest expectation value for the energy can be taken as the best wavefunction. This permits discrimination between two trial wavefunctions, and suggests an algorithm for solving the Schrödinger equation.

The variational principle provides the basis for Hartree-Fock theory which is an iterative method for obtaining a wavefunction. The first step in Hartree-Fock theory is to choose a trial-function, which is an antisymmetric product of one-electron functions (orbitals), and the iterative method consists in optimizing this product.

Antisymmetry is a requirement that follows from the Pauli principle, which says that no two fermions can have the same set of quantum numbers (be in the same state) at any given time. The first proposed wavefunction was the Hartree wavefunction, where the total wavefunction Ψ is the product of the spin-orbitals χ_n

$$\Psi(x_1, x_2, \cdots, x_N) = \chi_1(x_1)\chi_2(x_2)\cdots\chi_N(x_N) \tag{4.4}$$

where the numbering refers to the atoms, and x_n is the coordinate set for electron n. The Hartree wavefunction is not a satisfactory wavefunction because it is not antisymmetric. The criterion of

antisymmetry is fulfilled by the Slater determinant:

$$\Psi = \frac{1}{\sqrt{N!}} \begin{vmatrix} \chi_1(x_1) & \chi_2(x_1) & \cdots & \chi_N(x_1) \\ \chi_1(x_2) & \chi_2(x_2) & \cdots & \chi_N(x_2) \\ \vdots & \vdots & \ddots & \vdots \\ \chi_1(x_N) & \chi_2(x_N) & \cdots & \chi_N(x_N) \end{vmatrix} \tag{4.5}$$

Hartree-Fock theory uses the variational theorem to obtain the determinant that minimizes the total electronic energy.

4.1 Density Functional Theory (DFT)

Density Functional Theory (DFT) is a quantum mechanical method which is not based on the optimization of the wavefunctions, but the optimization of the electron density. The following two theorems, called the Hohenberg-Kohn theorems, provide the background of DFT.

Theorem 2 (HK 1) *The external potential, and hence the total energy, is a unique functional of the ground state electron density.*

Theorem 3 (HK2) *The ground state energy can be obtained variationally: the density that minimizes the total energy is the exact groundstate energy.*

Theorem 2 states that there is a one-to-one mapping between the ground state electron density and the external potential in the absence of degeneracy. Thus, the energy of the system may be obtained from the density of the system. Theorem 3 says that if we know the correct functional for the ground state density it can be optimized variationally. The density is only dependent on three spatial coordinates, while the wavefunction is a function of the coordinates of all the particles (N) in the system (3N spatial coordinates and N spin coordinates). This means that in order to calculate optimized energies we need not use the computationally expensive wavefunction methods, but the less expensive DFT

may be used to model bigger systems. Thus it is of use to develop methods that implement DFT for energy optimization (and later also other variables).

DFT, which has been developed from the Thomas-Fermi model, calculates the energy of a physical system by representing the energy as a functional of the electron density. The Thomas-Fermi model describes an interacting free electron gas and has the limitation that is does not take exchange and correlation energy into account. An improvement was later supplemented by Dirac, who included a functional for the exchange interaction, but this model was less accurate due to cancellation of error in the previous. One main problem in the Thomas-Fermi model is the poor representation of the kinetic energy, which was improved by Kohn and Sham who divided the kinetic energy functional into two parts, one of which can be calculated exactly, and a small correction term [53]. With the Hohenberg-Kohn theorems and the theory of Kohn and Sham DFT has developed into a quantitative tool for modeling real systems.

4.1.1 Kohn-Sham theory

So far we are concerned with a system of interacting particles, but it would be much easier to handle a system of non-interacting particles. It is possible to take a fictitious system of non-interacting electrons as as a starting point, and adjust it with and effective potential such that the non-interacting electrons have exactly the same density as a as the real, interacting electrons in the true potential. Kohn and Sham realized this and stated how starting from such fictitious non-interacting system it is possible to achieve the true total energy self-consistently. The Kohn-Sham approach is based on calculating the energy of the non-interacting particles and then correcting for the interaction approximately. Thus the biggest part of the energy is calculated exactly.

The energy functional can be written as

$$E_{DFT}[\rho] = T_S[\rho] + E_{ne}[\rho] + J[\rho] + E_{xc}[\rho] \tag{4.6}$$

where $T_S[\rho]$ is the kinetic energy assuming non-interacting electrons, $E_{ne}[\rho]$ is the attraction between

electrons and nuclei and $J[\rho]$ is the Coulomb part of the electron-electron repulsion. The $E_{xc}[\rho]$ is a term that takes into account the kinetic energy deriving from the interaction of the electrons, and all non-classical corrections to the electron-electron repulsion energy such as exchange and correlation contributions. The three first, non-interacting functionals can be calculated exactly, but the exchange term has to be approximated, and it is this approximation that introduces the errors in DFT.

In the theory of Kohn and Sham the electron density,ρ, is expressed as a sum of one-electron densities [54]:

$$\rho = \sum_{i=1}^{N} \langle \chi_i | \chi_i \rangle \tag{4.7}$$

and in this situation the first three terms in the energy become one-electron integrals, for instance the kinetic energy of the non-interacting reference system is

$$T_s = -\frac{1}{2} \sum_i \langle \chi_i | \nabla_i^2 | \chi_i \rangle \tag{4.8}$$

The Kohn-Sham one-electron operator is defined as

$$h_i^{KS} = -\frac{1}{2}\nabla_i^2 - \sum_k^{\text{nuclei}} \frac{Z_k}{|r_i - r_k|} + \int \frac{\rho(r')}{|r_i - r'|} dr' + V_{xc} \tag{4.9}$$

where V_{xc} is the functional derivative of exchange-correlation energy

$$V_{xc} = \frac{\delta E_{xc}}{\delta \rho} \tag{4.10}$$

Applying the one-electron operator (4.9) to the orbitals provides a set of pseudo-eigenvalue equations

$$h_i^{KS} \chi_i = \epsilon_i \chi_i \tag{4.11}$$

where χ_i are the eigenfunctions and ϵ_i the eigenvalues. This set of equations (the Kohn-Sham equations) are solved iteratively and the solutions (the Kohn-Sham orbitals) are one-electron functions that are used to construct the electron density (Eq. 4.7).

Several functionals for the exchange-correlation term have been developed. The Local Density Ap-

proximation (LDA) methods build on the uniform interacting electron gas, and thus assumes that the energy density at a single point is equal to the uniform electron gas with the same density. Local spin density approximation (LSDA) is LDA generalized to spin polarized systems. It is often advantageous to use LSDA, as opposed to LDA, also for non-polarized systems, because it easier to construct good approximative exchange-correlation functionals. The electron density in a molecule is usually far from uniform, so extending the description to include the gradient of the local density to the correlation functional should improve the description of the exchange functional. Thus, generalized gradient correction (GGA) extends LDA by also including the gradient of the density. Examples of such functionals are PBE and RPBE, which are used in this thesis. PBE is a functional with correlation from Perdew-Burke-Ernzerhof [55], and RPBE is revised PBE by Hammer et al. [56], where the latter has shown to give a better description of adsorption energies.

One problem with current DFT is that it describes non-valence electron excitations poorly, and also does not treat van der Waal forces very well. Thus dispersion-induced attraction is not properly modeled, and such distances are usually over-estimated. Also, hydrogen bonds are, as a rule, too short [57].

Although both Hartree-Fock and DFT equations are solved in a very similar self-consistent manner, they are fundamentally different in that Hartree-Fock is an approximate model that can (at least in principle) be solved exactly, while DFT is an exact model that can only be solved approximately. This is because in Hartree-Fock the electron correlation is omitted while in the theory of DFT it is included. Electron correlation cannot be calculated exactly and thus an approximate functional has to used in DFT.

Density functional theory has developed into a powerful tool for the investigation of surface reactions, and has by now been applied in the development and optimization of real catalytic systems [58, 59].

4.2 Theoretical investigations of the MTO reactions and catalysts

Several studies have been performed on possible reactions in the MTO-process. There are very many different compounds present within the zeolite catalyst during the MTH-process, and theoretical investigations have been performed to study the possibility of how some of these compounds may be linked through reactions.

Quantum mechanical calculations demand a lot of computer resources, and the more atoms that are included into the calculation the more time-consuming it is. Therefore initial studies on acidic zeolites were performed on only small gas-phase clusters without reference to specific materials. Such studies do not take into account the zeolite framework with channels and cages, and therefore cannot say anything about the steric influence of the framework on the reactions. With better computers and the use of periodic boundary conditions (PBCs) as well as density functional theory (DFT) it is now possible to study bigger systems. Chabazite has been widely used for theoretical calculations as its smallest unit cell is of only 12 T atoms, and thus 24 atoms in total. This is a quite small unit cell compared to many other zeolite frameworks (H-ZSM-5 has 288 atoms in the unit cell). Also, as explained in the introduction all T-atoms in the chabazite framework are topologically equivalent, and therefore the introduction of on Al in the structure gives only four possible acid sites. In, for instance, H-ZSM-5 there are 12 different T-atoms which increases the number of possible acid sites dramatically.

Shah et al. compared the acidity of H-SSZ-13 and H-SAPO-34 with DFT by adsorption of methanol on the acid site. They found that at low partial pressures of methanol, only the zeolite can protonate it, while H-SAPO-34 is not acidic enough [60, 61].

Calculations of the adsorption and vibrational properties of CO on mordenite (a zeolite with a different topology) have also been performed[62]. It was found that the PW gradient-corrected functional (PW91 and PBE) overestimate the frequency shifts and that the revised Perdew-Burke-Ernzerhof (RPBE) functional gives a better description of hydrogen bonding. The RPBE functional has therefore been used for CO adsorption on H-SSZ-13 and H-SAPO-34 in this thesis. PBE was used otherwise.

Adsorption energies are calculated as

$$E_{\text{ads}} = E_{\text{structure+MeOH}} - (E_{\text{structure}} + E_{\text{MeOH in unit cell}}) \tag{4.12}$$

Chapter 5

Experimental setup

5.1 Catalyst

In this study the catalysts H-SAPO-34 and H-SSZ-13 were compared. The catalysts were provided by SINTEF, Oslo. Catalyst syntheses were based on conventional methods [39, 63], and characterized by XRD. Table 5.1 lists the catalyst batches and crystal size.

H-SAPO-34		H-SSZ-13	
batch name	particle size	batch name	particle size
ABA217	0.1 - 2 μm	KP	0.5 - 4 μm
MHN06	0.5 - 2 μm	CHA07	0.5 - 4 μm
		CHA09	0.5 - 2

Table 5.1: Batches used in the catalytic testing.

The H-SSZ-13 was synthesized with a Si/Al ratio of 11 which is equivalent to one acid site per cage. The same ratio was obtained in the SAPO-34 (Al+P/Si= 11), so that the number of acid sites was equal for the two materials. This was achieved by direct synthesis, without post-synthetic dealumination.

Also, the crystal sizes of the two structures should be similar in order to minimize possible effects due to diffusion. The crystal sizes and morphologies were investigated by scanning electron microscopy (SEM), and transmission electron microscopy (TEM) for a few deactivated samples. TEM was per-

formed to investigate graphite deposited on the surface. In addition, IR studies were performed to assess acid strength.

All catalysts were calcined at 550 °C, and then ion exchanged and calcined again in order to obtain the protonated form of the zeolite/zeotype. This thesis only includes catalytic testing and some characterization performed after the ion-exchange procedure. Before catalytic testing the material was pressed and sieved to 0.240-0.450 mm particle size.

5.2 Characterization Methods

Scanning Electron Microscopy was performed on all the tested catalyst batches to determine particle size and shape. The instrument was a Scanning Electron Microscope FEI Quanta 200 FEG-ESEM with EDS. It had both a backscatter detector and an Evert-Thornley detector (secondary ion), and both these signals could be mixed in various amounts. For H-SAPO-34 and H-SSZ-13 mixing the signals 50/50 was often found to be the best.

A circular sample-holder was covered with double-sided carbon tape, and then a thin layer of the zeolite was deposited on top. This was done by sprinkling the powder on the tape. The sample-holder was then shaken to remove loose particles. If the particles are not well attached on the carbon tape there is a risk that they will detach in vacuum or when the electron beam hits.

The field strength was usually kept at 10-12 kV, but sometimes also lower. Usually, higher voltages give higher resolution, but since these zeolites are not conductive, the voltages could not be set too high.

EDS was performed on CHA07 and ABA217 to determine Si/Al or (Al+P)/Si ratios on the surface of the crystals.

TEM and IR investigations were performed at Haldor Topsøe in Lyngby, Denmark and by the Zecchina group at the University of Torino, Italy.

5.3 Catalytic testing

In order to investigate the effect of temperature on the MTO-reaction over H-SAPO-34, a series of experiments were performed at varying temperature; 300 °C, 350 °C, 400 °C and 450 °C. Effluent gas was analyzed by gas chromatography after 10 minutes and then at intervals of about 22 min by automatic sampling. This only permitted point wise measurements and no monitoring of continuous changes with time. WHSV was 6.0 hr^{-1} and the reaction was stopped after 5 hours. Table 5.2 shows reactor conditions for the temperature-series.

Mass of catalyst	100 mg
Feed	Methanol
WHSV	6.0 g MeOH/(g catalyst h)
Carrier gas	He
H-SAPO-34	
Catalyst batch	ABA217
Temperature (°C)	300, 350, 400, 450
H-SSZ-13	
Catalyst batch	
Temperature (°C)	400

Table 5.2: Test conditions for the temperature-series

There were some difficulties in producing small enough H-SSZ-13 particles, and the first successful batch was only sufficient to make one experiment at 400 °C, chosen because this was the optimum temperature for H-SAPO-34.

A study at short times on stream was performed for both catalysts at 300, 325, 350, 375 and 400 °C. The amount of catalyst was 60 mg and flow conditions were scaled to keep WHSV = 6.0 hr^{-1}. At each temperature one long test was run until (nearly) complete deactivation, and also 5 short tests. One effluent analysis was performed for each test and thereafter quenched for analysis of deposits. Table 5.3 gives an account of all the tests made and which catalyst batch was used.

Also some flushing experiments were performed. In these studies methanol was fed for a predefined amount of time and then flushed with carrier gas before quenching. Such flushing experiments were done at 300 and 350°C.

H-SAPO-34		
Time of analysis	Quench time	Catalyst batch at different temperatures
3	5	ABA217 (all temperatures)
5	10	ABA217 (all temperatures)
10	15	ABA217 (all temperatures)
15	20	ABA217 (all temperatures)
20	25	ABA217 (all temperatures)
long test		ABA217 (all temperatures)
H-SSZ-13		
3	5	CHA07 (all temperatures)
5	10	CHA07 (all temperatures)
10	15	CHA07 (all temperatures)
15	20	CHA07 (all temperatures), CHA09 (400 °C)
20	25	ABA217, all temperatures
long test		CHA07 (all temperatures), CHA09 (400 °C)

Table 5.3: Setup for short tests, and batches used for each experiment. The temperatures are 300, 325, 350, 375 and 400 °C. The long test was run until full deactivation or nearly full deactivation.

In order to study the effect of varying residence time, a temperature series performed by halving the amount of catalyst, thus doubling the WHSV. All other settings were kept the same as in prior experiments.

5.3.1 Test rig - reactor test conditions

The testrig is shown schematically in figure 5.1.

The carrier gas was He, and the gas flow was controlled by Porter P150 flowmeters. Since the feed, methanol, was a liquid, the carrier gas was bubbled through a saturation evaporator. The partial pressure of the feed was controlled by adjusting the temperature of the waterbath surrounding the saturation evaporator. This was sufficient since the temperatures needed were quite near room temperature (around 20 °C).

The reactor was shaped as a u-tube, with inlet, outlet and septum for insertion of the thermocouple. For the temperature-series, where 100 mg of catalyst was used, the reactor in figure 5.2a was used. It was then decided to use a reactor such as that in figure 5.2b in order to diminish the dead volume. The

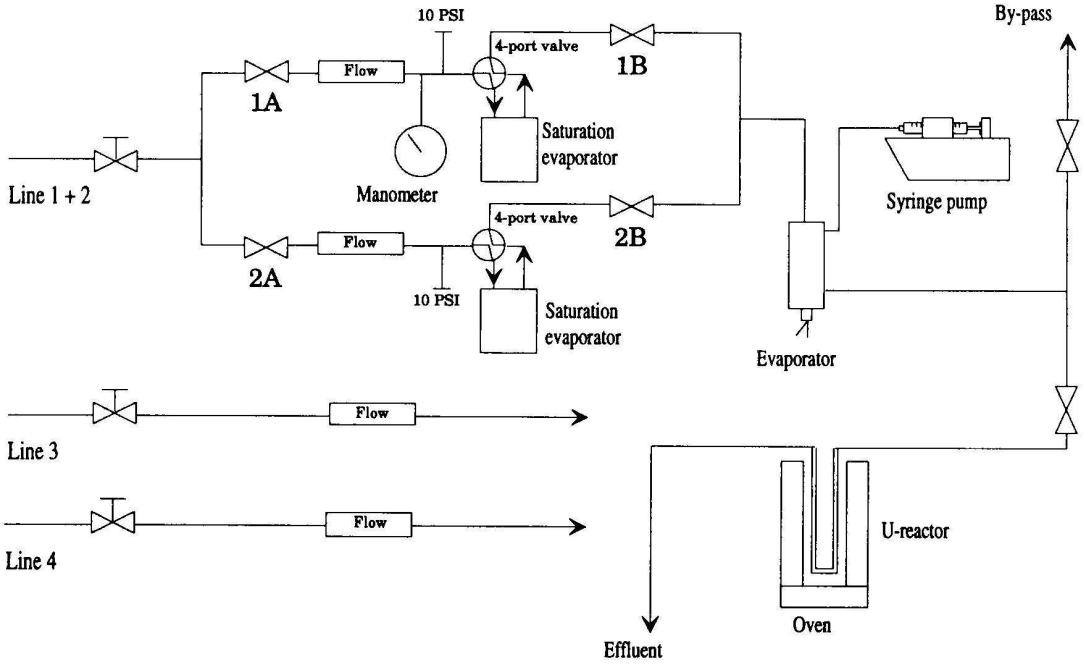

Figure 5.1: Schematic representation of the testrig.

size of the bed was the same in both reactors, 10 mm in inner diameter. The catalyst particles were fractionated to 0.420-0.250 mm. The thermocouple placed in the catalyst bed was 1.5 mm thick.

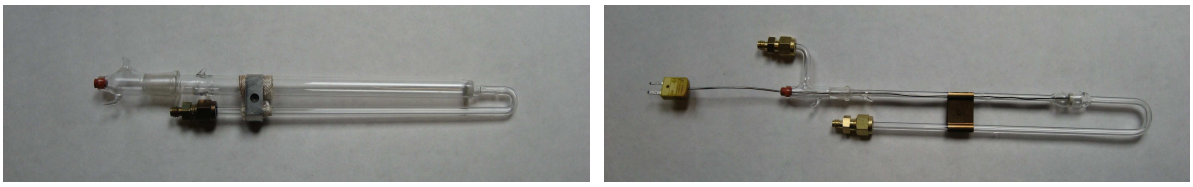

(a) **(b)**

Figure 5.2: (a) Reactor used for temperature-series (b)Reactor used for all other catalytic tests

After switching on the feed, the first GC analysis was performed by manual trigger after a predefined time, usually 10 minutes. When MS analysis was performed the instrument was online during the whole test. When the sample was quenched, it was quickly transferred from the hot glass-reactor (taken out of the oven) to a sample vial.

5.3.2 GC - Gas Chromatography

The effluent stream was analyzed by a Gas Chromatograph and a Mass Spectrometer. Two different GCs were used. One was a Carlo Erba 6000 Vega 2 GC with FID detector and automatic sampling. This GC was replaced by an Agilent 6890 A GC, also with FID detector and automatic sampling. The capillary column from the former GC was transferred to the latter, but different temperature programs where used as seen in table 5.4. The column was Supelco SPB-5 capillary column, 60 m long, 0.530 mm in diameter and a 3 μm thick stationary phase. The pressure of the carrier gas was 42 kPa for both GCs.

Carlo Erba			Agilent		
Ramp (°C/min)	Temp (°C)	Hold time (min)	Ramp (°C/min)	Temp (°C)	Hold time (min)
	50	5		45	5
15	185	0	25	260	0
Total time		14.0	Total time		13.6

Table 5.4: Temperature programs used for the Carlo Erba and Agilent Gas Chromatographs.

Since the GC was only analyzing the composition of the effluent, differences in the temperature program (or other part of the GC) did not influence the results of the experiments, as the the same peaks were separated in both instruments. The temperatures series and the short tests at 300 °C were performed on the Carlo Erba GC, while all other tests were performed after installation of the Agilent GC.

Figure 5.3 shows a typical chromatogram for the GC analysis. The big chromatogram is over the whole analysis time of 13.6 min, while the insert shows the part where most of the products are eluted, with identified peaks labelled. This setup was not able to separate ethane from ethene, nor propane from propene, and these peaks are therefore only labelled C2 and C3, respectively.

The main products of the MTO-reaction over H-SSZ-13 and H-SAPO-34 are alkanes and alkenes in the C1 to C4 range. All hydrocarbons up to C4 were identified by the gas chromatograph, while C5 and C6 products were lumped together and only treated as a group in the integration. Table 5.5 shows the identified peaks and retention times for the Agilent GC. The channels in the chabazite framework

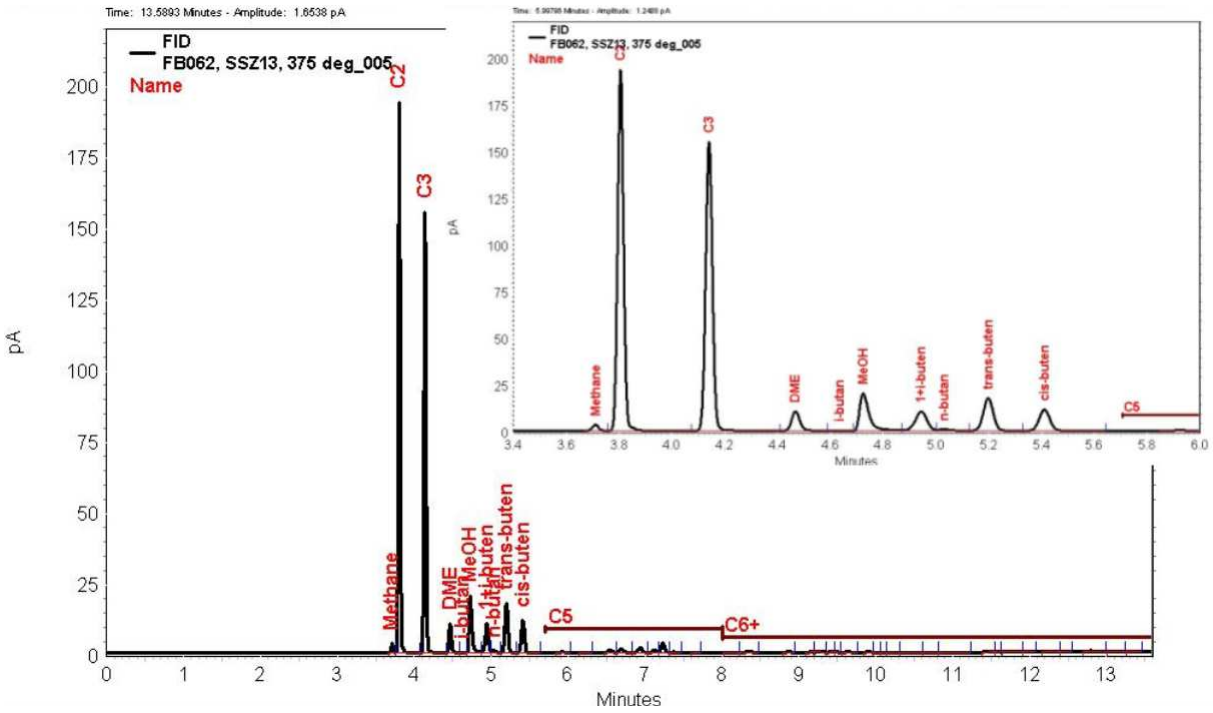

Figure 5.3: Total chromatogram over the whole range of the analysis (13.6 min), the insert shows the part of the chromatogram where most products are eluted, from 3.4 to 6 minutes. In both chromatograms identified peaks are labelled.

were so small that no bigger products than C6-hydrocarbons were present in the effluent.

Compound(s)	Retention time (min)
Methane	3.71
Ethane+ethene (C2)	3.81
Propane+propene (C3)	4.14
Dimethyl ether	4.47
iso-butane	4.64
Methanol	4.72
1-butene + iso-butene	4.95
n-butane	5.03
trans-butene	5.20
cis-butene	5.41
C5	5.70 - 8.00
C6	8.00 - 13.60

Table 5.5: Identified compounds and their retention times on the Agilent GC.

5.3.3 MS - Mass Spectrometry

The effluent was analyzed by MS during the long running tests. This was done because the more accurate (quantitative) GC-analyses could only be done with at least 20 minute intervals, while MS-analysis of each ion was done at intervals of approximately 17 seconds, and thus gave an indication of what happened between the GC-points. The instrument used for the MS analyses was a Pfeiffer Vacuum Omnistar GSD 301 02.

Table 5.6 shows the masses that were chosen and which molecules may correspond to these values.

M/Z	molecule/ion
4	Helium
16	Methane
18	H_2O^+
25	C_2H^+
26	$C_2H_2^+$
27	$C_2H_3^+$
28	$C_2H_4^+$, N_2^+
29	$C_2H_5^+$
30	CO^+
31	CH_3O^+ methanol fragment
32	Methanol, O_2^+
42	$C_3H_6^+$
44	$C_3H_8^+$
46	Dimethyl ether (DME)
56	$C_4H_8^+$
58	$C_4H_{10}^+$

Table 5.6: Measured M/Z values and corresponding molecules/ions

M/Z = 31 (CH_3O^+) was used as the methanol peak since 32 (CH_3OH^+) also corresponds to O_2^+. No hydrocarbons can fragment into ions with mass 31, and since the product spectrum of the reaction contained only hydrocarbons, the 31 peak was only a measure of methanol. M/Z = 46, the ratio of the molecular ion, was used for DME. In the table only ions with charge +1 are considered, and none of the hydrocarbons detected in the effluent could fragments with mass 46 and charge +1.

When performing the MS analysis it was important to obtain a new baseline every time. Therefore after quench an empty reactor or swagelock connection was put in place of the reactor to measure the

signal of the methanol feed alone. The MS data was calibrated every time with a corresponding GC analysis.

5.3.4 Analysis of deposits/coke

As previously described zeolites are microporous structures with channels and cavities where molecules may be trapped. In order to analyze these molecules the zeolite framework had to be dissolved.

Dissolution Procedure

In order to analyze the trapped species in the zeolite, 15 mg of zeolite submitted to testing was dissolved in 1 mL 15% HF. Teflon tubes were used since glass is dissolved by HF acid. The zeolite was dissolved after 30-60 minutes. Shining light through the teflon tube from the bottom with a torch easily showed if all was dissolved and, if not, a little shaking of the tube while closed often helped. If the sample was heavily coked the outer coke did not dissolve. The previously trapped organic material was extracted with CH_2Cl_2. 1 μL of the extract was analyzed in an Agilent 6890N Gas chromatograph connected to the Agilent 5793 Mass Selective Detector (GC/MS). Split varied from 1:5 to 1:30, increasing the split when the detector or column was overloaded. Table 5.7 shows the temperature program used.

Ramp (°C/min)	Temperature (°C)	Hold time (min)
	10	3
10	300	15
Total time per run (min)		47

Table 5.7: Temperature program used with the GCMS for analyzing retained material.

The solvent used for extraction contained C_2Cl_6 as internal standard. The solvent with the extracted material was transfered to a vial before injection. In order for the automated sampler to reach the sample the inner part of the vial was conical and was only 300 μL in volume.

The peaks in the chromatogram were analyzed using the NIST98 database for the fragmentation in the MS. This is a very thorough database and most major peaks were identified. Smaller peaks were not so easily assigned, especially when there was partial overlap between neighbouring peaks.

Thermogravimetric analysis - TGA

Thermogravimetric analysis (TGA) was performed on the (partially) spent catalyst to determine the total weight percent of deposited coke. A Rheometric Scientific STA 1500 instrument was used for the TGA. 10-15 mg catalyst plus coke was placed in an Al_2O_3 crucible and heated in oxygen from 25 to 550 °C with a heating rate of 5° C/min, and then kept at 550° C for 60 min. Weight-loss could thus be measured, and fig 5.4 shows a typical curve for the TG analysis.

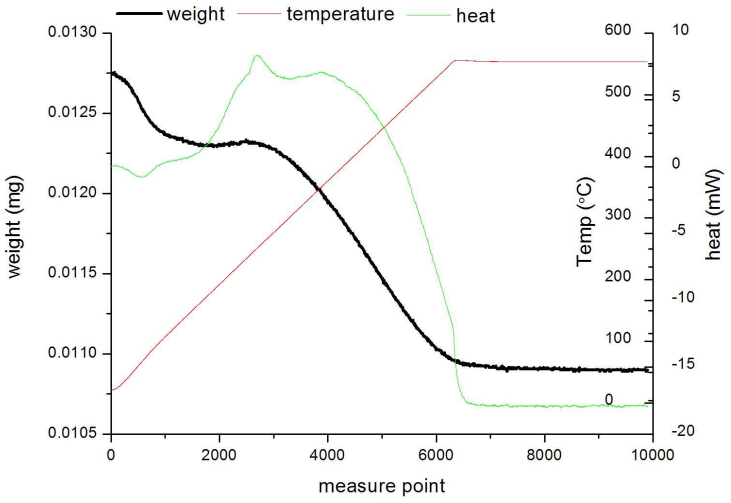

Figure 5.4: Typical curve from thermogravimetric analysis Green line shows heat output (mW), red line the temperature (°C) and the black line the weight of the sample (g).

The left axis shows the range of the weight, and the ranges of both heat output (-20 to +10 mW) and temperature (-50 to 600 °C) are shown on the right axis. The heat curve was a good indication of the thermal properties of the process going on. In figure 5.4 a dip in correspondence to the first weight-loss is seen, which is consistent with the endothermic vaporation of water, while heat was released in the second weight loss when the hydrocarbons were burnt. The amount of deposited coke is given as

gram coke per gram catalyst and was calculated according to equation 5.1

$$\text{amount of coke} = \frac{\text{g coke}}{\text{g catalyst}} = \frac{m_{\text{coke + catalyst}} - m_{\text{catalyst}}}{m_{\text{catalyst}}} \tag{5.1}$$

where $m_{\text{coke+catalyst}}$ is the mass at the first plateau in the spectrum and m_{catalyst} the final mass. The first plateau was taken as the mass of coke plus catalyst, and the initial loss of weight was due to removal of water.

Chapter 6

Results and discussion of experimental work

6.1 Characterization

All catalyst batches were characterized by XRD before and after calcination, prior to the work in this thesis.

SEM pictures showed the H-SAPO-34 to have cubic crystals ranging from 0.2 to 2μm in size (Fig. 6.1b). There was also some smaller "powder" around the crystals. The H-SSZ-13 crystals were more spherical (Fig. 6.1a), but in the same size range. It was very difficult to take clear pictures of the samples, especially chabazite. This was probably due to charging of the surface, since zeolites and zeotypes are not conductive. The batches used in these tests were not very uniform, and this means that there were differences in the crystals of the two catalysts. However the crystal sizes were in the same size range and therefore still comparable.

EDS analyses were performed on CHA07 and ABA217 to study the Si/Al and (Al+P)/Si ratios in the H-SSZ-13 and H-SAPO-34 samples, respectively. Table 6.1 shows the result of this analysis. The Si/Al ratio for H-SSZ-13 and corresponding (Al+P)/Si for H-SAPO-34 is a measure of the density of

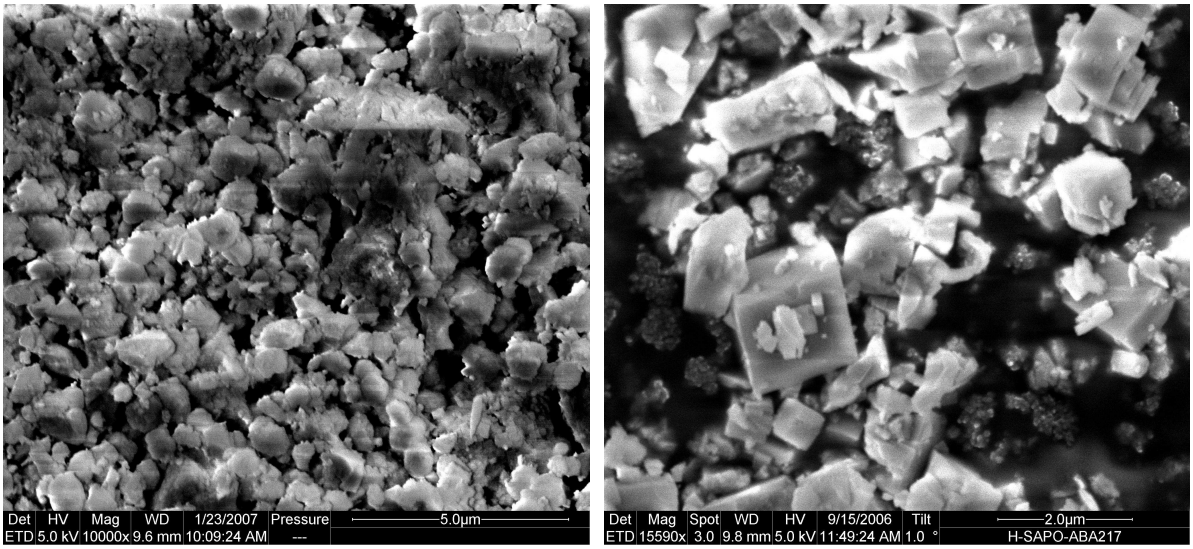

(a) **(b)**

Figure 6.1: SEM pictures of (a)CHA07 (H-SSZ-13) and (b) ABA217 (H-SAPO-34). Note the different length scales.

Table 6.1: Si/Al or (Al+P)/Si ratios on the surface of CHA07 and ABA217, measured by EDS

Catalyst (batch)	point of analysis	Si/Al or (Al+P)/Si
H-SSZ-13 (CHA07)	scan over many particles	9.9
H-SAPO-34 (ABA217)	scan over many particles	10.2
H-SAPO-34 (ABA217)	scan over many particles	10.0 small traces of Na/K
H-SAPO-34 (ABA217)	point on big crystal	8.6
H-SAPO-34 (ABA217)	point on what looks like small amorphous material	19.9

acid sites in the zeolite/zeotype; 11 corresponds to one acid site per cage. The synthesis procedure anticipated a ratio of 11, but in all the EDS analyses of the crystals it was lower. This indicated a higher density of acid sites, but the deviation was not very big. Remembering that the surface will always loose some of the crystallinity of the material it was not surprising that this ratio deviated from the expected. EDS analyses were made on specific spots of the sample as well as an average over whole pictures at 10000x magnification (area of around 12x12 μm). In one of the averaging pictures traces of Na and K were detected, but the point source of this impurity was not found. The small amorphous-looking material had a higher Si/Al ratio, which indicated that the Al had a higher tendency to grow into the crystals than remain in the amorphous material. Both catalysts deviated in the same direction, so the assumption of similar acid site densities was still valid, according to EDS.

ICP analyses gave a Si/Al ratio of 12.7 and 13.3 for CHA09 and CHA07, respectively. This showed that the total Al content was lower than expected, corresponding to a lower acid site density, and so this deviation was opposite of what was observed in the EDS-analyses. However, the latter showed differences in the crystals and the amorphous-looking material, and so the Si/Al in the actual crystals may have been lower than indicated by ICP. The lower ratio obtained by EDS suggested a higher density of acid sites on the surface, compared to the inner part of the crystal.

IR spectroscopy was performed on CHA07 and ABA217 by the Zecchina group at the University of Torino in order to study the acidity of the two catalysts. H-SAPO-34 was slightly less acidic than H-SSZ-13; the difference in CO shift upon adsorption was 40-44 cm^{-1} [64]. Also the samples used in the present work had few silanol groups indicating little framework defects (silanol nests).

6.2 Stability tests of H-SSZ-13 and H-SAPO-34

An ideal catalyst is unaltered at the end of the reaction and can thus be reutilized endlessly. This is however not true for real catalysts which eventually deactivate after a certain number of cycles, due to side reactions. The lifetime of the catalysts is therefore limited, and it changes depending on the reaction conditions. In this thesis, the conversion is given as percentage of methanol converted to non-oxygenate products at any given time on stream, and the stability of the catalyst refers to the time of high conversion before onset of deactivation. Thus, higher stability corresponds to longer time on stream before the activity declines.

The stability of H-SAPO-34 as a catalyst for the MTO reaction, WHSV=6.0 g g^{-1} hr^{-1}, with respect to time on stream, is shown in Fig. 6.2, for various temperatures. The temperatures range from 300 to 450°C with 50°C intervals. One test with H-SSZ-13 was included at the optimum temperature of H-SAPO-34 for comparison.

The lowest stability was observed at 300°C, with a clear induction period up to maximum conversion of only 30% after 30 minutes on stream. The deactivation was then rapid. At 350°C the stability improved, and nearly full conversion was observed already at the first analysis after 10 minutes of

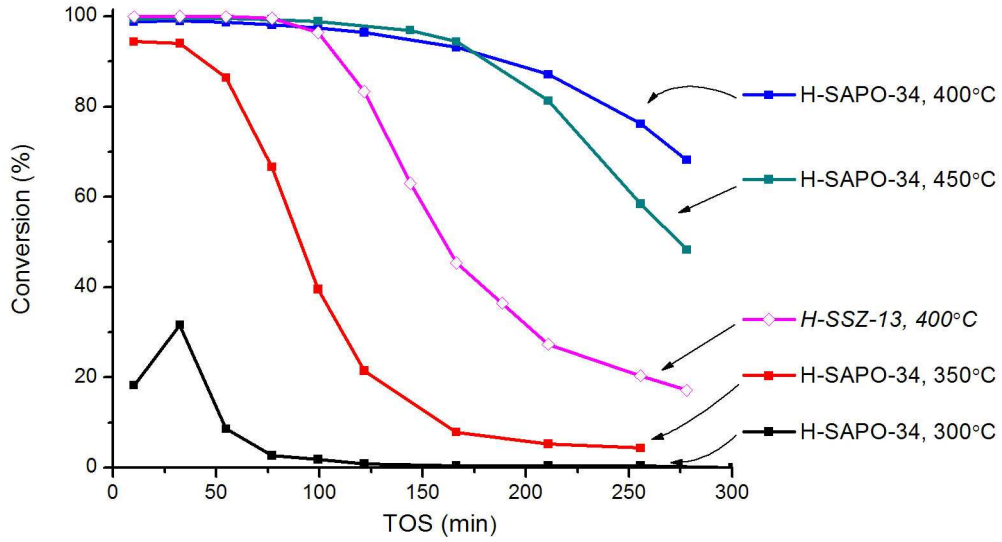

Figure 6.2: Conversion of methanol over H-SAPO-34 at 300, 350, 400 and 400°C, and over H-SSZ-13 at 400°C.

methanol feed. Here, the induction period was no longer observable, while deactivation was rapid. The highest capacity for converting methanol was observed at 400°C. At this temperature the initial conversion was 100% and after 278 minutes (last analysis before quench) the activity was still at 70% conversion. At even higher temperature (450°) the initial conversion was 100%, but the activity declined faster. Lower temperatures were not tested since some activity was necessary for studying the reaction; at 300°C the maximum conversion reached was only 30% and the lifetime of the catalyst was very short. Since there was only enough catalyst to perform one test with H-SSZ-13 the optimum catalytic temperature for H-SAPO-34 was chosen. H-SSZ-13 reached full conversion at 400°C, but it started deactivating faster than H-SAPO-34 both at its optimum temperature and at 450°C. However, H-SSZ-13 might have had a higher conversion capacity in the beginning, so that at higher space velocities the total methanol converted would be the same. At higher space velocities the residence time of the reactants in the catalyst bed would be shorter, possibly preventing secondary reactions. If the higher acidity in H-SSZ-13 made the product-forming reactions go faster, probably also coke was formed more rapidly than in H-SAPO-34. This means that at shorter residence time H-SSZ-13 might have the same methanol conversion capacity as H-SAPO-34 at longer residence time.

Figure 6.3 shows the composition of the hydrocarbons retained inside the cages after 5 hours of methanol feed at different temperatures. The chromatograms were calibrated by means of C_2Cl_6 as

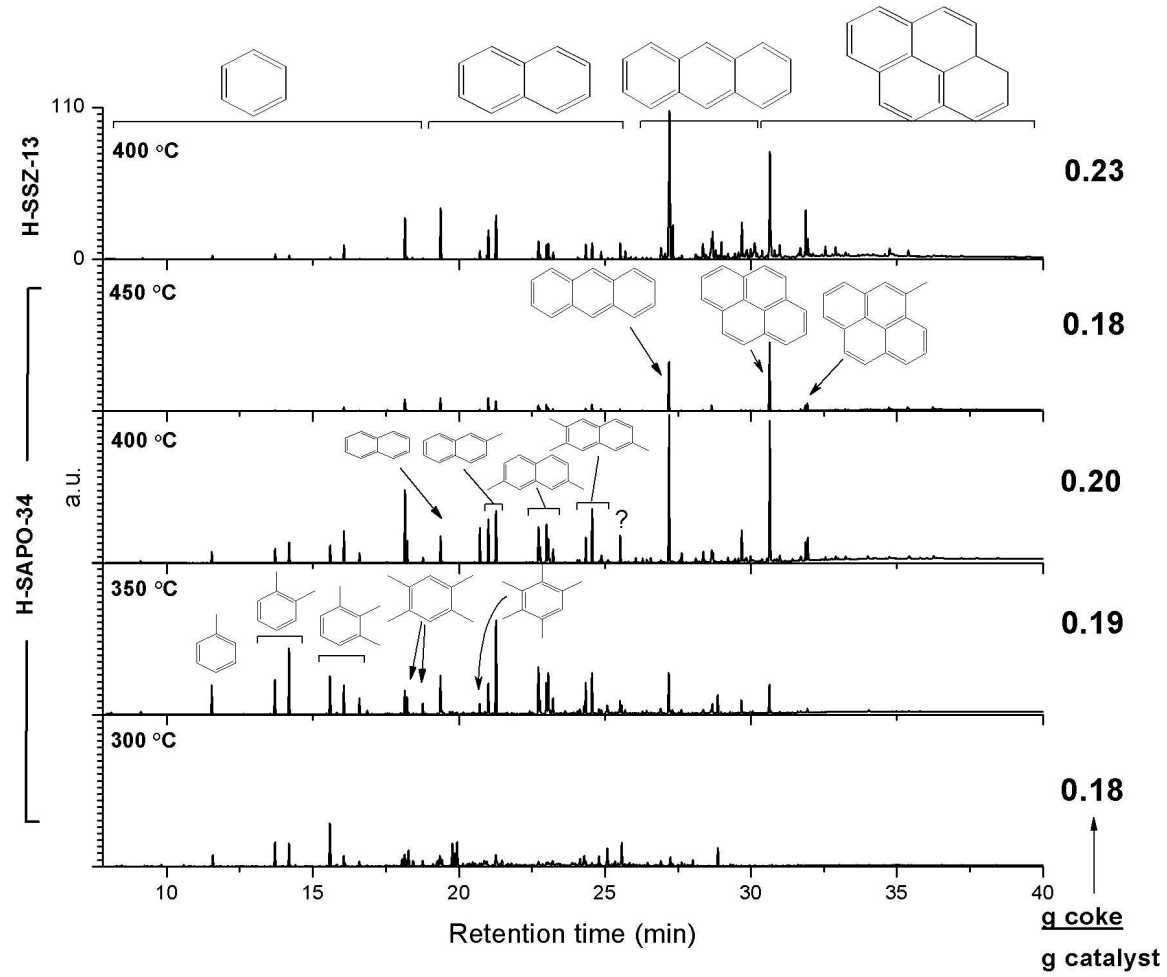

Figure 6.3: Composition of retained hydrocarbons and total amount of coke (right) after 300 minutes on stream. In this, and in the following figures, the intensities of the peaks are calibrated relative to the height of an internal standard C_2Cl_6, which is set to be 1 (a.u.).

an internal standard, and are thus directly comparable. The analyses were made after dissolving the catalyst in HF and extracting the hydrocarbons in CH_2Cl_2. The total amount of retained hydrocarbons soluble in dichloromethane was least for H-SAPO-34 at 300°C. This was consistent with there being little methanol conversion at this temperature: low conversion of methanol also meant little production of retained hydrocarbons, as well as little production of the desired products. The amount of soluble hydrocarbons increased with temperature up to 400°C, while after 5 hours at 450°C there were almost no soluble hydrocarbons at all. However, the relative amount of heavy hydrocarbons increased with temperature compared to the lighter aromatic rings. The major compounds detected at 300°C were methylated benzenes, while there was a substantial increase of methylated naphtalenes at 350°C. At

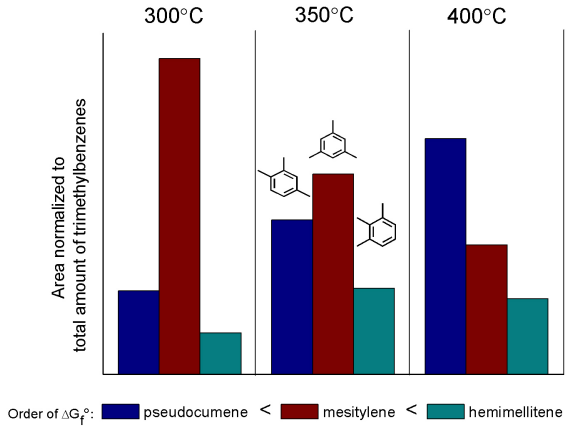

Figure 6.4: The amount of the three trimethylbenzenes in the cages of H-SAPO-34 after feeding with methanol for five hours at 300, 350 and 400°C, relative to the total amount of trimethylbenzenes at each temperature.

400°C the two main peaks represented three and four aromatic rings, and at 450°C these were almost the only compounds present. Also, the total amount of hydrocarbons had decreased relative to 400°C. The chromatogram for H-SSZ-13 at 400°C was quite similar to that of H-SAPO-34 at the same temperature, but with a shift towards heavier compounds. The differences were not very pronounced, even though the activity after 5 hours was only 20% for H-SSZ-13 and 70% for H-SAPO-34. The total amount of soluble hydrocarbons increased with temperature up to the optimum temperature (400°C) for H-SAPO-34, and, by increasing the temperature further, the total amount of soluble hydrocarbons decreased considerably. The fact that there was so little soluble hydrocarbons at 450°C indicated that the reactions forming deactivating hydrocarbons was very fast here, and that insoluble coke had been formed. Three- and four-ring aromatics being the main compounds detected also suggested this.

All three tri-methylbenzenes were present in detectable amounts in the soluble hydrocarbons, as observed for 300, 350 and 400°C in Figure 6.3, which made it possible to identify which peak corresponded to which compound according to boiling point (the NIST98 database did not discriminate between the different trimethylbenzenes). When going from 300 to 400°C the relative amounts of the trimethylbenzenes changed (Fig. 6.4). At the lowest temperature there was mainly 1,3,5-trimethylbenzene (mesitylene), while at 400°C the was most 1,2,4-trimethylbenzene (pseudocumene). A higher temperature should give a distribution closer to thermodynamic equilibrium, dictated by the

Gibbs free energy of formation, which at the studied temperature is in the order

$$\Delta G_f^\circ(\text{pseudocumene}) < \Delta G_f^\circ(\text{mesitylene}) < \Delta G_f^\circ(\text{hemimellitene}) \tag{6.1}$$

The distribution deviated from thermodynamics at lower temperatures giving more mesitylene (the molecule with highest symmetry). This observation suggested that this compound was more easily formed inside the cages of the catalyst.

The thermogravimetric analysis (TGA) give the total amount of deposited hydrocarbons, and is given as g(coke)/g(catalyst) after quench (right hand column in Fig. 6.3). The total amount of hydrocarbons produced after 5 hours was less at 450°C compared to 400°C, even though the sample was more deactivated.

6.3 Study at short times on stream

Experiments where the catalyst system was quenched after short times on stream were performed. This permitted to study deposited products in more detail. Since the amount of catalyst was limited, the experiments were scaled down to 60 mg catalyst as opposed to the previous 100 mg. The WHSV remained the same (6.0 hr^{-1}). Figure 6.5 shows that methanol conversion capacity with 100 mg catalyst at 300, 350 and 400°C was higher than when using 60 g catalyst. There are possibly many reasons for this, and a proper investigation of it was outside the scope of this thesis. It is however important to keep in mind that catalytic tests at different scales are not directly comparable.

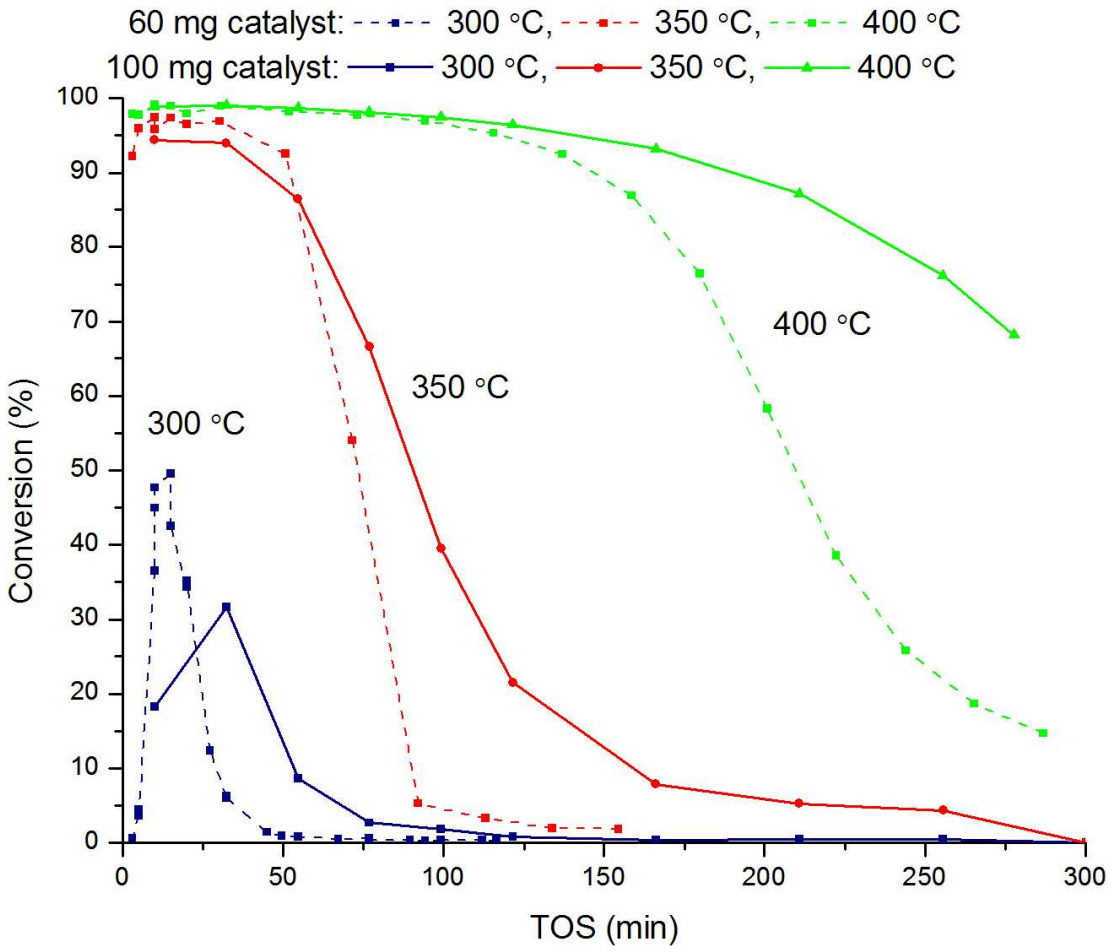

Figure 6.5: Conversion curves for methanol over H-SAPO-34 for different temperatures and different catalyst amounts. WHSV = 6.0 hr^{-1} for all tests. Dashed lines for 60 mg catalyst, and solid lines for 100 mg catalyst.

6.3.1 Study at short times on stream (TOS) - 300°C

In order to study the reactions in more detail it was chosen to perform further experiments at the temperature with slowest conversion, 300°C, since the slower the reaction is, the easier it is to keep track of the individual steps of the reaction.

Figure 6.6 shows conversion of methanol with time on stream for both H-SAPO-34 and H-SSZ-13 under the same conditions. H-SAPO-34 had maximum conversion of 50% after 10-15 minutes, while H-SSZ-13 had a maximum of 100% after 5-10 minutes. An induction period was observed for both catalysts. Also, H-SSZ-13 did not deactivate completely but kept a steady conversion of 3-5 % after

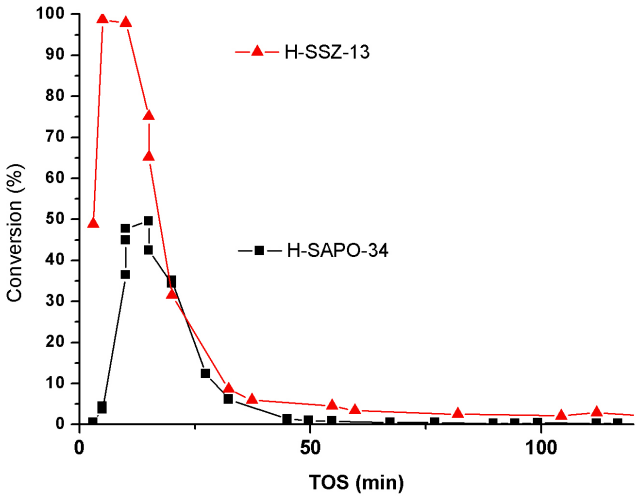

Figure 6.6: Conversion of methanol over H-SAPO-34 and H-SSZ-13 at 300°C measured with gas chromatography

deactivation, while there was no activity on H-SAPO-34 after deactivation.

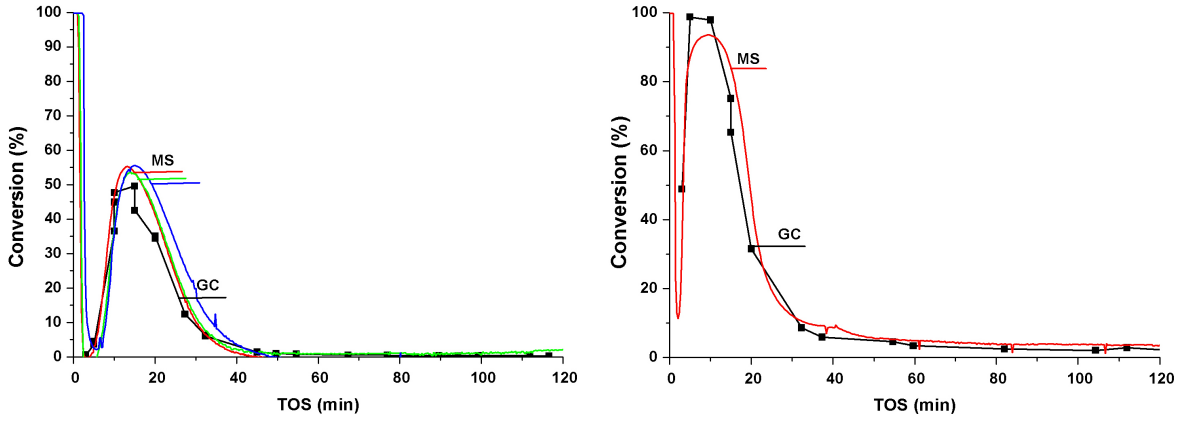

Figure 6.7: Conversion of Methanol over (a) H-SAPO-34 and (b) H-SSZ-13 measured by mass spectrometry and gas chromatography

Figures 6.7a and 6.7b show the conversion of methanol measured by MS and GC superimposed, for H-SAPO-34 and H-SSZ-13 respectively. For H-SAPO-34, MS curves for three reproduction experiments are shown. The reproduction was good although with a slight disagreement in the MS response time after the onset of the methanol flow. Although the agreement between MS and GC analyses was overall quite good, there was a mismatch for both catalysts at maximum conversion.

For H-SAPO-34 mass spectrometry showed higher maximum conversion than GC-analysis, while it was opposite for H-SSZ-13. Mass spectrometry confirmed the induction time observed by GC, and it showed more clearly that the induction period was shorter for H-SSZ-13 than H-SAPO-34 (increase in conversion was faster). At higher temperatures discrepancy between GC and MS curves was only observed after deactivation.

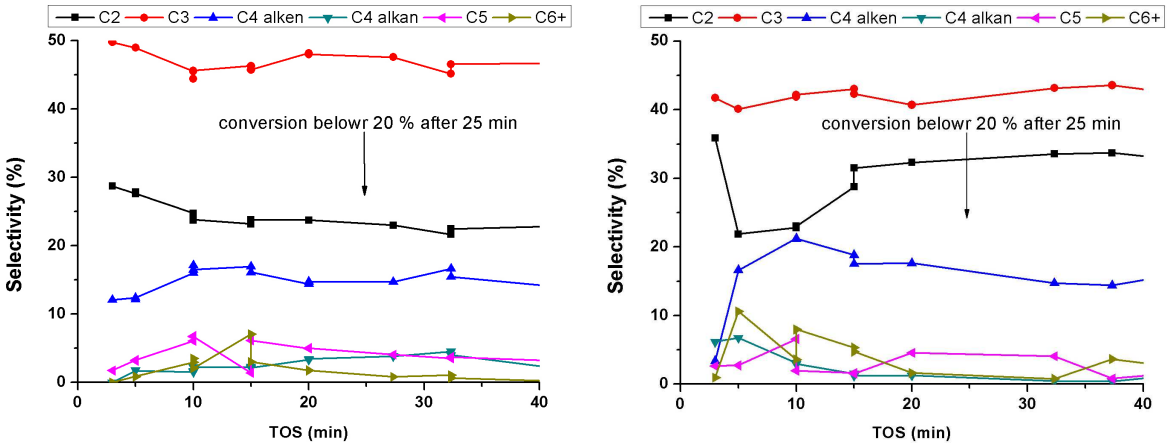

Figure 6.8: Selectivities of products for (a) H-SAPO-34 and (b) H-SSZ-13 at 300°C. Here, and in the following figures, the selectivity is given as percentage of converted carbon atoms.

Figure 6.8 shows the product selectivities for the two catalysts, where the selectivity is given as the percentage of converted carbon atoms. The product stream consisted of mainly C_2-C_4 hydrocarbons, the shorter the hydrocarbon the higher the selectivity. There was a higher selectivity towards C_3 than towards C_2 for both catalysts.

Figure 6.9a compares the selectivity of the C_2 and C_3 species for H-SAPO-34 and H-SSZ-13 and Figure 6.9b compares the C_2/C_3 ratio. The selectivity towards C_2 and C_3 was approximately 70% in total for both catalysts, but that ratio of C_2 to C_3 differed. A higher C_2/C_3 ratio was observed for H-SSZ-13, except for when the catalyst was very fresh (first few points at 100% conversion).

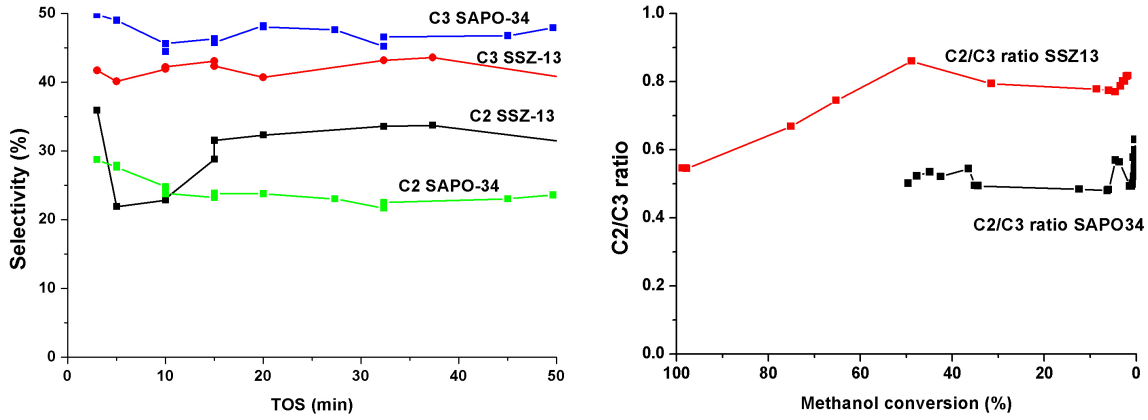

(a) (b)

Figure 6.9: (a)Product selectivities for both catalysts and (b)C_2/C_3 ratio in effluent stream for H-SAPO-34 and H-SSZ-13 at 300°C

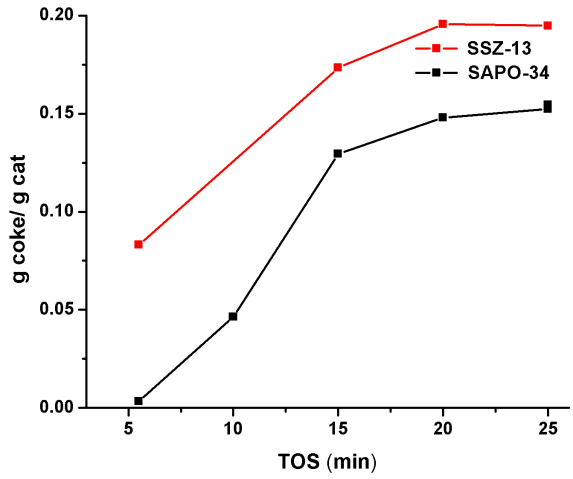

Figure 6.10: Amount of hydrocarbons in quenched material (both external and internal hydrocarbons, 300°C), as measured by TGA

Figure 6.10 gives the total amount of hydrocarbons for both catalysts at 300°C, as measured by TGA. The mass of retained hydrocarbons increased with time, but seemed to level off as conversion decreased. Also, the mass of deposited hydrocarbons was greater for H-SSZ-13 than H-SAPO-34.

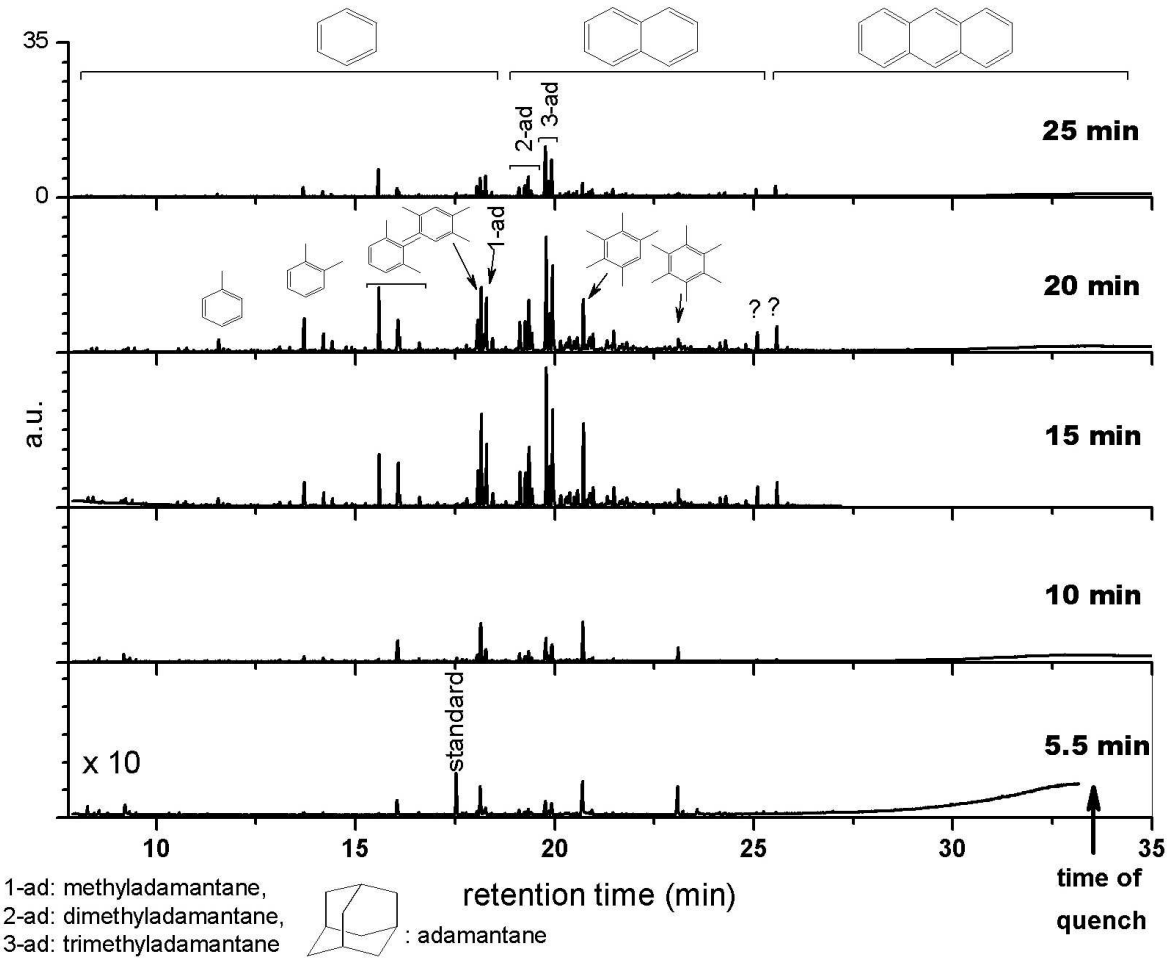

Figure 6.11: Composition of retained hydrocarbons in H-SAPO-34 after 5, 10, 15, 20 and 25 min of methanol feed at 300°C

After 5, 10, 15, 20 and 25 minutes on stream, the zeolite was dissolved in HF and the retained material was subsequently analyzed by GC/MS (Figures 6.11 and 6.12). Qualitatively there seemed to be more retained material in H-SAPO-34 than in H-SSZ-13 and also the build up of the retained soluble hydrocarbons was slower. After 5 and 10 minutes there was more dissolved material from H-SSZ-13, but the amount decreased from 15 to 25 minutes. There was a decrease in the amount of dissolved hydrocarbons after maximum activity has been reached. This decrease was evident from 20 to 25 minutes for H-SAPO-34, and from 15 to 20 minutes for H-SSZ-13. A possible explanation is that the species inside the catalyst grew to become insoluble species, and that deactivation could be, at least partially, due to this. However, the biggest aromatic ring that can be formed inside the cage of the catalyst is pyrene, which is soluble in CH_2Cl_2 (cfr. Fig. 6.3).

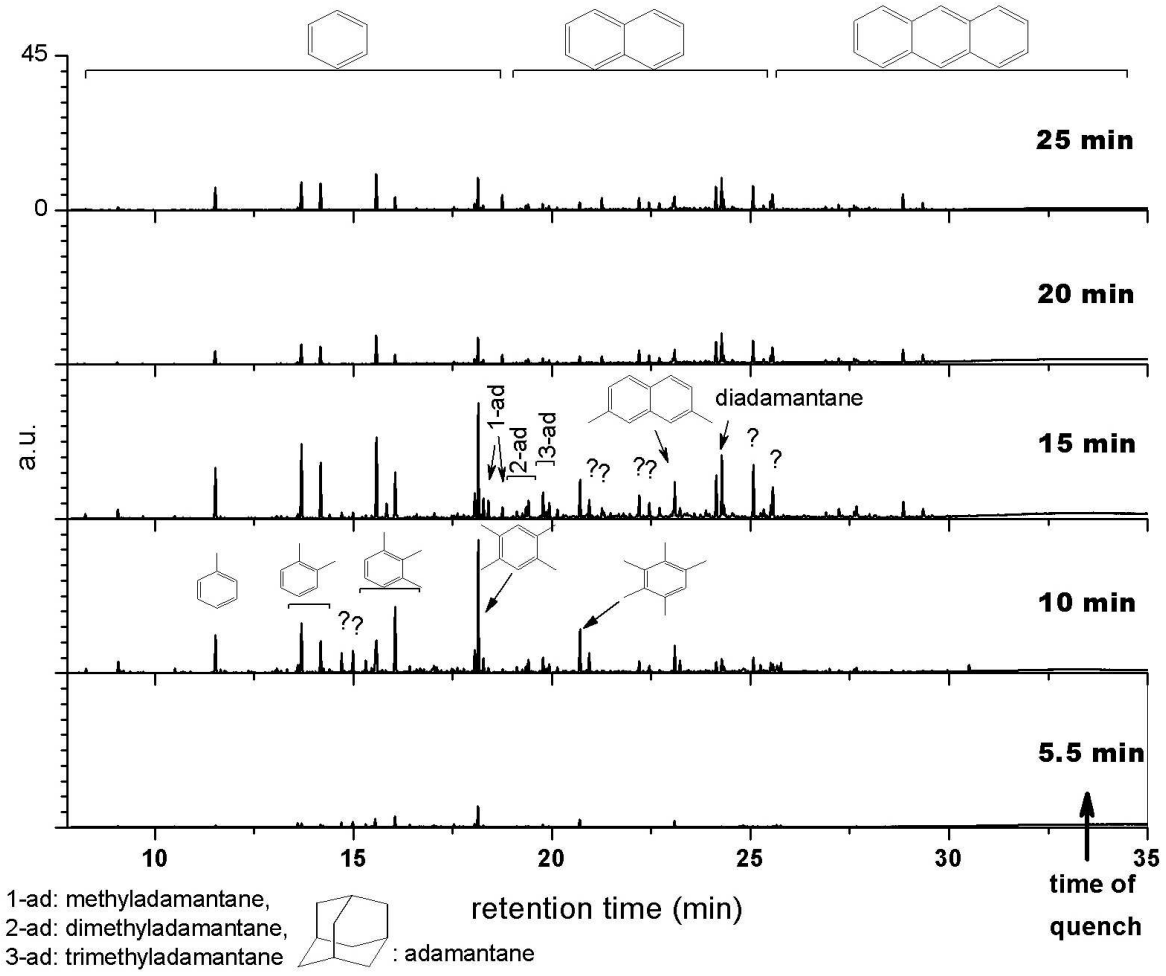

Figure 6.12: Composition of retained hydrocarbons in H-SSZ-13 after 5, 10, 15, 20 and 25 min of methanol feed at 300°C

6.3.2 Study at short TOS - 325°C

Figure 6.13 shows the conversion of methanol over H-SAPO-34 and H-SSZ-13 at 325°C. Again, H-SSZ-13 had a higher methanol conversion capacity than H-SAPO-34. H-SSZ-13 started at full conversion while H-SAPO-34 displayed an induction period and did not reach full conversion. H-SAPO-34 deactivated completely to 0% conversion while H-SSZ-13 leveled off to a constant activity of approximately 8% .

The selectivities for the different products at 325°C are presented in Figures 6.14a and 6.14b. Both catalysts had a higher selectivity towards C_3-hydrocarbons than C_2-hydrocarbons. There was a small

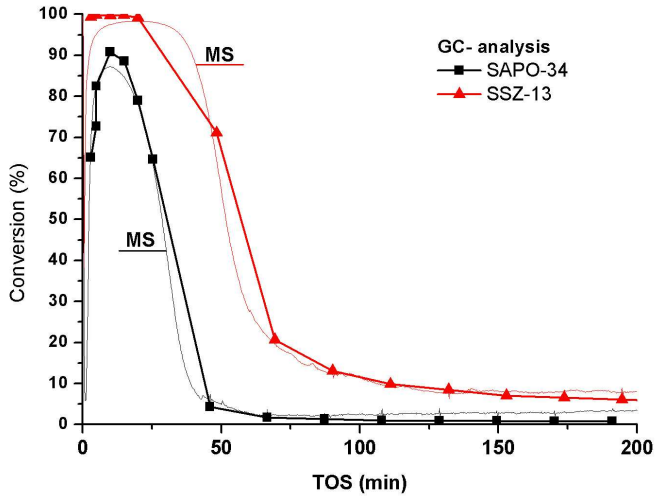

Figure 6.13: Conversion of methanol over H-SAPO-34 and H-SSZ-13 at 325°C measured with gas chromatography

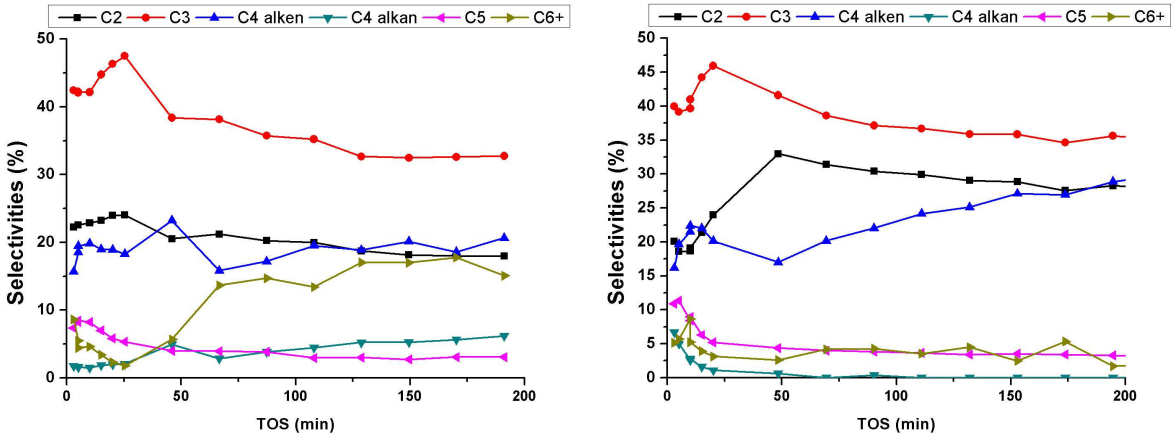

Figure 6.14: Selectivities of products for (a) H-SAPO-34 and (b) H-SSZ-13 at 325°C

increase in selectivity towards both propene/propane and ethene/ethane until conversion started to decrease (approximately 25 minutes on stream for H-SAPO-34 and 50 minutes on stream for H-SSZ-13). As deactivation went to completion the selectivity towards C_4-alkenes increased, but when there was very little conversion the uncertainties became increasingly large and the numbers are therefore not very reliable. However, since the selectivities seemed to be quite stable, they were reported in the graphs also at long times on stream.

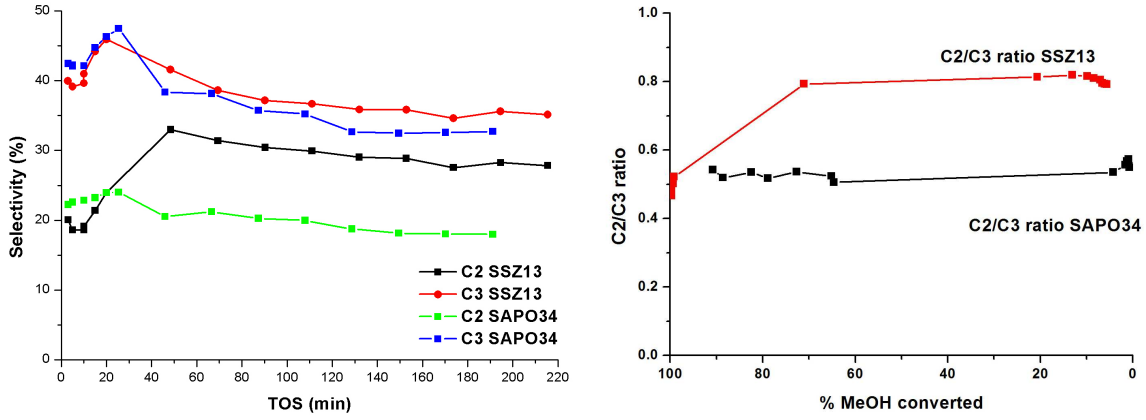

(a) (b)

Figure 6.15: (a)Product selectivities for both catalysts and (b)C_2/C_3 ratio in effluent stream for H-SAPO-34 and H-SSZ-13 at 325°C

In figure 6.15 only selectivities for C_2 and C_3 were considered. Both catalysts had a higher selectivity towards C_3 than C_2 but H-SSZ-13 had a higher selectivity for both products than H-SAPO-34, except during the first 10 minutes on stream when this order was inverted. This means that H-SSZ-13 had a higher total selectivity towards the lighter olefins, compared to H-SAPO-34. Also the C_2 to C_3 ratios for the two catalysts differed, with H-SSZ-13 giving a higher ratio, i.e. a bigger fraction of C_2. The order was inverted during the first 10 minutes, which was approximately the same time as the induction period for H-SAPO-34. Figure 6.15b gives the ratio as a function of methanol converted. H-SAPO-34 never reached full conversion, but the C_2/C_3 ratio was similar for both catalysts at maximum conversion. The ratio stayed stable for H-SAPO-34, while it increased with deactivation for H-SSZ-13. A possible explanation for the increase of C_2 with deactivation can be that as deactivation proceeded the catalyst pores became more and more clogged and so it was easier for C_2 than for C_3 to diffuse out. The C_2/C_3 ratio changed with deactivation only for H-SSZ-13 indicating that the hydrocarbons formed in the two catalysts had different effects on the selectivities.

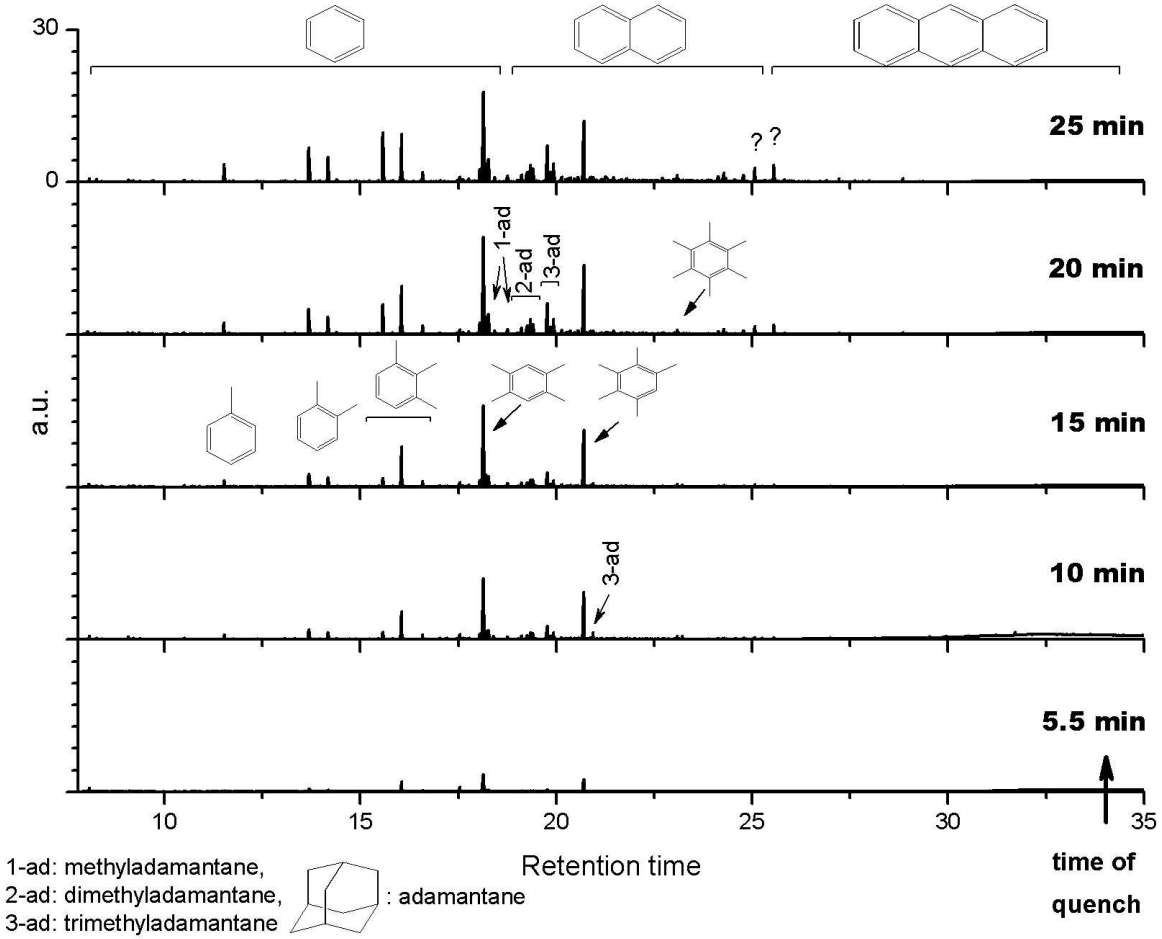

Figure 6.16: Composition of retained hydrocarbons in H-SAPO-4 after 5, 10, 15, 20 and 25 min of methanol feed at 325°C

Figures 6.16 and 6.17 show the chromatograms of the retained material soluble in HF. Also at 325°C there was an increase in retained material with time. Comparing the intensity of the peaks in the two figures show that there was more dissolved material in H-SSZ-13 than in H-SAPO-34. There were mostly methylated benzenes in H-SAPO-34, but more two-rings in H-SSZ-13 giving a shift towards the heavier two-ring fraction in H-SSZ-13. At 325°C there were no three-rings present during the first 25 minutes on stream. H-SSZ-13 also contained some non-aromatic two-rings and a few dimethyladamantane peaks were detected. In H-SAPO-34 adamantanes with one, two and three methyl groups were found. As at 300°C there was a maximum for the amount of soluble hydrocarbons. In H-SSZ-13 there was less soluble material after 25 minutes than after 20 minutes. The same was not observed within the first 25 minutes in H-SAPO-34. By comparing the y-axis in Figure 6.3 on page 58 (5 hr test) and in Figures 6.16 and 6.17 it is evident that there was a decrease of soluble

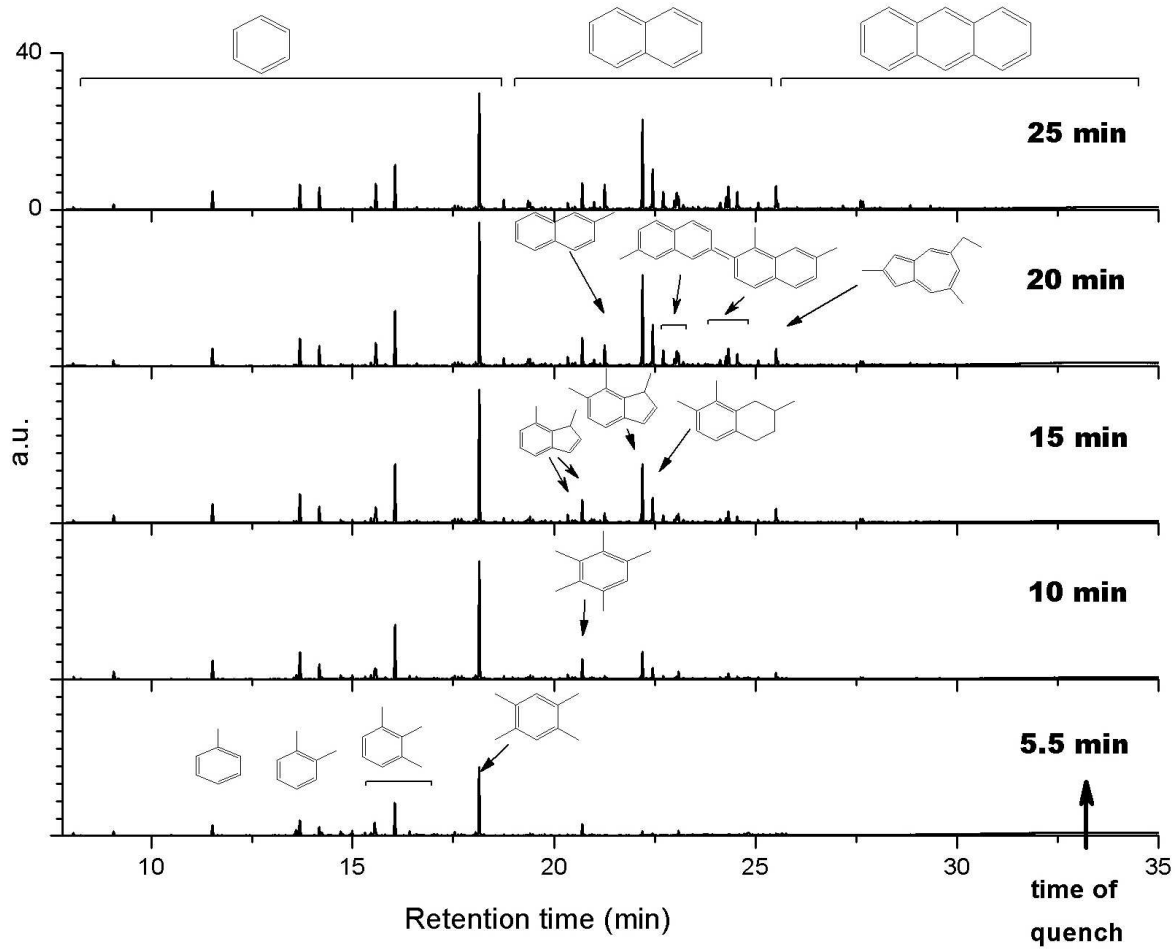

Figure 6.17: Composition of retained hydrocarbons in H-SSZ-13 after 5, 10, 15, 20 and 25 min of methanol feed at 325°C

hydrocarbons after long times on stream for both catalysts.

At 325°C the total amount of hydrocarbons, measured by TGA, increased up to 25 min on stream for both catalysts, as seen in figure 6.18. There were more hydrocarbons on H-SSZ-13, but the amount of coke seemed to level of. A decrease in the slope of the coke versus time curve was observed also for H-SAPO-34. H-SSZ-13 displayed full conversion for more than 25 minutes before deactivation started.

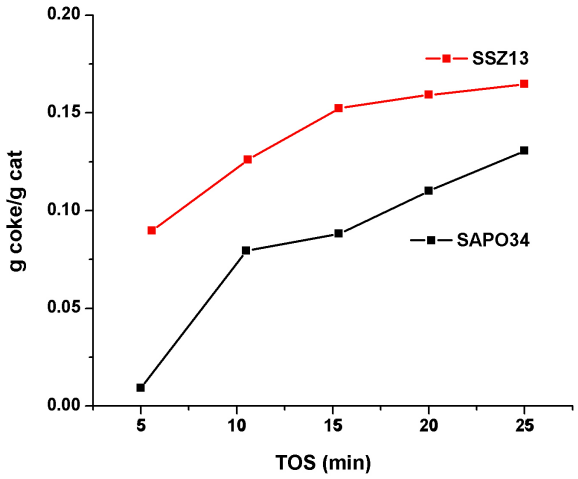

Figure 6.18: Amount of hydrocarbons in quenched material (both external and internal hydrocarbons) at 325°C, as measured by TGA.

6.3.3 Study at short TOS - 350°C

The conversion of methanol for both catalysts at 350°C is compared in Figure 6.19. H-SSZ-13 had a higher capacity for converting methanol than H-SAPO-34 under these conditions, as it had at the lower temperatures. After 260 minutes H-SSZ-13 had an activity of 20% and was still not completely deactivated. H-SAPO-34 was nearly completely deactivated after 85 minutes. It was still possible to see an induction period for H-SAPO-34, but this was now much shorter than at lower temperatures. Also, H-SAPO-34 reached nearly full conversion, 99%, but it started deactivating sooner than H-SSZ-13 and also deactivated faster.

The selectivities of H-SAPO-34 and H-SSZ-13 at 325 and 350°C were similar (Figure 6.20). Both catalysts had a higher selectivity towards C_3 than C_2 hydrocarbons, but the difference was more pronounced in H-SAPO-34. As long as there was significant activity (i.e. the catalyst is fresh) the selectivities were quite stable for both catalysts. For H-SAPO-34 the changes started after 80 minutes on stream, when the conversion was only a few percent. In the beginning, when there was full conversion there was a slight increase in C_2 and C_3. In H-SSZ-13 this effect was stronger, especially for the C_2 compounds. Initial selectivities for the two catalysts were very similar and the total selectivity for C_2 and C_3 was around 75% for both, but the ratios differed.

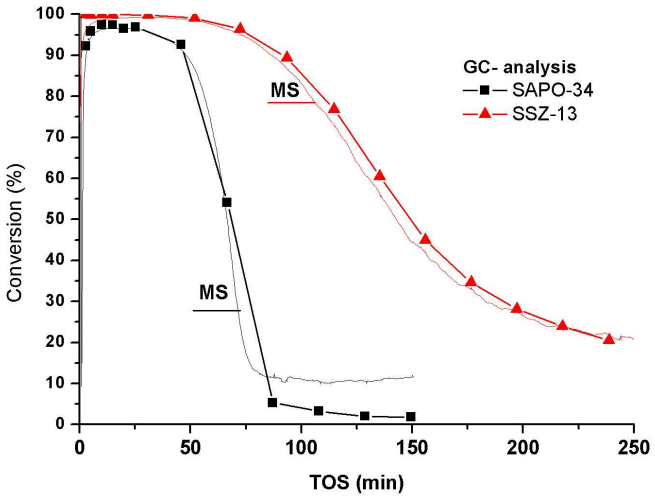

Figure 6.19: Conversion of methanol over H-SAPO-34 and H-SSZ-13 at 350°C measured with gas chromatography

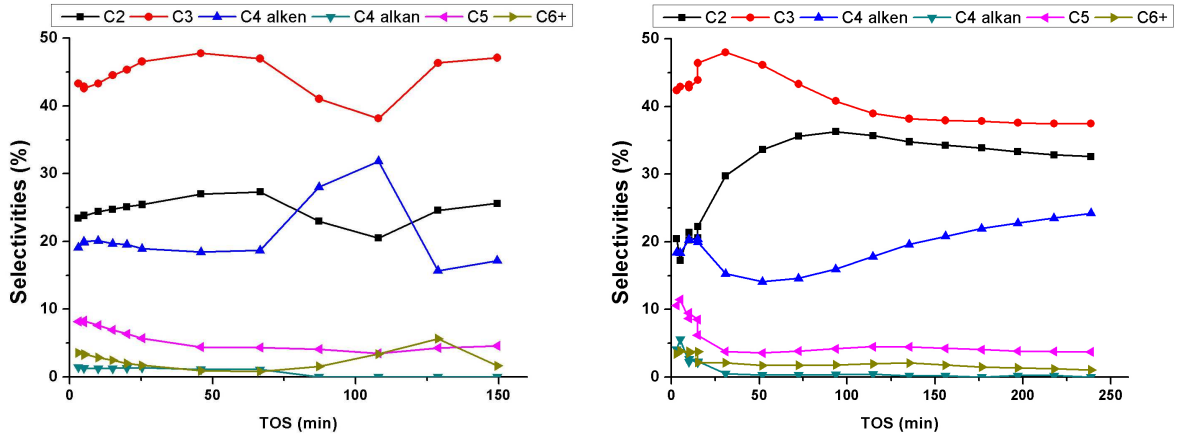

Figure 6.20: Selectivities of products for (a) H-SAPO-34 and (b) H-SSZ-13 at 350°C

Figures 6.21a and 6.21b show more clearly the differences in C_2 and C_3 selectivities for the two catalysts. The selectivities for C_3 were almost identical until H-SAPO-34 completely deactivated, but there was more difference for C_2. In the beginning there was less C_2 produced from H-SSZ-13 than H-SAPO-34 but the C_2 selectivity increased significantly when deactivation started. This means that the C_2/C_3 ratio was lower for H-SSZ-13 than H-SAPO-34 when the catalyst was fresh, but that this changed quickly. C_2/C_3 ratios were quite stable after the first "build-up" phase. The ratio was less

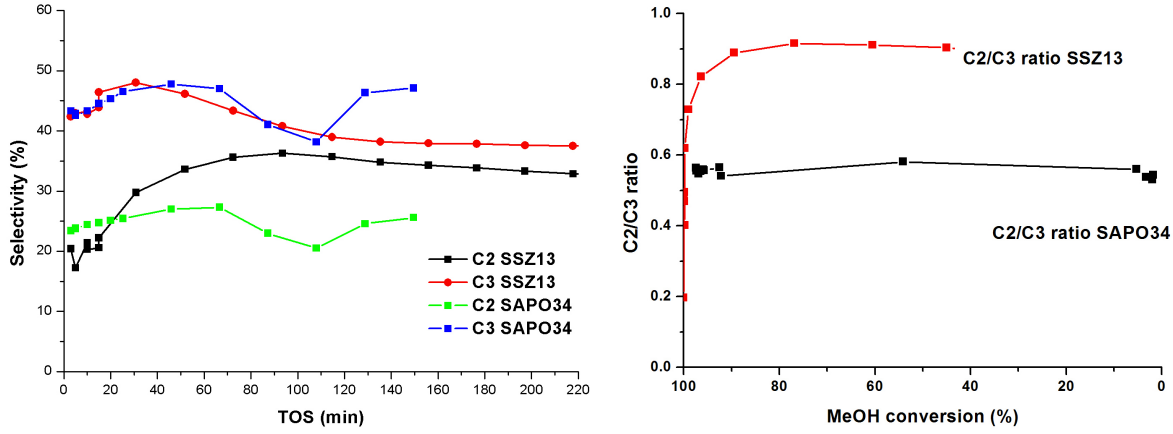

(a) (b)

Figure 6.21: (a)Product selectivities for both catalysts and (b) C_2/C_3 ratio in effluent stream for H-SAPO-34 and H-SSZ-13 at 350°C

than one which means more of the methanol went into C_3 than C_2 hydrocarbons.

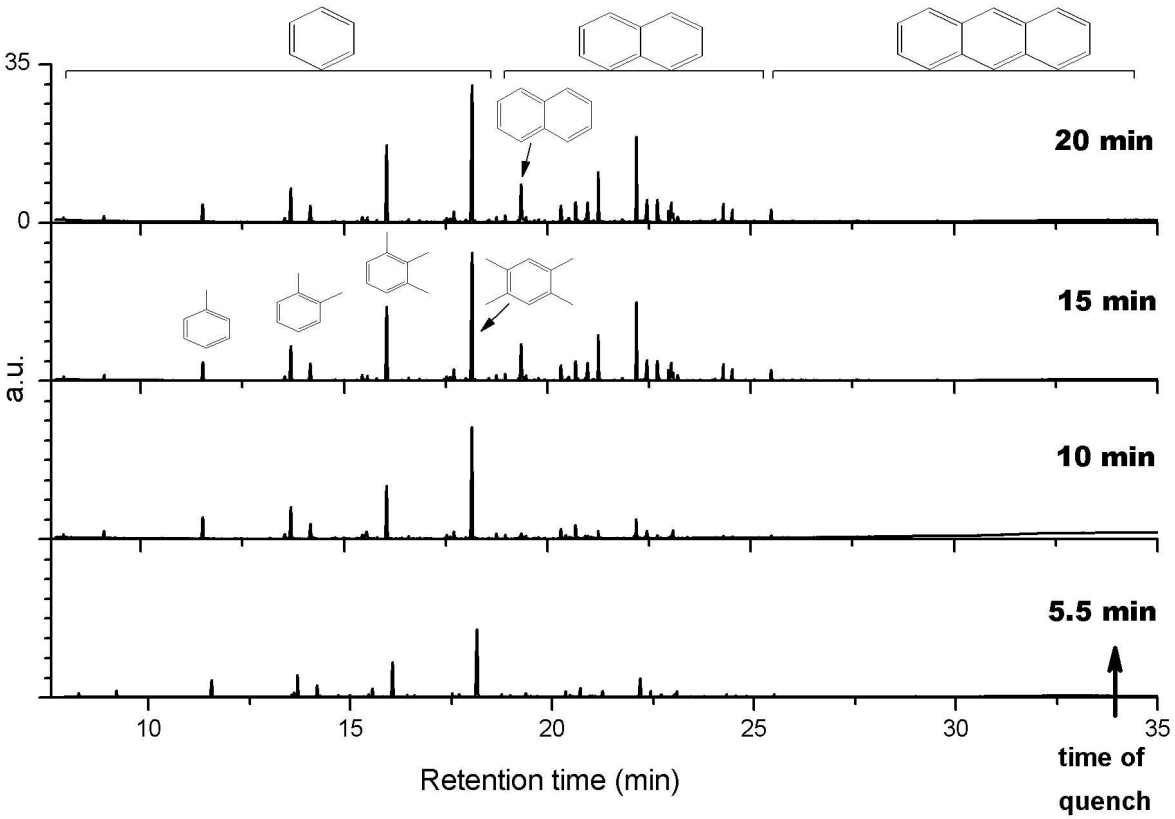

Figure 6.22: Composition of retained hydrocarbons in H-SSZ-13 after 5, 10, 15, 20 and 25 minutes of methanol feed at 350°C. The peaks are identified in more detail in Fig 6.24 and 6.25.

The chromatograms of the retained material (Fig. 6.22 and 6.23) were more similar for the two catalysts at 350°C than at lower temperatures. There was again an increase in soluble, retained hydrocarbons with time, and for H-SAPO-34 there was a decrease between 20 and 25 minutes. There was not enough catalyst to perform the test at 25 minutes for H-SSZ-13. The main peak for both catalysts was tetramethylbenzene. Two-ring structures were more prominent in H-SSZ-13, they were not present in the dissolved H-SAPO-34.

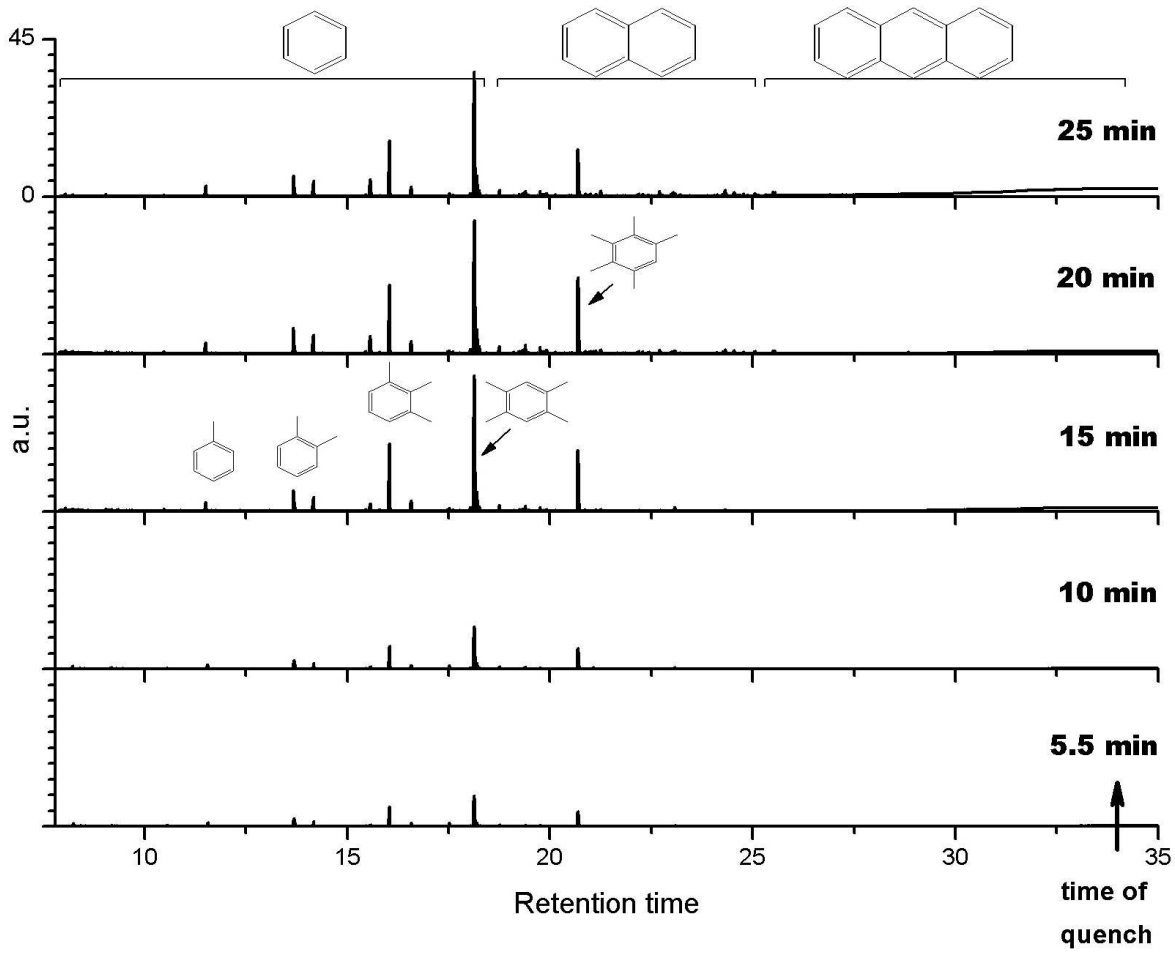

Figure 6.23: Composition of retained hydrocarbons in H-SAPO-4 after 5, 10, 15, 20 and 25 minutes of methanol feed at 350°C.

While the effluent only consisted of a small range of compounds, there was a wide specter of retained hydrocarbons. Figures 6.24 and 6.25 show in more detail the differences in the retained material for the two catalysts after 5 and 15 min, respectively.

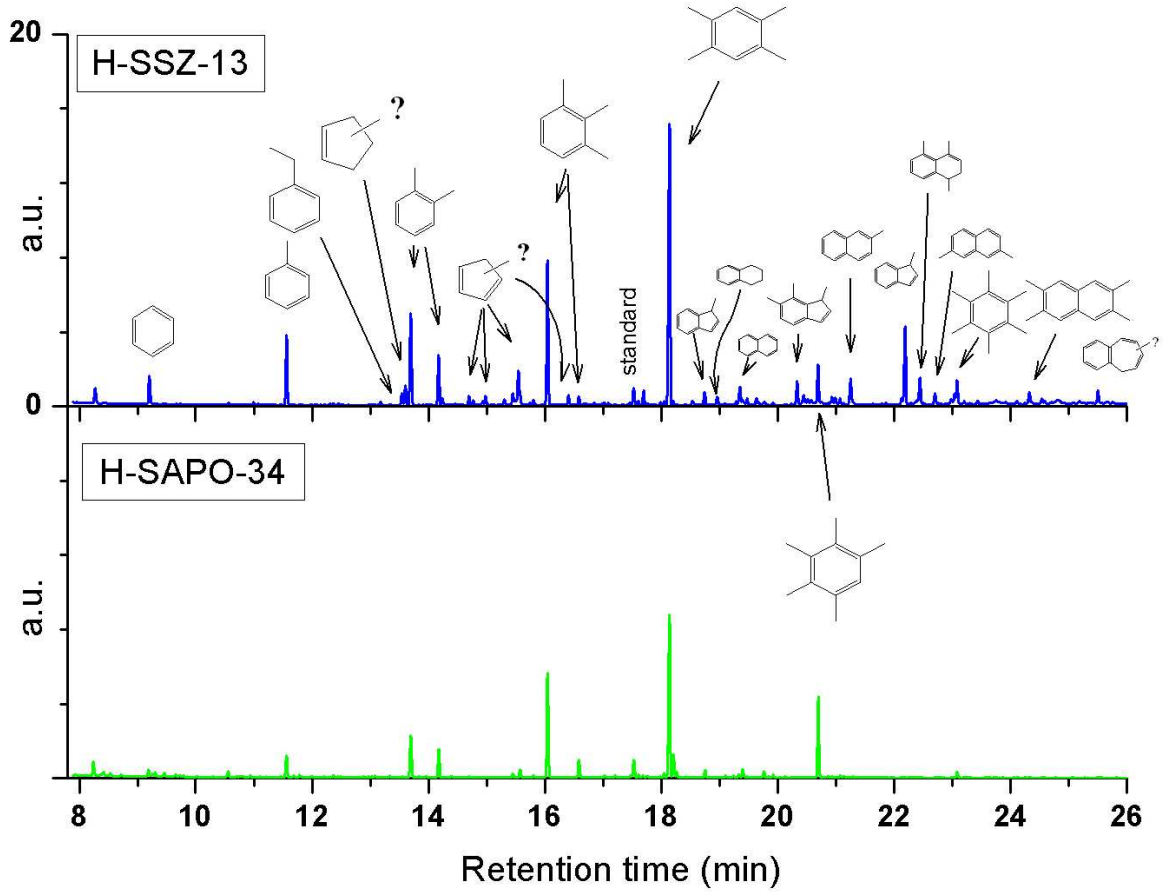

Figure 6.24: Retained hydrocarbons after 5 minutes of methanol feed in H-SSZ-13 (top) and H-SAPO-34 (bottom). There was in total more retained hydrocarbons in H-SSZ-13. H-SSZ-13 contained a wider variety of compounds than H-SAPO-34 which contained almost exclusively methylated benzenes. Methyl groups with question marks indicate that the number of methyl-groups was not well established. A line with a question mark on a ring indicates that the number of methyl groups was not well determined.

After 5 minutes on stream the amount of hydrocarbons was bigger in H-SSZ-13. Also, there were almost only polymethylated benzenes in H-SAPO-34 while several other ring-compounds were found in H-SSZ-13. The most abundant two-ring was methylindene which is only partially aromatic (aromatic benzene fused with a cyclopentene ring). As in the case with the benzenes, there were more methylated than non-methylated two-rings. There were also other one-rings than benzene in H-SSZ-13, mostly cyclopentenes and cyclopentadienes. The latter are interesting because Anderson et al. suggested pentadienes to be precursors for the formation of adamantanes in H-SAPO-34 [37].

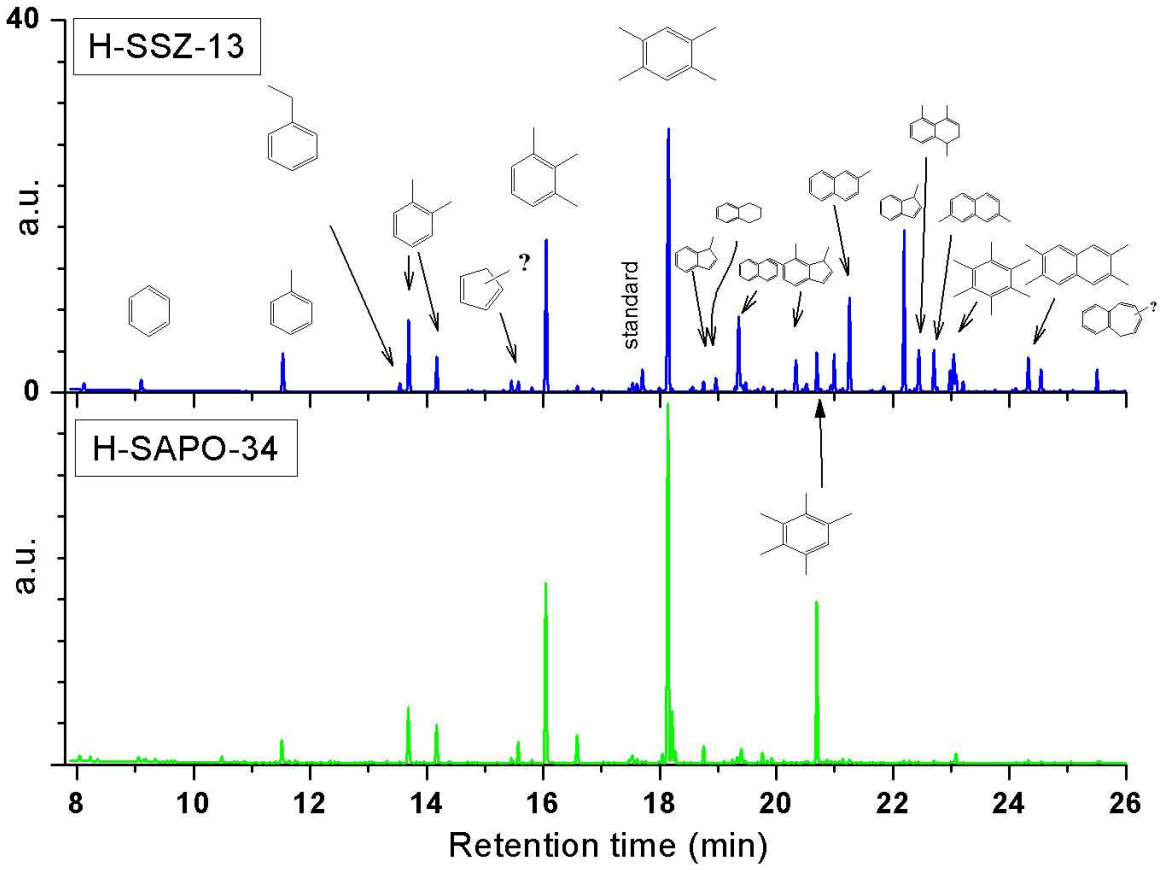

Figure 6.25: Retained hydrocarbons after 15 minutes of methanol feed in H-SSZ-13 (top) and H-SAPO-34 (bottom). The difference between the two catalysts was smaller than after 5 minutes on stream.

After 15 minutes on stream there were more soluble retained hydrocarbons than after 5 minutes (note that the y-axis on Figures 6.24 and 6.25 differ). The difference between the two catalysts was no longer that pronounced, but still there were almost only polymethylated benzenes in H-SAPO-34, while H-SSZ-13 formed several other one- and two-rings. At 350°C no adamantane derivatives were detected in the dissolved material.

As at the lower temperatures the total amount of coke increased with time for both catalysts (Fig. 6.26), and again there was more coke deposited on H-SSZ-13 than on H-SAPO-34.

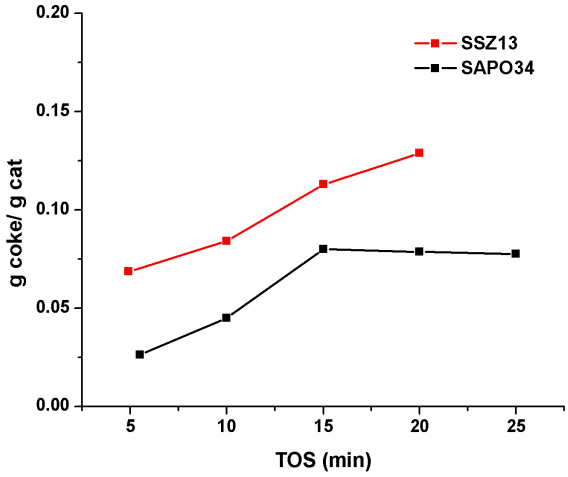

Figure 6.26: Amount of hydrocarbons in quenched material (both external and internal hydrocarbons), at 350°C, as measured by TGA.

6.3.4 Study at short TOS - 375°C

At 375°C the order of stability with time for H-SAPO-34 and H-SSZ-13 changed as opposed to lower temperatures, now H-SAPO-34 started to deactivate later than H-SSZ-13 (Fig. 6.27). Still, H-SSZ-13 deactivated slower. This means that when H-SSZ-13 started to deactivate H-SAPO-34 had a higher activity, but that this order changed after a while. After 300 minutes H-SSZ-13 still had an activity of 20% and H-SAPO-34 converted only 10% methanol. Figure 6.41 on page 88 shows that at 375°C the total methanol converted from start until the catalyst had deactivated to 20% conversion was very similar for the H-SAPO-34 and H-SSZ-13, 16.2 and 16.7 g methanol/g catalyst, respectively. Since the test was stopped after 300 minutes it is not known how this activity changed further. Thus, H-SSZ-13 had a higher conversion capacity than H-SAPO-34 at 375°C, but H-SAPO-34 displayed full conversion for a longer time.

The selectivities at 375°C are shown in figure 6.28. Both catalysts had a higher selectivity for C_3 than C_2 hydrocarbons initially, but when the activity had decreased to 80% this order changed for H-SSZ-13. The selectivities were quite stable in H-SAPO-34, and changes in C_2 corresponded to changes in C_4. Also, the C_2/C_3 ratio was always less than one for H-SAPO-34. In H-SSZ-13, the selectivity towards C_2 was initially much lower than towards C_3. During the period where there was

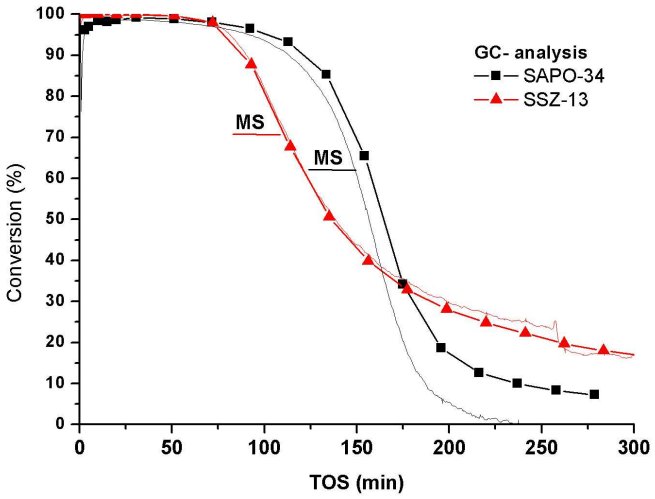

Figure 6.27: Conversion of methanol over H-SAPO-34 and H-SSZ-13 at 375°C measured with gas chromatography

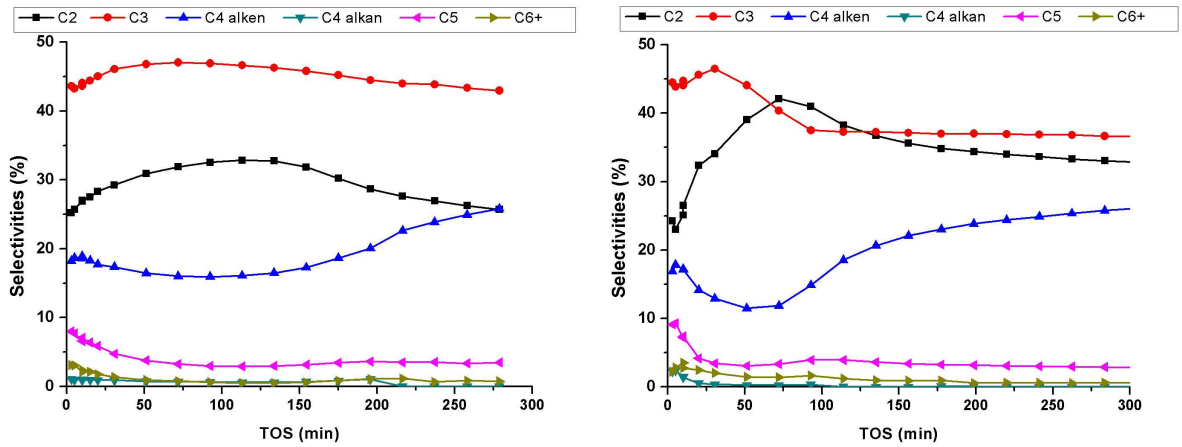

Figure 6.28: Selectivities of products for (a) H-SAPO-34 and (b) H-SSZ-13 at 375°C

full conversion C_3 decreased a little and C_2 increased much until their selectivities were similar.

The selectivity gives the amount of product relative to the converted methanol, while the yield gives the amount of product relative to the feed. Figures 6.29a and 6.29b show the yields for the reaction at 375°C. The changes in the yield of C_4-hydrocarbons were not as closely connected to the change in C_2 hydrocarbons as the selectivity curves suggested. However there was a small increase in C_4 in H-SSZ-13 when the C_2 and C_3 yields started do decrease. Especially for H-SSZ-13 the changes in C_4

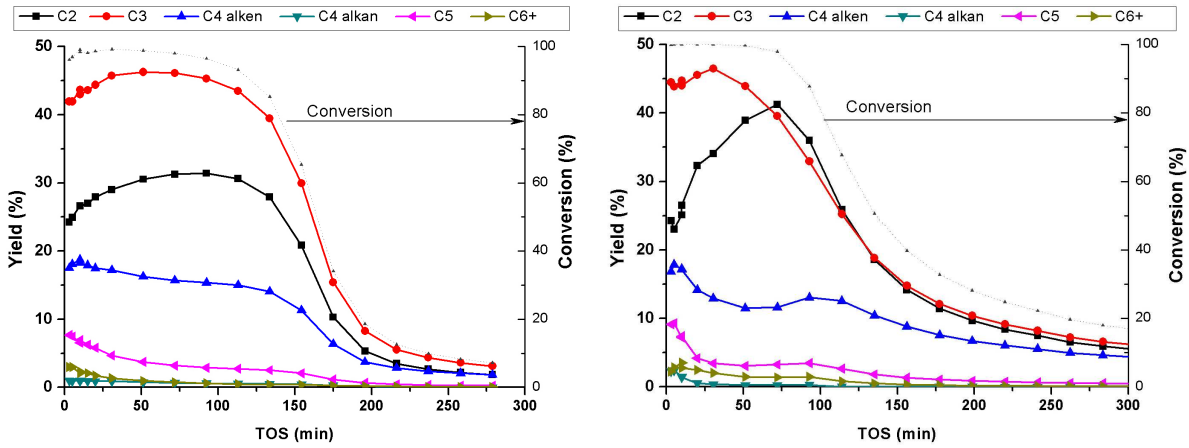

Figure 6.29: Yields for (a) H-SAPO-34 and (b) H-SSZ-13 at 375°C

were not as pronounced as those of C_2 and C_3. For both catalysts there was an increase in C_2 and C_3 yield at the beginning of the reaction, and this increase was stronger for C_2. That C_2 increased relative to C_3 with deactivation may have been due to C_2 molecules being smaller and therefore diffusing more easily through the partially blocked structure. That the bigger C_4 molecules increased relative to C_2 and C_3 must have a different explanation. One possibility is that C_4 was formed by an alternative route on the outer part of the crystal, and thus deactivation did not have such a strong effect on this reaction.

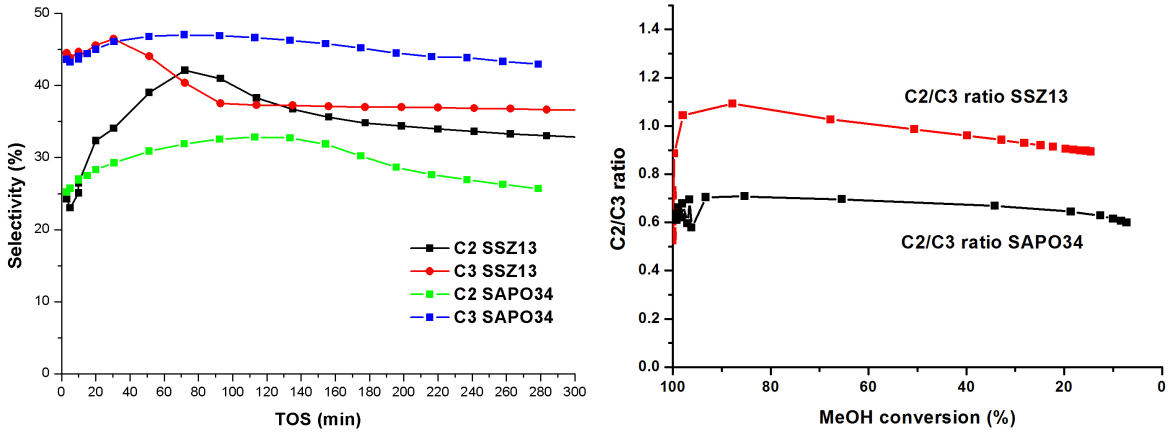

(a) (b)

Figure 6.30: (a)Product selectivities for both catalysts and (b)C_2/C_3 ratio in effluent stream for H-SAPO-34 and H-SSZ-13 at 375°C

Figure 6.30a shows how the selectivities for C_2 and C_3 were much more similar in H-SSZ-13 than in H-SAPO-34 after the first hour on stream. For H-SSZ-13 the selectivity towards C_2 was higher than towards C_3 when the catalyst was no longer very fresh (Fig. 6.30b). Again, a build up towards a more stable ratio was displayed during the period where there was full conversion. The ratio increased for both catalysts compared to lower temperatures, which means that there was relatively more C_2 produced compared to C_3 at this temperature.

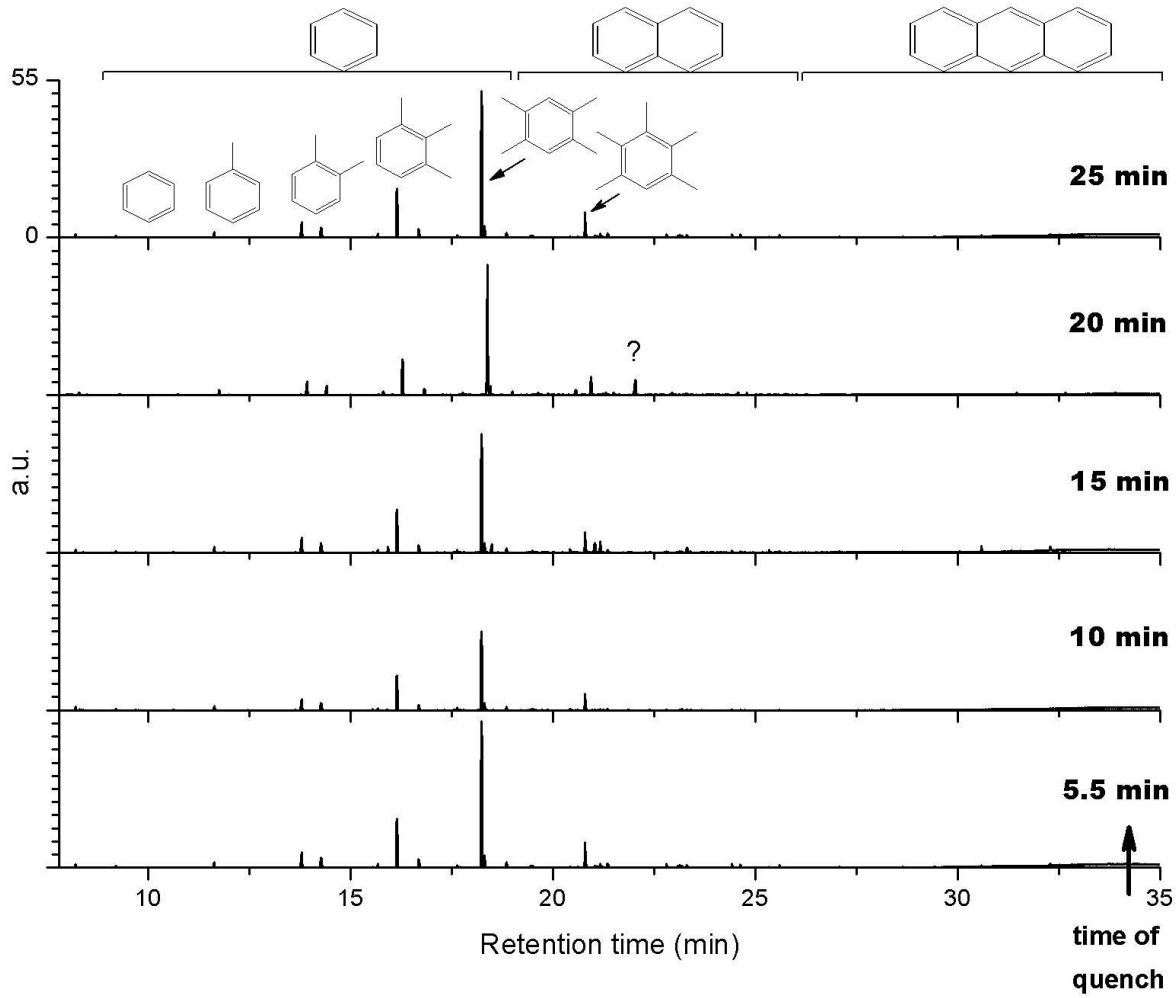

Figure 6.31: Composition of retained hydrocarbons in H-SAPO-4 after 5, 10, 15, 20 and 25 min of methanol feed at 375°C

At 375°C, the highest peaks of the retained material were higher than at the lower temperatures (Figures 6.31 and 6.32) Also, there was much more retained material soluble in CH_2Cl_2 in H-SSZ-13 than H-SAPO-34, and at this temperature there was a clearer difference in the size of the aromatic compounds retained. For both catalysts, the main peak was tetramethylbenzene, but in H-SSZ-13 there was a big fraction of naphtalene and methyl naphtalenes. In H-SAPO-34 there were no two ring aromatics present, as the only compound eluted after tetramethylbenzene was pentamethylbenzene. There were still no bigger aromatics than two-rings present after 25 minutes in H-SSZ-13. Most of the retained compounds were aromatic. At 375°C the total amount of hydrocarbons was higher in H-SSZ-13 than in H-SAPO-34 (Figure 6.33).

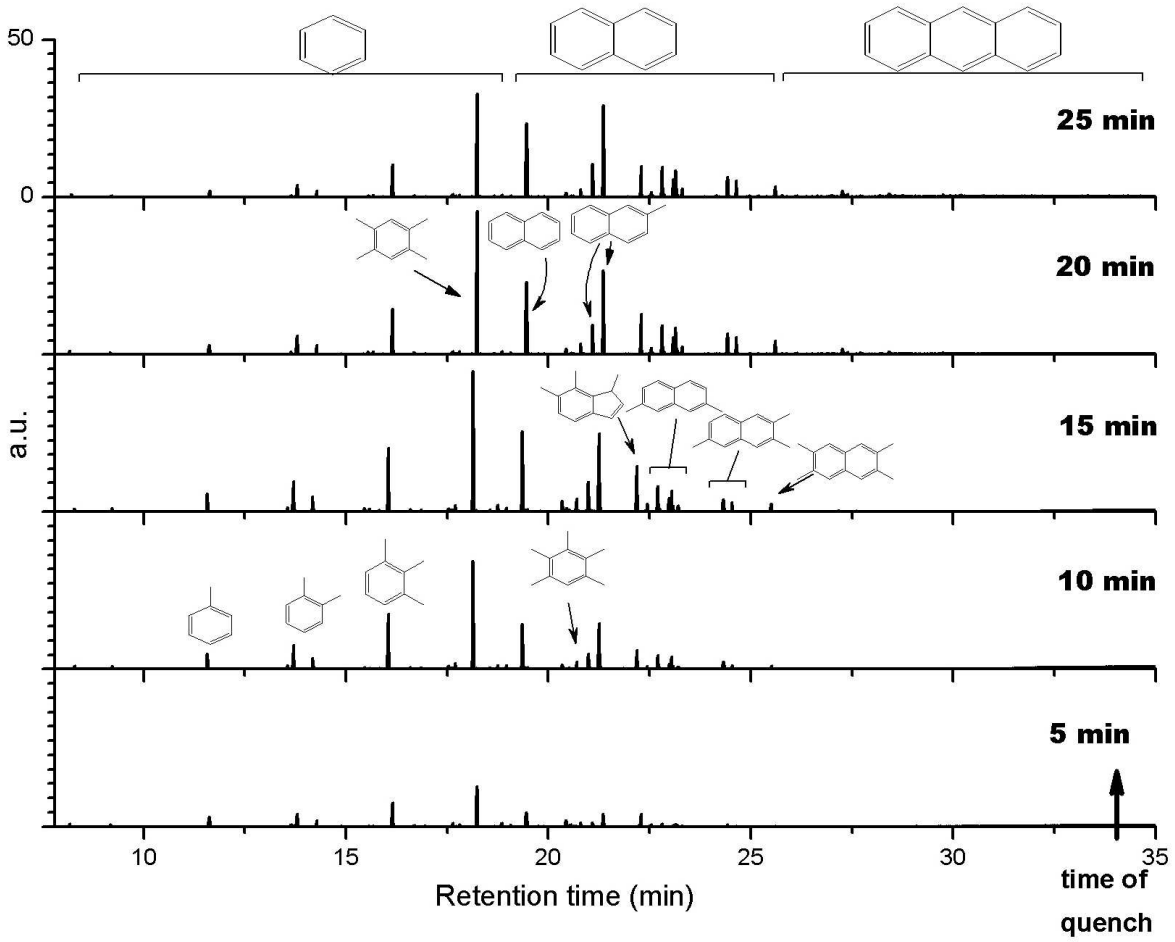

Figure 6.32: Composition of retained hydrocarbons in H-SSZ-13 after 5, 10, 15, 20 and 25 min of methanol feed at 375°C

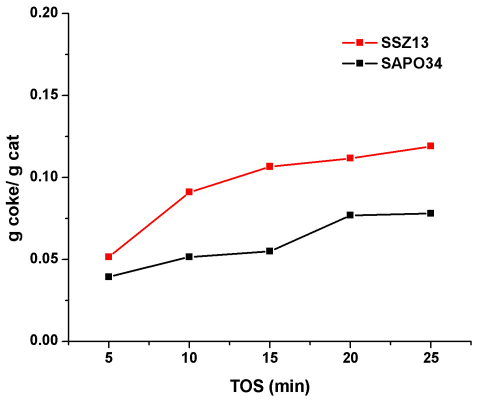

Figure 6.33: Amount of hydrocarbons in quenched material (both external and internal hydrocarbons), at 375°C, as measured by TGA

6.3.5 Study at short TOS - 400°C

At 400°C both catalysts initially displayed full conversion of methanol, and no induction period was observed (Figure 6.34). H-SSZ-13 started deactivating after 70 minutes, which was half as good as H-SAPO-34 (deactivation started at about 140 minutes).

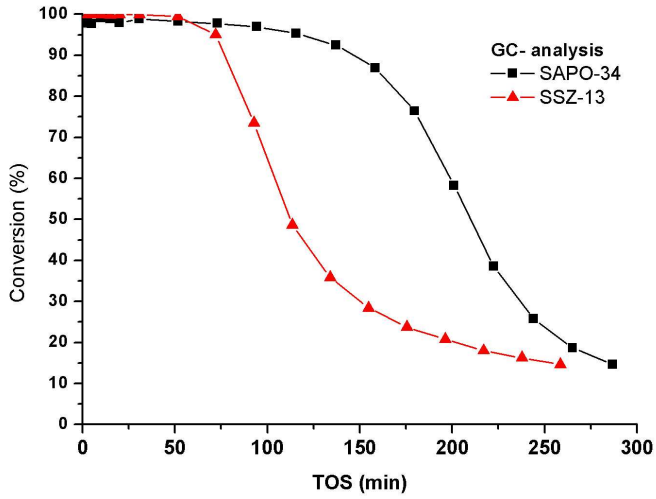

Figure 6.34: Conversion of methanol over H-SAPO-34 and H-SSZ-13 at 400°C measured with gas chromatography

H-SAPO-34 still displayed a higher selectivity towards C_3 than C_2, but H-SSZ-13 gave more C_2 than C_3 carbons once the catalyst had started deactivating.

The hydrocarbon selectivities shown in figure 6.35 for H-SAPO-34 manifested a very stable selectivity towards C_3. The increase and then decrease in C_2 was mainly compensated for by C_4 alkenes, but also the higher hydrocarbons. The same was true for H-SSZ-13, but here it seemed that the increase in C_2 at the beginning was more correlated to the C_3 selectivity. Both catalysts had an increase in C_2 selectivity during the period of full conversion. When the conversion started declining, also the C_2 selectivity went down. This effect was much more pronounced in H-SSZ-13 than H-SAPO-34. For both catalysts the main selectivity to C_2 and C_3 was approximately 70%, but the distribution among them differed. Figure 6.36 shows more clearly that the selectivities were more stable in H-SAPO-34 than in H-SSZ-13, also if the period with full conversion is considered. Except for when the catalyst was very fresh, more C_2 than C_3 was formed in H-SSZ-13, while there was always more C_3 than C_2

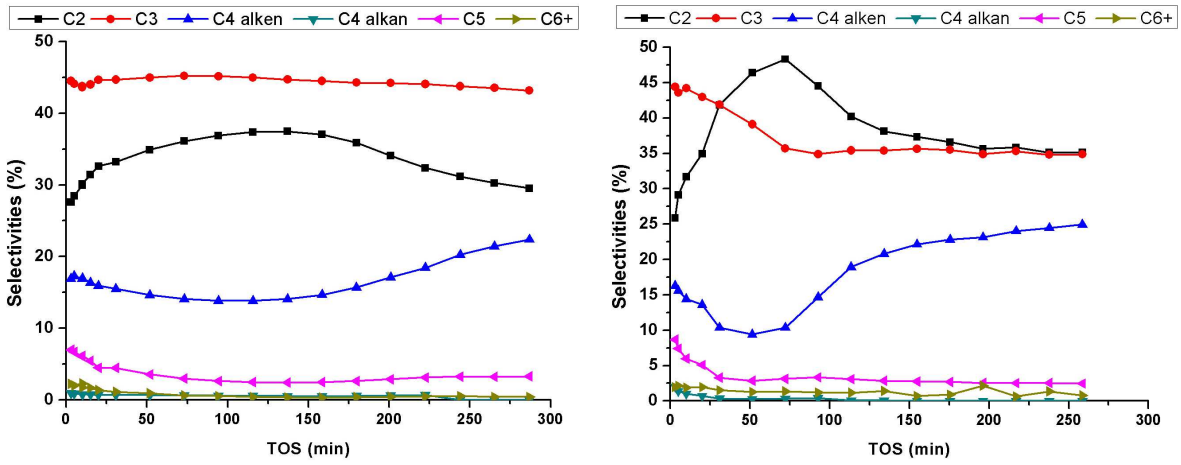

Figure 6.35: Selectivities of products for (a) H-SAPO-34 and (b) H-SSZ-13 at 400°C

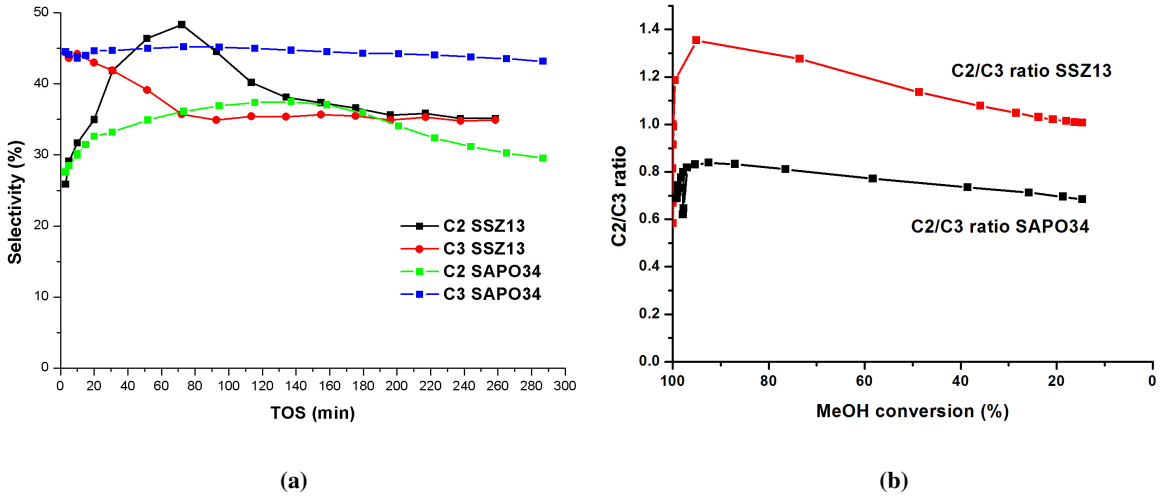

Figure 6.36: (a)Product selectivities for both catalysts and (b)C_2/C_3 ratio in effluent stream for H-SAPO-34 and H-SSZ-13 at 400°C

in H-SAPO-34.

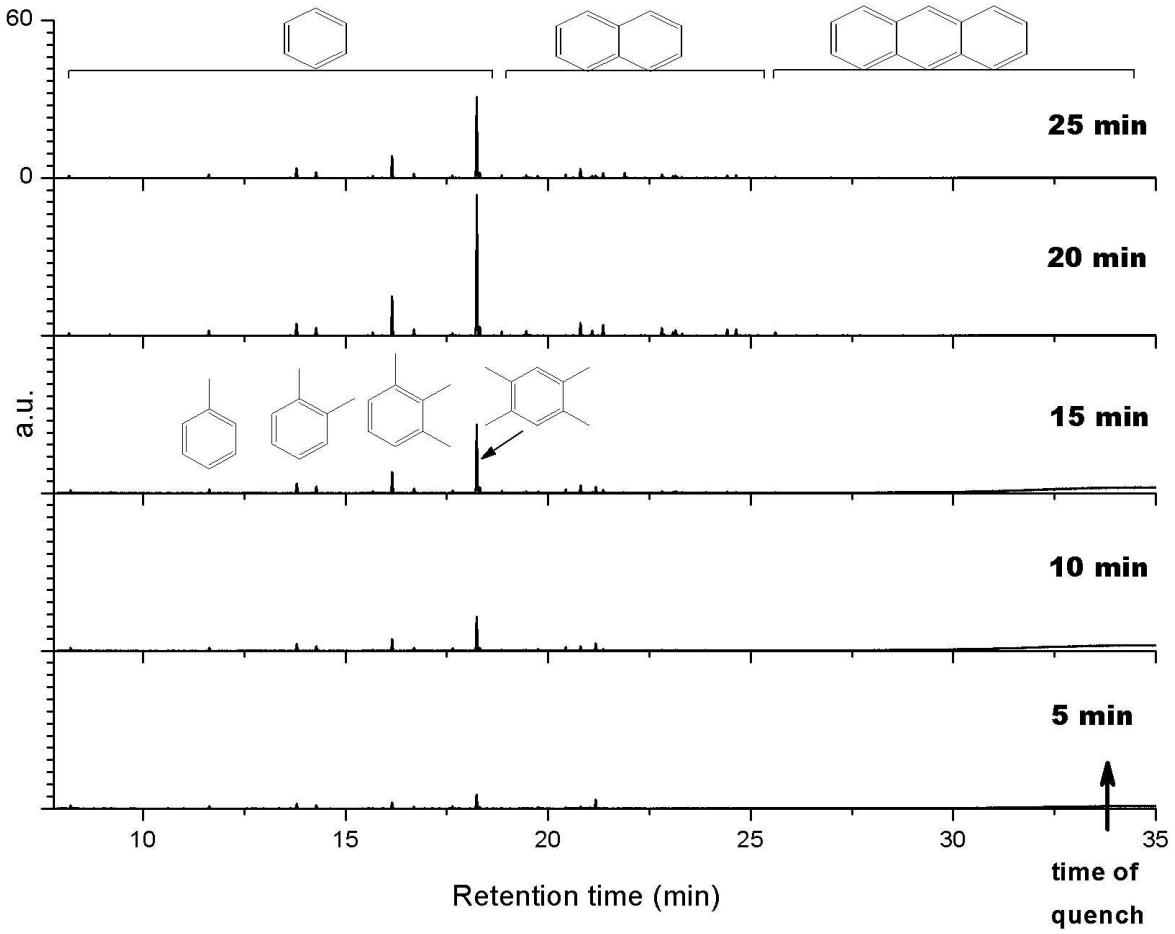

Figure 6.37: Composition of retained hydrocarbons in H-SAPO-4 after 5, 10, 15, 20 and 25 min of methanol feed at 400°C

Figures 6.37 and 6.38 show the retained hydrocarbons at 400°for H-SAPO-34 and H-SSZ-13, respectively. There was less soluble material in H-SAPO-34, and the main compound in this less acidic catalyst was tetramethylbenzene. Comparing the height of the different peaks at the different temperatures showed that the relative amount of tetramethylbenzene was higher at 400°C; The other methylated benzenes were present in very small amounts. There was an increase in the tetramethylbenzene peak in the beginning, and then a decrease from 20 to 25 minutes on stream. The main compounds retained in H-SSZ-13 at 400°C were naphtalene and methylnaphtalene, except after 5 minutes on stream when tetramethylbenzene was most abundant. The amount of the two naphtalenes was approximately the same and the third highest peak was attributed to tetramethylbenzene. There was an increase in retained soluble material from 5 to 15 minutes on stream, and then there was little

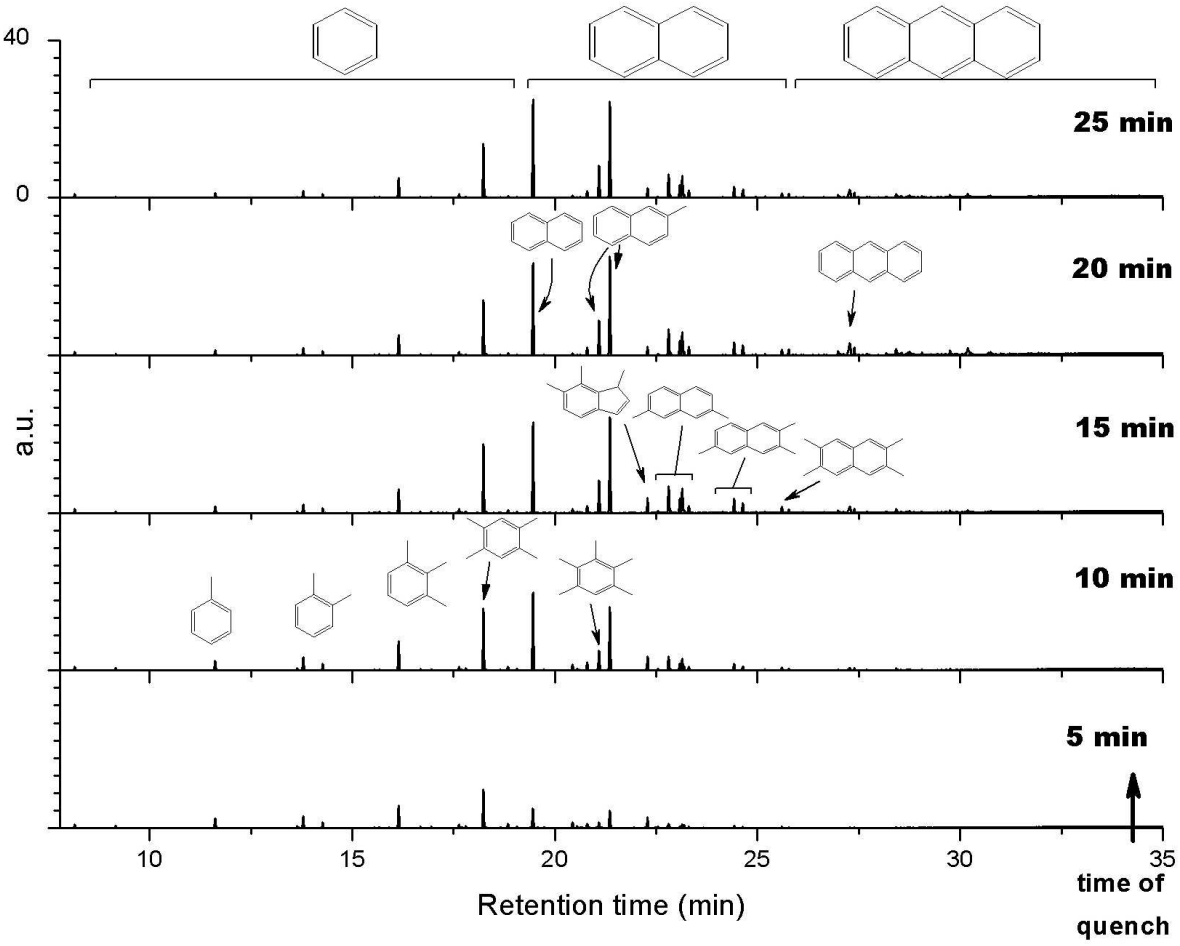

Figure 6.38: Composition of retained hydrocarbons in H-SSZ-13 after 5, 10, 15, 20 and 25 min of methanol feed at 400°C

change until 25 minutes on stream. At 400°C a three ring aromatic compound was observed already after 10-15 minutes on stream.

The total amount of deposited hydrocarbons was highest for H-SSZ-13 but the difference was not as pronounced as at lower temperatures (Fig. 6.39).

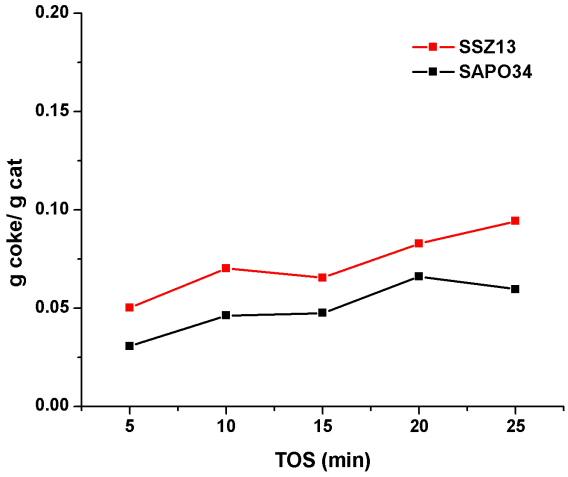

Figure 6.39: Amount of hydrocarbons in quenched material (both external and internal hydrocarbons), at 400°C, as measured by TGA

6.3.6 Comparing changes with temperature

Figure 6.40a shows the stability of H-SAPO-34 for the conversion of methanol at different temperatures. This series resembles the series shown in Figure 6.2 but in the latter 450°C is included, and 325 and 375°C are omitted. As mentioned in section 6.3 on page 60, a new series was required, as the down-scaling was not perfectly linear. However the trends were the same, with an increase in capacity as the temperature was increased to 400°C. H-SSZ-13 displayed the same trend with respect to temperature - a steady increase in conversion capacity up to an optimum temperature, which for was between 350 and 375°C (Figure 6.40b).

The amount of methanol converted per gram catalyst is a possible measure of how active the catalyst is. Figure 6.41 shows how much methanol had been converted from start until the activity had decreased to 20%. The height of the column gives the amount converted, and the number above shows the time on stream when the 20% conversion limit was reached. For H-SAPO-34 the total amount converted increased with temperature up to 23 g methanol per g catalyst at 400°C. The total capacity of the H-SSZ-13 however, increased to a maximum of 17 g methanol converted at 375°C with a subsequent decrease. It is clear how the activity of the catalysts switched with H-SSZ-13 being most stable (and converting more methanol) at lower temperatures, and H-SAPO-34 at higher tem-

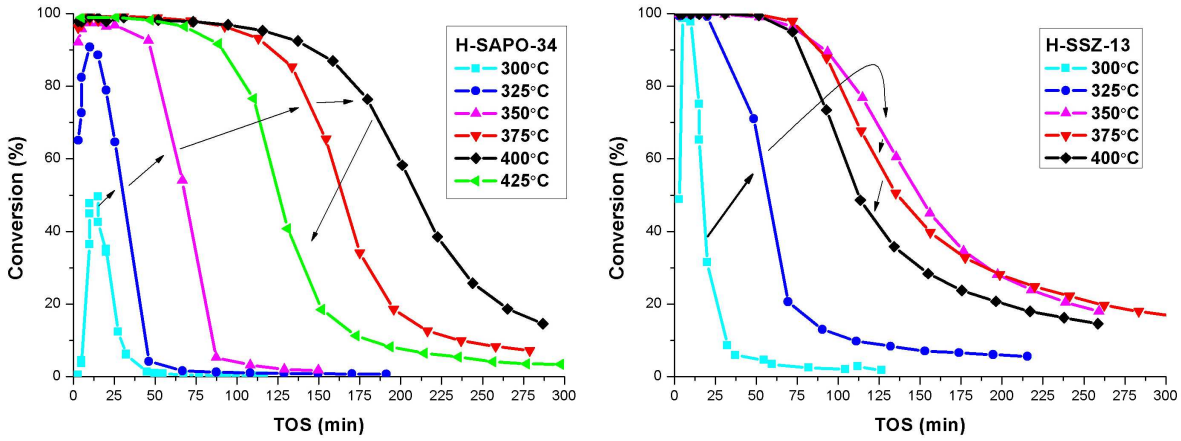

(a) (b)

Figure 6.40: Conversion of methanol over H-SSZ-13 as a function of time on stream (TOS) at 300, 325, 350, 375 and 400°C. The arrow indicates the increase in temperature.

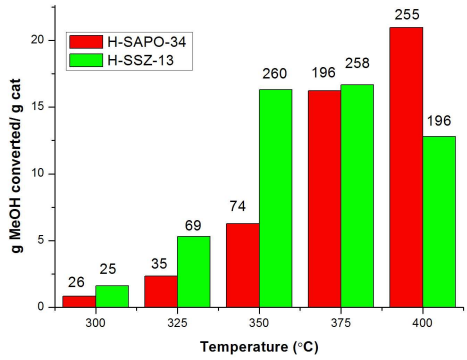

Figure 6.41: Total methanol converted by the time the catalyst was deactivated to 20 % conversion. Given in g methanol/g catalyst for the temperatures 300, 325, 350, 375 and 400°C. The number over the bars indicate the time on stream when the activity had decreased to 20% .

peratures. Under these conditions the maximum capacity of H-SSZ-13 (~ 16g methanol/g cat) did not reach the same level as the maximum capacity of H-SAPO-34 (~ 23g methanol/g cat). However, at their respective optimum temperatures they were deactivated to 20% 20% conversion at approximately the same times on stream (TOS). The reason for the difference in total conversion capacity is that H-SAPO-34 converted all methanol for a longer time, but then deactivated faster.

Figures 6.42a and 6.42b show the changes in the C_2/C_3 ratio with temperature for the two catalysts.

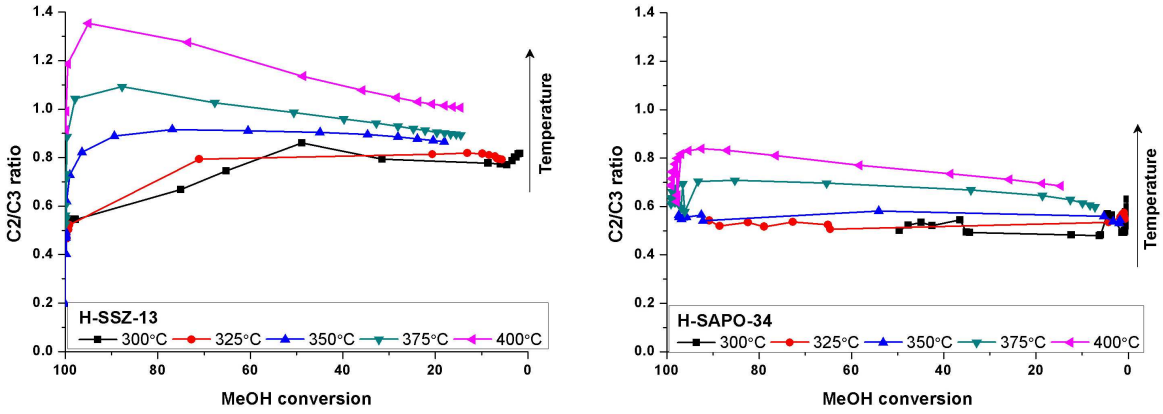

(a) (b)

Figure 6.42: The changes in the C_2/C_3 ratio with methanol conversion for (a) H-SSZ-13 and (b) H-SAPO-34 at the different temperatures.

The C_2/C_3 ratios are given as functions of methanol conversion. Again the higher C_2/C_3 ratio in H-SSZ-13 compared to H-SAPO-34 is displayed. For both H-SAPO-34 and H-SSZ-13, the C_2/C_3 ratio increased with temperature, which means that a higher temperature favored the smaller product in the effluent. However, H-SSZ-13 covered a much greater range. While in H-SAPO-34 the ratio was always smaller than one, and thus there was more C_3 than C_2 formed, the ratio was smaller than one for H-SSZ-13 only at the lower temperatures. At 375 and 400°C the C_2/C_3 ratio in H-SSZ-13 was greater than one except for when the catalyst was very fresh.

The C_2/C_4 ratios for the two catalysts at the different temperatures are displayed in Figures 6.43a and 6.43b. Also for this ratio H-SSZ-13 covered a greater range, but, except for at 300°, the ratios converged to the same value with deactivation. The ratios for both catalyst increased with temperature, so a higher temperature favored the production of the lighter compound. Also, the C_2/C_4 ratio was more stable in H-SAPO-34 than in H-SSZ-13.

The amount of hydrocarbons deposited per gram catalyst varied with temperature and time (Figure 6.44). As already seen in the previous sections, more hydrocarbons were formed on H-SSZ-13 than on H-SAPO-34 at all temperatures. This was true also at the lower temperatures (300 - 350°C) where the total capacity of converting methanol was higher for H-SSZ-13. The amount of hydrocarbons increased rapidly during the first period, and then leveled off. This was especially true at the

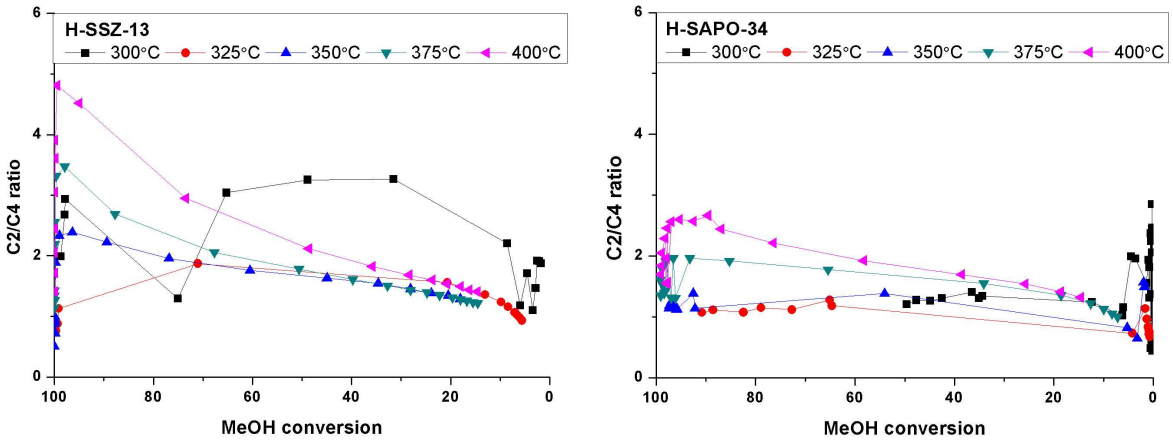

(a) **(b)**

Figure 6.43: the changes in the C_2/C_4 ratio with methanol conversion for (a) H-SSZ-13 and (b) H-SAPO-34 at the different temperatures.

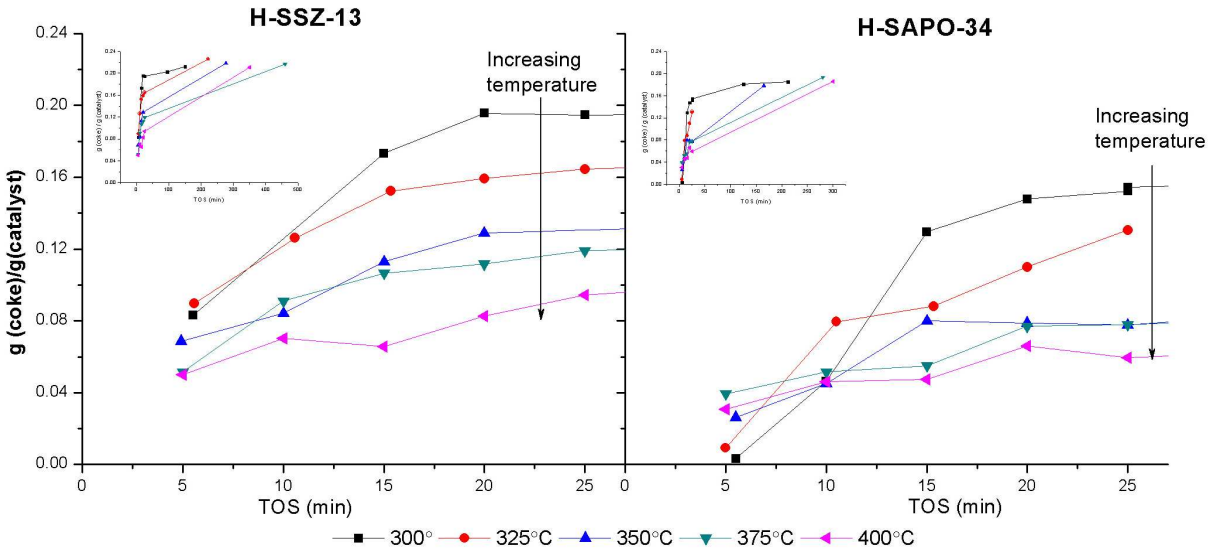

Figure 6.44: Total amount of coke formed on H-SSZ-13 (left) and H-SAPO-34 (right) with time and temperature. Inserts include long times on stream.

lowest temperature, 300°C, where the mass that was oxidized in the TGA did not increase much after 20-25 minutes on stream (inserts in Fig. 6.44). It was also interesting to note that the total amount of hydrocarbons deposited after 25 minutes decreased with increasing temperature. After 25 minutes on stream, 0.20 g hydrocarbons were deposited on H-SSZ-13 at 300°C. At 400°C it had decreased to 0.10 g coke/g catalyst. The same trend holds for H-SAPO-34, but the total amount of hydrocarbons was always lower in H-SAPO-34 than in H-SSZ-13. The inserts include the amount of hydrocarbons deposited on the catalyst after long times on stream. Since none of the long time experiments were stopped at the same time these tests were not directly comparable. The tests were stopped at different activity, but all tests converted less than 20% methanol at the time of quench. Even though they are not directly comparable the graphs indicate that approximately the same amount of coke was formed on the catalyst regardless of temperature. Also, there was consistently slightly less coke formed in H-SAPO-34 than H-SSZ-13 also after long times on stream.

It is interesting that the amount of hydrocarbons decreased with temperature, also past the optimal temperature for the conversion of methanol, as seen for H-SSZ-13. This shows that deactivation was not directly proportional to the amount of hydrocarbons formed in the system. It is plausible to think that coke formation is connected to deactivation, but the nature of the deactivating hydrocarbons is not known. As an example, hydrocarbons formed in the pore openings may block access to the active part of the catalyst (Brønsted acid sites inside the pores) and thus lead to deactivation. If the formation of this type of hydrocarbons is enhanced more than non-deactivating hydrocarbons at higher temperatures, less hydrocarbons may be formed in total, even with quicker deactivation.

The hydrocarbons formed and retained inside the catalyst can be divided into groups according to the number of carbon rings in the compound. During the first 25 minutes on stream no pyrene (4-ring) was formed in either of the two materials in the temperature range studied. Figures 6.45 and 6.46 show the distribution of one-, two- and three-rings formed inside the pores of the two materials.

In H-SSZ-13 there was a clear trend in that there were mainly one-ring hydrocarbons formed initially and that the fraction of two- and three-rings increased with time on stream. This was the case for all temperatures. Three-ring compounds were formed in H-SSZ-13 during the first 25 minutes at all temperatures except 350°C. 350°C was also the optimum temperature observed for H-SSZ-13 under

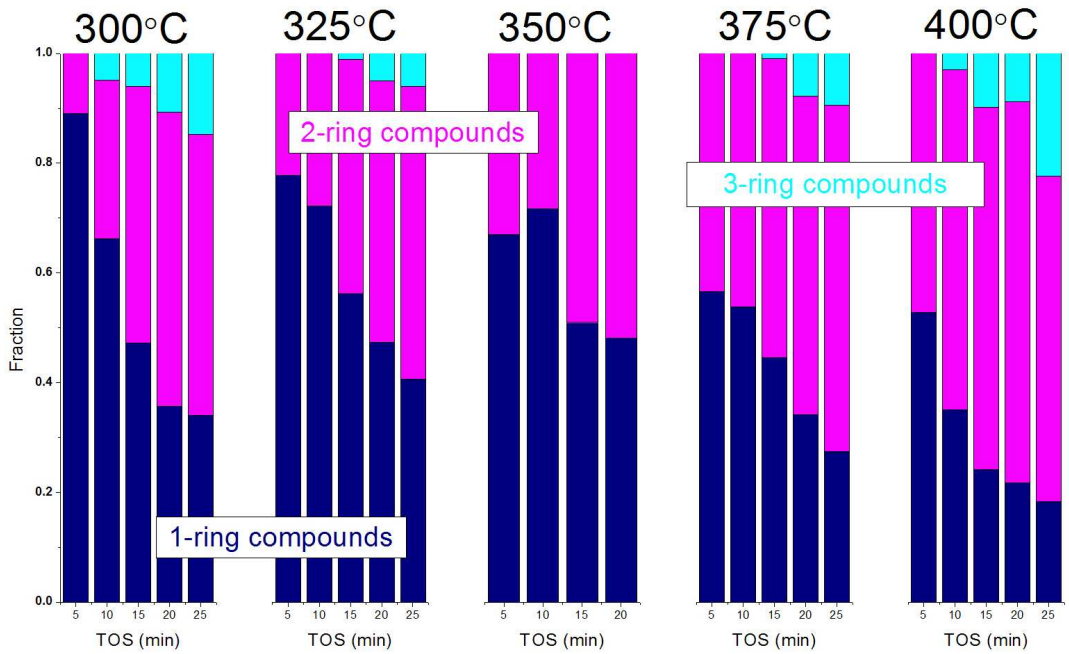

Figure 6.45: Relative distribution of one-, two and three-rings in H-SSZ-13.

these conditions, but note that H-SSZ-13 displayed full conversion for more than the first 25 minutes at all temperatures except 300°C.

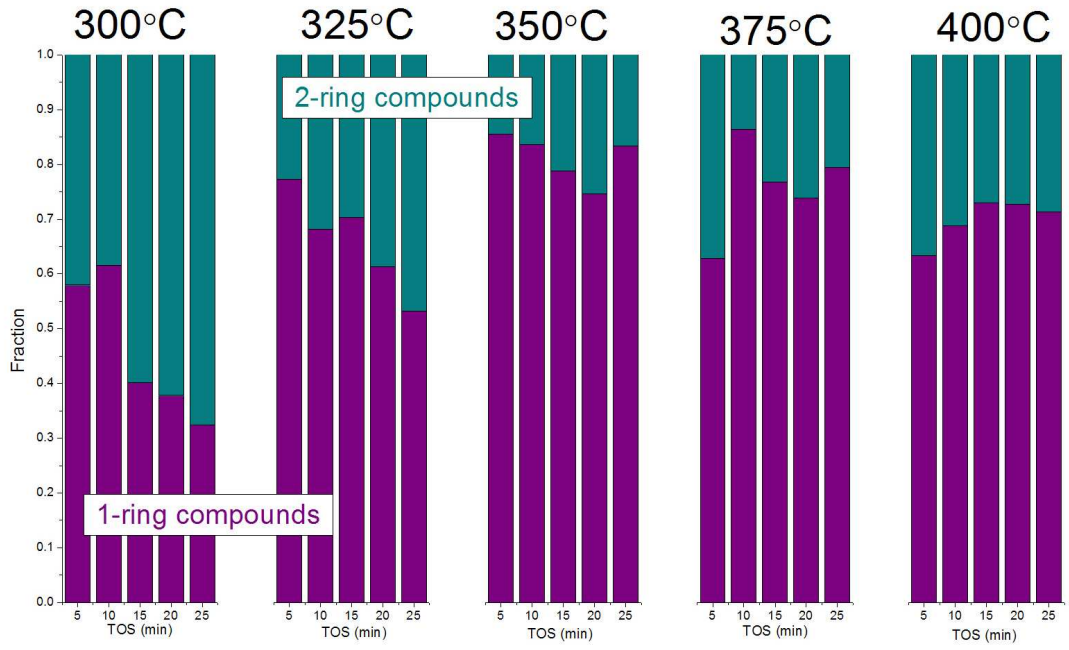

Figure 6.46: Relative distribution of one-, two and three- rings in H-SAPO-34.

For H-SAPO-34 there was not such a pronounced trend in the distribution of one- and two-rings in the retained material during the first 25 minutes. First, there were no three-rings present in the dissolved material under these conditions. Also, it should be noted that the fraction of two-rings was much bigger at 300°C than at the other temperatures. The trend with increasing amount of bigger rings with time was not so clear in H-SAPO-34 as it was in H-SSZ-13.

It should be noted that the amount of soluble hydrocarbons goes through a maximum at all temperatures. This is consistent with the idea that the medium sized hydrocarbons (which are soluble) react further to form bigger, non-soluble compounds. The problem with this view is that the hydrocarbons are thought to occupy the cages inside the catalyst and these cages can only fit compounds as big as pyrene which is soluble. Possible explanations are that the compounds within the cage decomposed with time and then reacted with the coke on the surface of the catalyst, that big compounds connected through the windows forming bigger compounds or that the compounds became insoluble for other reasons, for instance further dehydrogenation. Another contradictory point was that this decrease in hydrocarbons extracted with CH_2Cl_2 was not directly connected to visible coke. However, at long times on stream, coke that was not soluble in HF or CH_2Cl_2 was formed (identified as black particles in the solvent).

After 5 hours on stream the catalysts were almost completely or partially deactivated, and non-soluble coke had been formed on the surface of the catalyst. At this time the total wt% of deposited hydrocarbons in the catalyst was around 20% for H-SSZ-13 and 18% for H-SAPO-34. This was less than what it would have been if all the cages of the catalyst were filled with one pyrene each, 28%. After 5 hours on stream the catalysts were almost completely or partially deactivated, and non-soluble coke had been formed on the surface of the catalyst. This means that the wt% hydrocarbons within the catalyst was less than what the cages can contain at maximum.

6.4 Flushing experiments

Flushing experiments were performed at 300 over H-SSZ-13 and over both catalysts at 350°C. At 300°C methanol was passed over H-SSZ-13 for 15 minutes and then the system was flushed in Helium for 5, 15, 30 and 60 minutes. At 350°C methanol was fed for 20 minutes before flushing. These times of feed prior to flushing were chosen in order to start flushing when there were most soluble hydrocarbons in the catalyst. Flushing of H-SAPO-34 at 300°C was also performed, but the amount of soluble hydrocarbons was very small giving a high level of noise in the chromatograms. 300°C was initially chosen because reactions are more easily followed at lower temperature when they are slower.

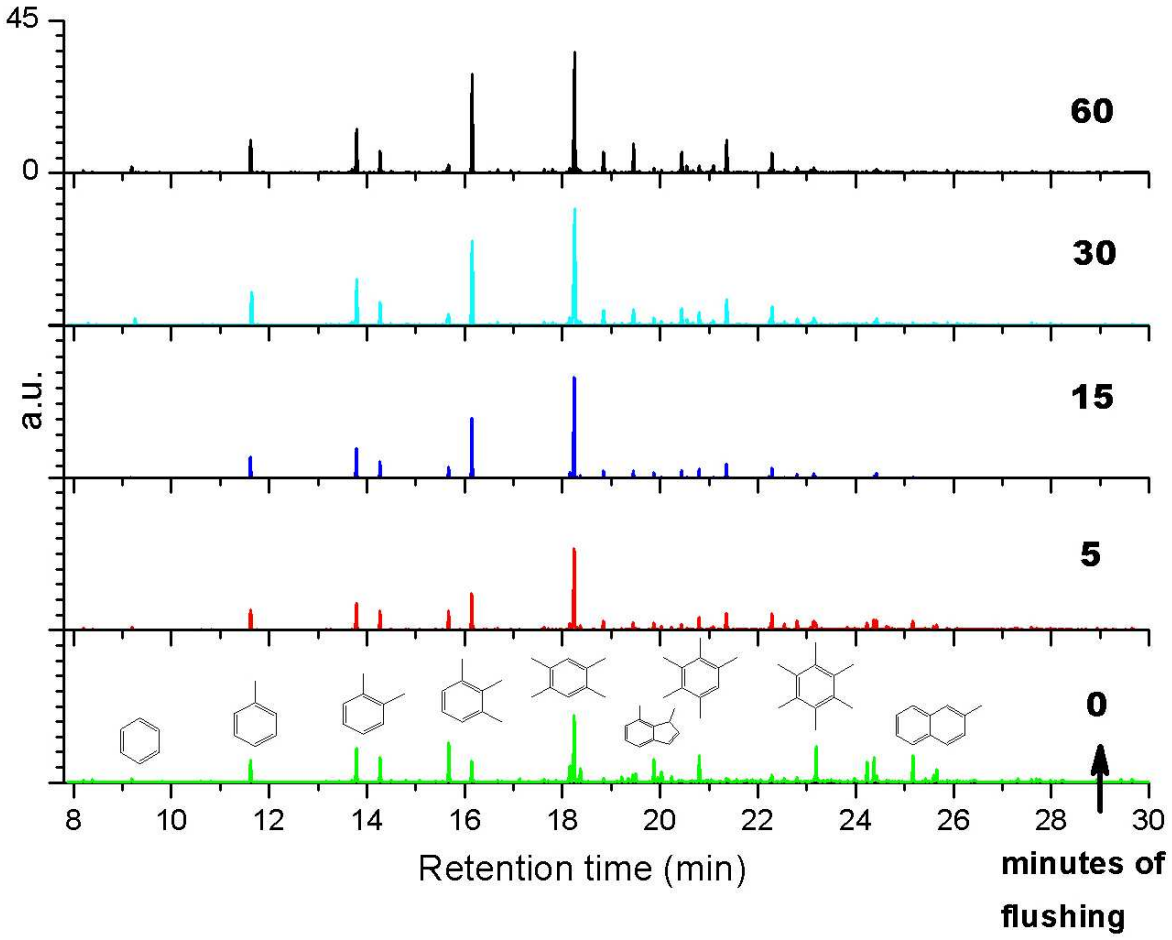

Figure 6.47: Composition of retained hydrocarbons in H-SSZ-13 at 300°C after 15 min methanol feed followed by flushing

Figure 6.47 shows the change in soluble material when flushing for various times after 15 minutes

methanol feed over H-SSZ-13 at 300°C. The main changes were during the first 5 minutes of flushing and then the chromatograms changed more gradually. All methylated benzenes up to tetramethylbenzene increased with flushing, while penta- and hexamethylbenzene decreased. 1,3,5-trimethylbenzene was the biggest of the trimethylbenzenes after 15 minutes of methanol feed, but flushing rapidly changed the order so that the most stable isomer, 1,2,4-trimethylbenzene, was the most abundant.

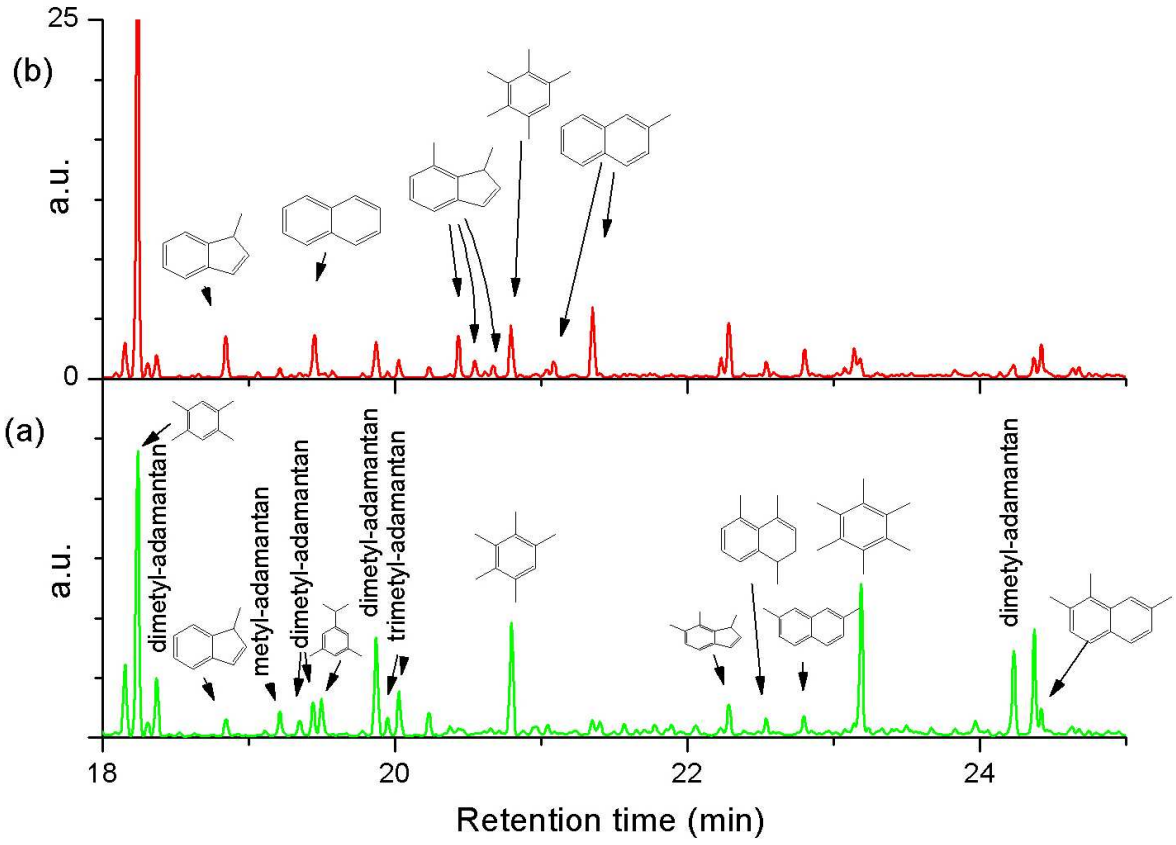

Figure 6.48: Composition of retained hydrocarbons in H-SSZ-13 at 300°C after 15 min methanol feed (a) followed by flushing for 15 minutes (b). The region where two-ring compounds were eluted is displayed in more detail.

The part of the chromatogram where two-rings were eluted is presented in more detail in Figure 6.48, for 0 and 15 minutes flushing. Clearly penta- and hexamethylbenzene disappeared, while several two-rings were formed, such as naphtalene and methylnaphtalene. Also methylated indenes were formed during flushing, but methylated adamantanes disappeared slowly.

Since the amount of soluble hydrocarbons in H-SAPO-34 at 300°C was too small for flushing studies, the two catalysts were compared at 350°C. The retained soluble material, after 20 minutes methanol feed and subsequently 1 hour of flushing, changed similarly in both materials (Fig. 6.49 for H-SAPO-

34 and Fig. 6.50 for H-SSZ-13), but there were some significant differences. Figure 6.49 shows that the main component in H-SAPO-34 was tetramethylbenzene both before and after flushing. All methylbenzenes up to pentamethylbenzene were present in the quench before flushing. Toluene, di-, tri- and tetramethylbenzenes increased, while pentamethylbenzene completely disappeared. Before flushing there were very few two-ring structures retained in H-SAPO-34, but after, methylated naphtalenes and indenes were present.

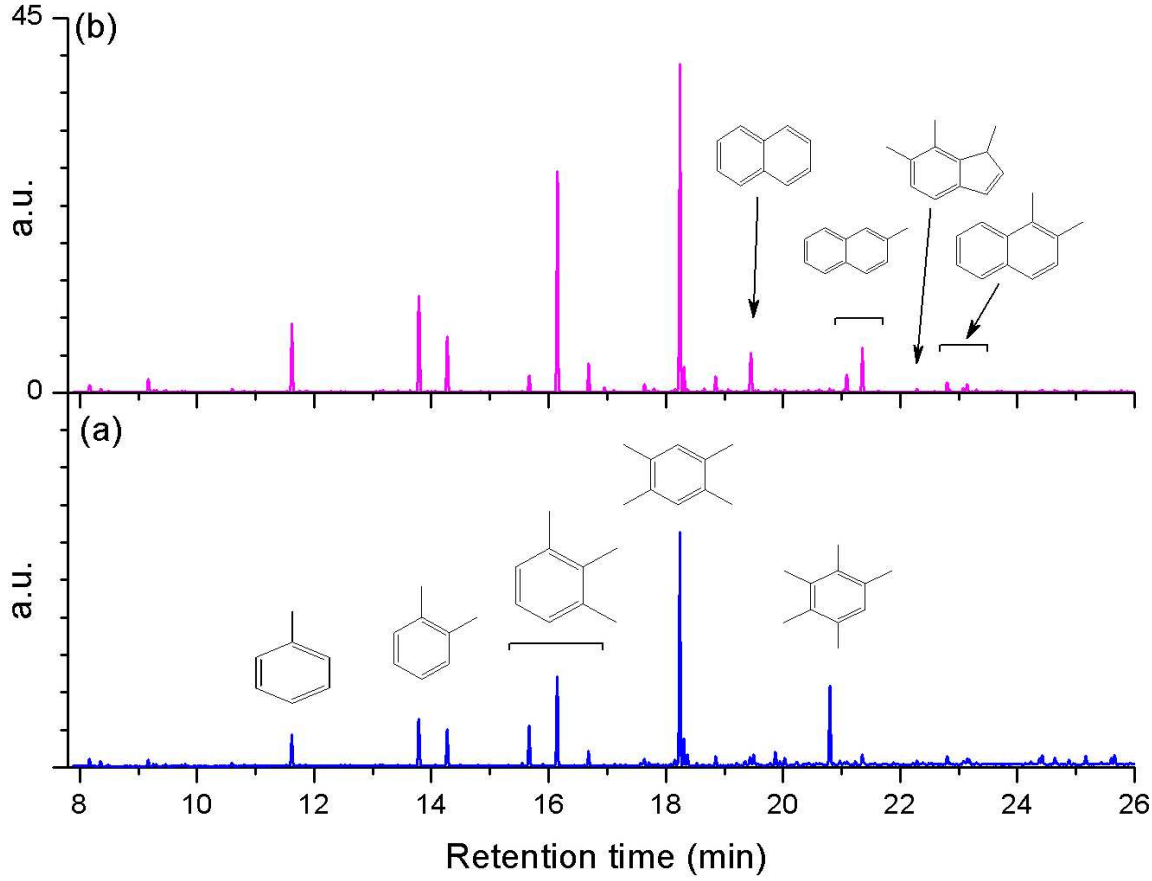

Figure 6.49: Composition of retained hydrocarbons in H-SAPO-34 at 350°C after (a) 20 min methanol feed, and (b) 20 min methanol feed followed by 1 hour flushing in He

Figure 6.50 shows that the evolution of species inside H-SSZ-13 with flushing was different from that of H-SAPO-34, although the type of retained compounds where the same. As in H-SAPO-34, all methylated benzenes up to pentaMB were present in H-SSZ-13. However the pentamethylbenzene peak was very small in H-SSZ-13. Also there was a difference in the trimethylbenzene peaks. In H-SAPO-34 all three compounds were eluted. The NIST98 database was not able to distinguish between these peaks, but since the compounds were eluted in order of boiling point the first peak

was assigned to 1,3,5-trimethylbenzene, the second to 1,2,4-trimethylbenzene and the third to 1,2,3-trimethylbenzene. Only the second peak was present in H-SSZ-13 while all three were present in H-SAPO-34. In addition there were two-rings present in H-SSZ-13 after 20 minutes of methanol feed. With flushing, the amount methylated benzenes with up to three methyl groups increased slightly, but the amount of tetramethylbenzenes decreased significantly (while it increased in H-SAPO-34). The initially very small peak of pentamethylbenzenes completely disappeared. After flushing the biggest peak was naphtalene, which had increased significantly. Also the amount of methylbenzenes increased slightly, while the methylated indenes decreased.

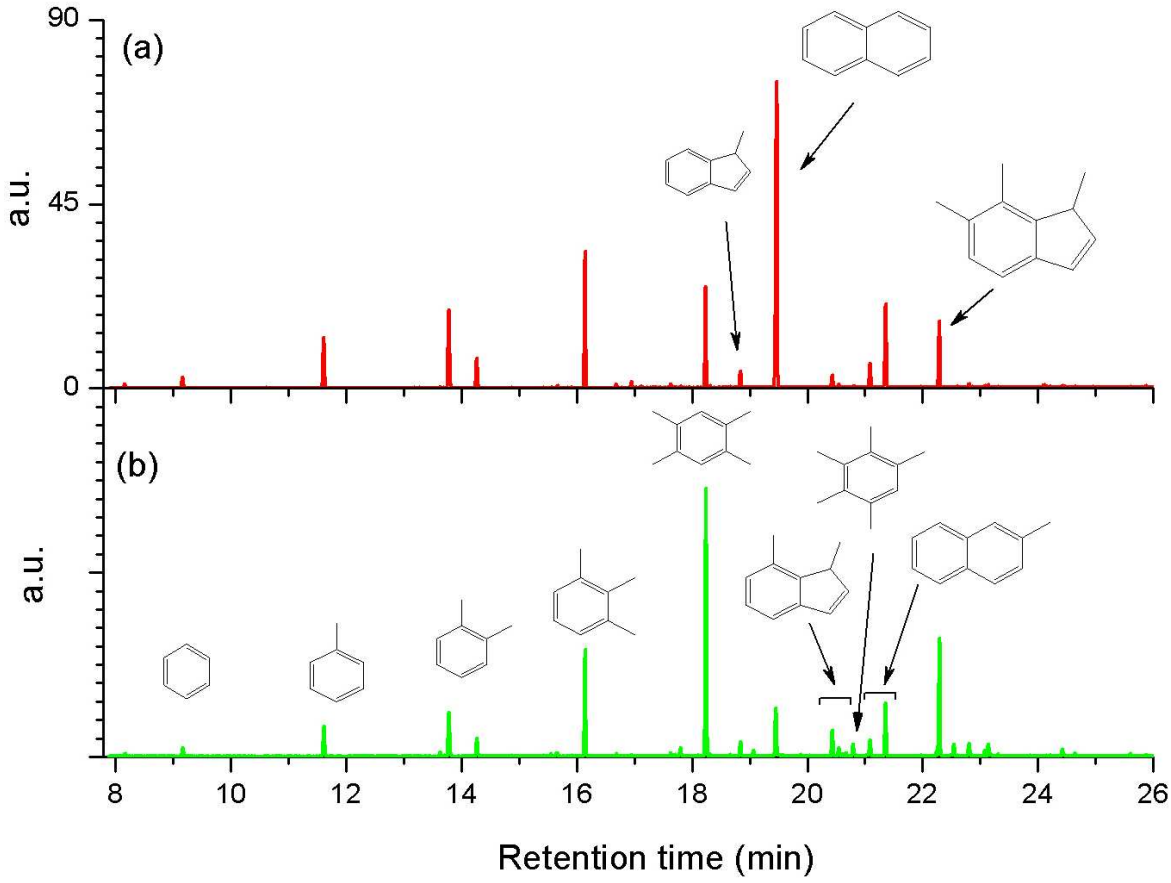

Figure 6.50: Composition of retained hydrocarbons in H-SSZ-13 at 350°C after (a) 20 min methanol feed, and (b) 20 min methanol feed followed by 1 hour flushing in He

H-SSZ-13 at 350°C differed from H-SAPO-34 at 350°C and H-SSZ-13 at 300° in very similar ways. The decomposition of a compound upon flushing was taken as an indication of protonation, since the mechanisms are believed to go through a protonating step at the acid site. At the lower temperatures

H-SSZ-13 did not seem to protonate tetramethylbenzene, and neither could the less acidic H-SAPO-34 at the higher temperature. Thus reducing temperature and reducing acidity had much the same effects. Note however that adamantanes were found almost exclusively in H-SSZ-13 at the lower temperature.

The amount of catalyst decreased considerably within the first 2-5 minutes of flushing at 350° C (Fig. 6.51). Note that the relative amount of hydrocarbons that disappeared was double as high in H-SAPO-34 compared to H-SSZ-13. This indicates that the rate of formation of deactivating coke was higher in H-SSZ-13. However, such a comparison should rather be done at the same point of deactivation and coke content. Again, H-SSZ-13 contained considerably more coke than H-SAPO-34.

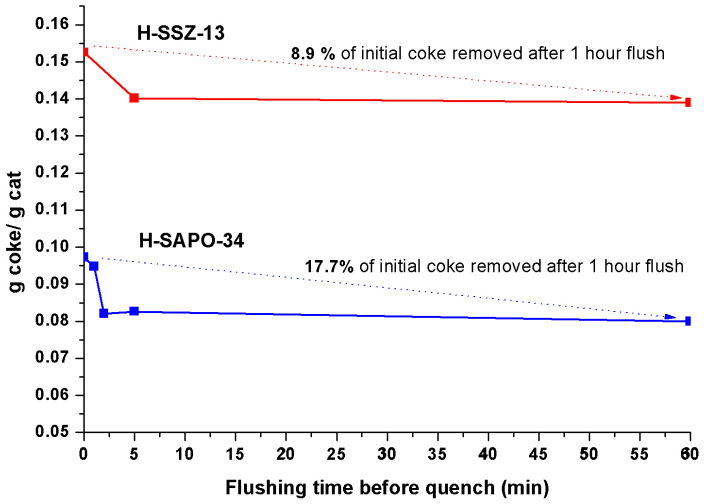

Figure 6.51: Removal of deposited hydrocarbons by flushing, as measure by TGA. H-SSZ-13 contains more coke than H-SAPO-34 initially, and less coke decomposed upon flushing.

6.5 Variation of WHSV

The effect of doubling the WHSV (g methanol/(g catalyst hr)) was investigated by keeping the linear flow constant while the amount of catalyst was halved. Figure 6.52 shows the conversion of methanol over H-SAPO-34 as a function of methanol fed per gram catalyst, for WHSV 6.0 hr^{-1} and 12.4 hr^{-1}.

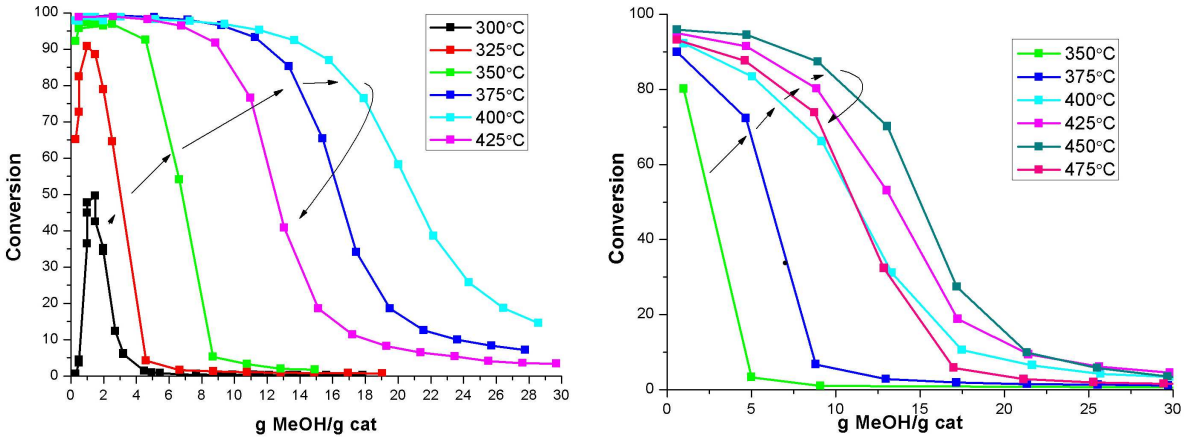

(a) WHSV = 6.0 g/(g hr) **(b)** WHSV = 12.0 g/(g hr)

Figure 6.52: Methanol conversion as a function of methanol fed over H-SAPO-34.

The Figures give conversion as a function of the total amount of methanol passed over each gram catalyst from start, so if the conversion had been independent of contact time, the two graphs should have been identical. At higher space velocities (shorter residence time), each gram of zeolite converted less methanol. Also, the optimum temperature changed when residence time was altered; halving the residence time increased the optimum temperature by 50°C.

It is also interesting to note the methanol to DME ratios. After conversion to hydrocarbons had stopped, the catalysts were still active for the condensation of methanol to DME, but under the present conditions this reaction did no reach equilibrium. The MeOH/DME ratio was usually around 2-10 after deactivation in both catalysts with WHSV=6.0 hr^{-1}. Cutting the residence time to one half gave a ratio of about 40 in H-SAPO-34. There was no obvious trend with temperature. For comparison, in the same temperature range the equilibrium ratio was from 0.2 to 0.5, which means that there was more DME at equilibrium. This indicated that there was not full equilibration of methanol and

DME under the present conditions. However, all the ratios were calculated at the point with most deactivation, and they did not say anything about what happened while there was catalytic activity. While there was full conversion there was no DME and methanol coming out of the reactor, and during deactivation the oxygenates may have been reacting at different rates so that the ratio does not say anything about the condensation equilibrium. However the ratio was mostly in the same range, 1-4, also during deactivation.

6.6 Color of spent catalyst

The coke and hydrocarbons deposited on the catalyst had different colors. With increasing time on stream the color was stronger, consistent with there being deposited more and more hydrocarbons. H-SSZ-13 had greenish coke, while the color was more yellow/brown on H-SAPO-34. TEM analysis were performed at Haldor Topsøe to investigate coke on the surface of the single crystals. TEM pictures were taken of selection of the samples, both at short and long times on stream, but no large compounds were detected on the crystal surfaces.

Also, the extract obtained with the dissolution procedure was strongly colored. The colors ranged from bright green and pink to more yellow/brownish. This observation was not investigated further, but it would be interesting to find the molecules giving the colors.

6.7 Comparison with previously reported results

The effect of acidity on the MTO-reaction over catalysts with the CHA-topology have been studied previously [65, 66, 67]. Yuen et al. varied the acid site density for H-SSZ-13, and found that a Si/Al ratio of 9 was better than both 4.5 and 29 (double life time with LHSV=3.7, 400°C, and 22% methanol in water as feed). Si/Al=9 was closest to the samples in the present study. The acid site density for H-SAPO-34 was not reported. The present results are in agreement with those of Yuen at al. who found that the lifetime of H-SAPO-34 at 400°C was much significantly better than that of H-SSZ-13. They also reported a high C_2+C_3 selectivity for both catalysts ($\sim$ 85%), but H-SSZ-13 gave

more alkanes. The present study did not discriminate between C_2 and C_3 alkanes and alkenes. The above mentioned study aimed at investigating which of acidity and pore sizes dominated the reaction most, and they found that pore sizes had greater influence on product distribution.

Wilson et al. investigated what characteristics of H-SAPO-34 influenced the conversion of methanol to light olefins. Their study did not concern variation of acid strength, but rather the acid site density. They found that varying acid site density had great effects on the lifetime of the catalyst, and one acid site per cage was found to be the best. The optimum density in H-SSZ-13 might, however, be different. The materials compared in this thesis had approximately the H-SAPO-34 optimum acid site density.

Dahl et. al did another comparison with WHSV=70 hr^{-1} and found again that H-SSZ-13 had a smaller conversion capacity than H-SAPO-34. However, they did not compare catalysts with the same acid site densities, and also concluded that deactivation rates depended more on acid site density than chemical composition. Under the present reaction conditions, H-SAPO-34 had a longer lifetime than H-SSZ-13, but it was also found that WHSV has a great influence on the optimum temperature of the catalyst. Thus, several parameters influence the catalytic activity strongly, and it may still be that H-SSZ-13 is better than H-SAPO-34 under different conditions. Furthermore, the acid site of the zeotype is undoubtedly significant for catalytic activity, and understanding the effect of varying acid strength may give valuable information on the mechanisms, thus bringing research closer to new and improved catalysts.

6.8 Other possible factors

The main assumption in this thesis was that the only characteristic that was different for the two catalysts was the acid strength. This means that for instance crystal sizes were the same. Although the crystal sizes were similar, they were not equal. Also, it is not likely that changing the chemical composition of the framework only had an effect on acidity. In the zeolite the framework atoms are mostly Si which have similar charges (variations due to Al in the framework). In the aluminophosphate the alternating Al and P introduce an unequal distribution of charge on the T-atoms. One effect of this is

that the zeolite is hydrophobic while the zeotype is hydrophilic [9]. Also the average number of acid sites per cage is not necessarily the same as a uniform distribution of acid sites. If the densities of acid sites in the two catalysts vary much, they are no longer so easily comparable.

The above mentioned factors may lead to errors in the interpretation of the results, since assumptions may lead to wrong explanations of what is observed.

In addition, unknown sources of error in the experiments may have been present, such as catalyst amount, temperature variations, feed flow and methanol partial pressure. Another source of error is that the limited amount of catalyst prevented repetition of all experiments. Initial studies were performed to assess reproducibility. These showed excellent reproducibility on the setup (cfr. deactivation and selectivity curves consist of many separate catalytic tests), but this does not mean that all experiments were performed correctly. In cases were the results did not fall into a trend, the tests were repeated as long, as there was catalyst available.

6.9 Further work

The work in this thesis does not stand alone. It is a continuation of the work done previously in the group and there is ample space for continuing this work further. The following list suggests experiments in direct continuation to what is presented here:

1. **Measure acidity with other methods** Acidity may be measured by for instance ammonia temperature dependent desorption

2. **Stability tests at other (higher) residence times.** With the feed being in contact with the catalyst for longer time, it has longer possibilities to react. This means that the system has more time to reach equilibrium before the compounds go into the effluent. Does increasing residence time decrease the optimum temperature further? Is it possible to vary residence time in such a way that the two catalysts have the same optimum temperature? If this is the case, the two materials can be compared when deactivation curves and coke content are similar, thus indicating if

the nature of the coke in the two catalysts differ in such a way as to influence the product selectivities.

3. **Flushing experiments** The present results indicate that H-SSZ-13 can protonate tetramethylbenzene under conditions when H-SAPO-34 cannot. In addition there were smaller differences in other compounds, which may be elucidated with more thorough flushing experiments, for instance what compounds give rise to the formation of two-rings.

4. **Labeling experiments** In continuation to flushing experiments, using labeled and unlabeled methanol resolve the rate of incorporation of methanol in the effluent and retained hydrocarbons. Are all products formed equally fast? Which of the retained hydrocarbons are most active and more likely to be of major importance in the hydrocarbon pool? It may also be possible to follow the variations in the mechanisms with deactivation by changing the time before onset of labeled methanol.

5. **The role of the adamantanes** Adamantane derivatives fit very well into the cage of the chabazite structure, and they are also formed during the reaction. Are they coke precursors, reaction intermediates, or ”dead ends” in the reaction?

6. **Investigations on the colours of the spent and dissolved catalysts** What are the compounds that produce the colours?

Other studies may give a greater understanding of factors that influence the mechanisms of the MTO-reactions.

7. **Varying acid site density** Not only the acidity but the density of acid sites may be varied, and it is likely that there is such an optimum density. As previously mentioned one acid site per cage has been found to be optimum for H-SAPO-34.

8. **Topologies with same acidity** Find related topologies that have the same acidity. How does topology influence the reaction in more detail than what is known about MTH on various zeolites?

9. Other zeotypes with the same structure There is a long list of materials with the same crystalline structure, but with different chemical composition. If acidity can be controlled by chemical composition it may be possible to find an optimum acidity for the reaction.

Chapter 7

Conclusions from experimental work

The main conclusion of the comparison of H-SSZ-13 and H-SAPO-34 as catalysts for the MTO reaction was that they were very similar; there were few differences in both products and retained hydrocarbons. However, the more acidic catalyst, H-SSZ-13, deactivated faster than H-SAPO-34 at higher temperatures. At the lower temperatures H-SSZ-13 displayed a higher conversion capacity than H-SAPO-34. Also there was a difference in optimum temperature for the two catalysts. Under otherwise equal conditions, the more acidic catalyst had a lower optimum temperature. Increasing temperature and increasing acidity should increase the rate of the reactions involved, and thus the shift in optimum temperature was not very surprising. Also changing the residence time of methanol shifted the optimum temperature, but this time to a higher value.

The products of the reaction were the same: mainly alkanes and alkenes with one to four carbon atoms and a few compounds with five C. The C_1 to C_4 fraction had a selectivity of more than 90% and with deactivation the amount of C_{5+} rapidly decreased to 0%. For both catalysts the C_2 and C_3 peaks were biggest at all temperatures; the selectivity towards C_2 + C_3 was around 60-80% for both catalysts.

The initial selectivities were very similar. This result suggested that the solids alone were very similar as catalysts, and that they only changed as hydrocarbons were formed inside and outside the pores. The different acidities gave rise to slightly different hydrocarbons retained in the crystals, which can

both have mechanistic effects and influence diffusivities in the crystals. For instance, molecules that clog the catalyst may have been formed more easily in the more acid material. The relative rates of formation of deactivating and non-deactivating hydrocarbons might also have been different for the two catalysts.

Although there were some differences, the retained material was very similar for the two catalysts. The same methylated benzenes were formed and the most abundant of these was tetramethylbenzene in both materials. Bigger ring-compounds were also formed, and the largest aromatic ring was pyrene. Formation of the heavier fraction of retained hydrocarbons increased with time, and thus also with deactivation. Also in the retained material increasing temperature and acidity had similar effects in that they gave a shift towards heavier hydrocarbons under otherwise equal conditions. Again, this could be explained as due to increasing reaction rates with acidity and temperature. The biggest difference in the retained material for the two catalysts was that there was a greater variety in the retained hydrocarbons in H-SSZ-13. A the same temperature H-SSZ-13 could protonate tetramethylbenzene, while this was not done by H-SAPO-34. Higher acidity gave a greater capacity for protonating other compounds.

More hydrocarbons are formed in H-SSZ-13 than H-SAPO-34, which is in agreement with increased reaction rates with acidity. It should be noted that the amount of soluble hydrocarbons goes through a maximum at all temperatures, while the total amount of hydrocarbons, as measured by TGA, increases, suggesting that soluble hydrocarbons develop into non-soluble species.

Chapter 8

Results and discussion of calculations

8.1 Choice of method

For the theoretical work in this thesis density functional theory (DFT) with periodic boundary conditions (PBCs) was used to calculate the electronic ground state as well as ground state frequencies of solids with adsorbed molecules. Generalized gradient corrected (GGA) functionals were chosen because hydrogen, in particular, is much better described with GGA than the local density approach (LDA) based on the free electron gas. The calculations were carried out using DMol^3 in Material Studio version 4.2. DMol^3 uses atom-centered basis functions, where each function corresponds to an atomic orbital. These basis functions are numerical, which means that they are given numerically as values on an atomic-centered spherical-polar mesh and not as analytical functions. The radial part of each function is then obtained by solving the DFT equations numerically for the atoms. The spherical harmonics are used for the angular part. The Double Numerical plus Polarization basis set (DNP) was chosen, which contains two basis functions per orbital, and in addition one polarizing d-orbital on non-hydrogens and a p-orbital on hydrogens. Numerical basis sets are effective compared to size, they are more effective than an equally big basis set with gaussian functions. Also, they give a good description of weak bonds since they minimize the effects of basis superposition [68]. Geometry optimizations were performed with convergence tolerance 10^{-5} Ha for the energy, 0.002 Ha/Å for the

forces and 0.005 Å as maximum displacement. The wavefunction was optimized with 10^{-6} Ha as convergence threshold. The calculations were performed without spin polarization (spin-restricted). Calculations were performed on desktop computers.

8.1.1 Choice of unit cell

H-SSZ-13 and H-SAPO-34 were the two solids studied in this thesis. Both materials are crystalline with the same zeolite structure (CHA), but with different chemical composition, as described previously. Geometry optimizations were performed with adsorption of methanol and CO on the four possible acid sites, and in order to distinguish the sites the four oxygens attached to the aluminum were named O1, O2, O3 and O4. SSZ-O1 indicates a calculation with the proton on O1 of H-SSZ-13, and SAPO-O1 for H-SAPO-34. Several adsorption geometries were obtained on H-SSZ-13. SSZ-O1(5) denotes geometry optimization number 5 for methanol with proton on O1.

The chabazite structure can be represented both by a rhombohedral and hexagonal cell, which contain 12 and 36 T-atoms, respectively. To test that the periodic representation did not affect the results, a geometry optimization of pure silicious chabazite with fixed boundaries was performed with both unit cells. There was no difference between the two calculations. All further calculations where performed with the rhombohedral cell because calculations with fewer atoms require less computer resources. The trigonal rhombohedral unit cell was fixed with cell length $a = 9.291$ Å and and angle $\alpha = 93.92°$ for both H-SSZ-13 and H-SAPO-34.

Initially, H-SAPO-34 was calculated in a slightly different rhombohedral unit cell, $a = 9.421$ Å, $\alpha = 94.20°$. These small alterations in the size of the unit cell had big effects on the adsorption energies. The adsorption of methanol on the O1 Brønsted acid site (Fig. 8.1a) was calculated, and the smallest unit cell gave a higher energy for both structures. This was expected because compression induces stress. The energy differences were 12 kJ/mol for H-SSZ-13 and 18 kJ/mol for H-SAPO-34, which was a significant variation for changing the cell by only 0.13 Å and 0.3°. The same change in cell parameters with only methanol (the solid removed) in the cell gave an energy difference of 0.07 kJ/mol, which was negligible. The difference in methanol adsorption calculated for SSZ-

O1(5) gave an energy difference of 5.5 kJ/mol. This is in the same order of magnitude as the energy differences found for the adsorption in the two materials. It was therefore decided to repeat the calculations for methanol adsorption on H-SAPO-34 with the smaller unit cell. This choice was made because there were fewer calculations with H-SAPO-34 (and time was scarce) and the unit cell used in the reference article had a shorter cell side (a = 9.186 Å and α = 94.76°) [61]. Also, cell optimization was tried for both materials without any acid sites (purely silicious chabazite and ALPO-34), with both the above unit cells as starting parameters. None of the calculations converged. Shah et al. obtained their cell parameters by optimizing purely silicious chabazite, but a similar calculation in DMol^3 with their optimized cell parameters as starting values did not converge either.

The materials studied in this thesis had one acid site per cage, which corresponds to one acid site per unit cell. Figure 1.8 on page 11 shows the numbering of the four topologically distinct acid sites used in this thesis. Figure 8.1 shows the unit cells for the two materials, with the proton positioned on oxygen O1 in H-SSZ-13 and on O2 in H-SAPO-34.

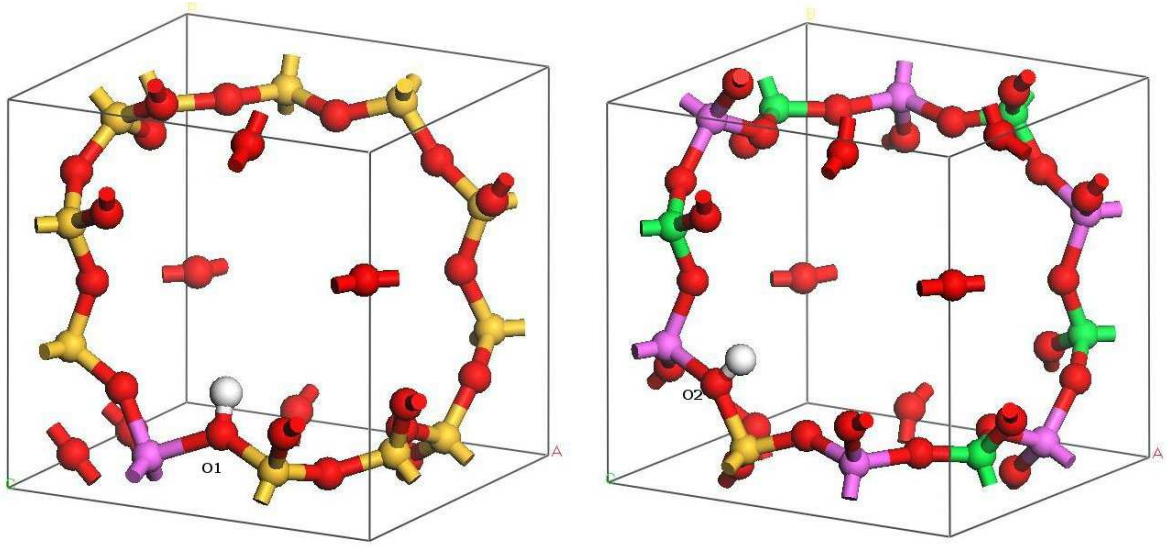

(a) **(b)**

Figure 8.1: The unit cell of (a)H-SSZ-13 and (b) H-SAPO-34, with hydrogen in the O1 and O2 position, respectively.

8.2 Methanol adsorption

Adsorption of methanol on H-SSZ-13 was studied for comparison with previously reported results ([69, 61, 60, 70, 71]).

8.2.1 Choice of setup

The adsorption energies on the four acid sites for both materials was calculated with the PBE functional (Table 8.4).

In periodic boundary calculations not only the crystal is calculated periodically, but also the adsorbed molecule. The effect of periodicity on methanol alone showed that using the energy of one gaseous free methanol molecule was not a good reference for calculating adsorption energies in periodic structures (Fig. 8.2).

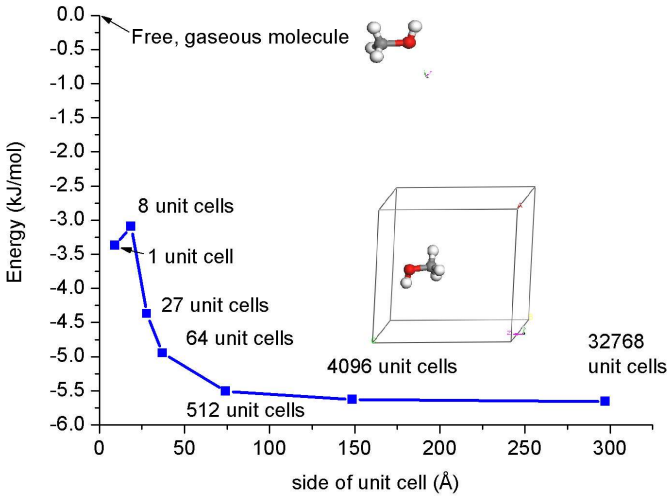

Figure 8.2: Energy of methanol calculated in periodic unit cell. The basic unit cell is the rhombohedral chabazite unit cell, and the cell is increased to 8, 27, 64, 512, 6094 and 32768 times this unit cell. The reference energy is the energy of MeOH non periodically, but otherwise same settings.

Using periodic boundary conditions, the methanol energy changed about 5.5 kJ/mol when the periodic boundaries were so large that the energy had converged. The periodic cell had to be 512 times the size of the smallest unit cell in order to reach convergence. This was far beyond the computer

capacities available. It was interesting to note that the first increase in size of the unit cell, doubling the cell length in each direction, changed the energy away from the plateau, while afterwards the energy decreased monotonously. The plateau did not correspond to the free molecule calculated non-periodically, the monotonous change was actually going away from the free molecule. This indicated that there was a difference in the way DMol^3 did the calculations, as non periodic and periodic calculations with increasing distance between molecules should in principle converge. The reason for this was probably that the zero-point of the potential was chosen differently for the periodic and non-periodic calculations. To see if this could be the explanation, the energy of two different geometries of methanol was calculated both with and without periodic boundary conditions. The energy difference of the two geometries was the same. Figure 8.2 indicates that big unit cells should be used, but this was not possible due to computational resources. Thus, periodic methanol in the smallest unit cell was used as reference for determining adsorption properties. The energy difference between methanol in one unit cell and methanol in an infinitely big unit cell (defined by the plateau) was about 2.5 kJ/mol, indicating an intrinsic error of at least this magnitude, which is of the order of kT at room temperature (kT=2.5 kJ/mol at 300K). Shah et al. found that the energy of the methanol molecule converged to within 1 kJ/mol for a 9 Å cell [61], approximately the size of one unit cell in the present work. As previously mentioned the chabazite unit cell is small for being a zeolite and thus requires comparatively little computer resources. A drawback of a small unit cell is that in calculations with periodic boundary conditions molecules in one unit cell may influence molecules in the neighboring unit cell. Therefore calculations with bigger unit cells and thus also greater distances between the adsorbed methanol molecules were performed. Increasing the unit cell in one direction enabled the calculation of one adsorbed methanol atom for two unit cells. Calculations on all three different directions were compared since methanol is an asymmetric molecule, and greater distance in the three directions may have different effects.

Table 8.1 shows results for adsorption of methanol on H-SSZ-13 with varying coverage (1 indicates one methanol per acid site). Such calculations were done by making a super-cell consisting of several basic unit cells.

Calculations with periodic boundaries set to four times the size of the smallest unit cell were carried

Table 8.1: Methanol adsorption on O1 in H-SSZ-13 with different unit cells. The size of the cell is denoted (x,y,z), so that the calculated cell is x times the smaller unit cell in the a-direction, y times in the b-direction and z-times in the c-direction. a, b, c are the vectors determining the unit cell in the rhombohedral representation.

Size of super-cell	Number of methanol molecules per acid site	Adsorption energy per methanol molecule (kJ/mol)
(1x1x1)	1	-99.23
(2x1x1)	0.5	-99.35
(1x2x1)	0.5	-98.44
(1x1x2)	0.5	-99.11
(2x2x1)	0.5	-98.32
(2x2x1)	0.25	-89.04
(2x2x2)	0.125	too demanding

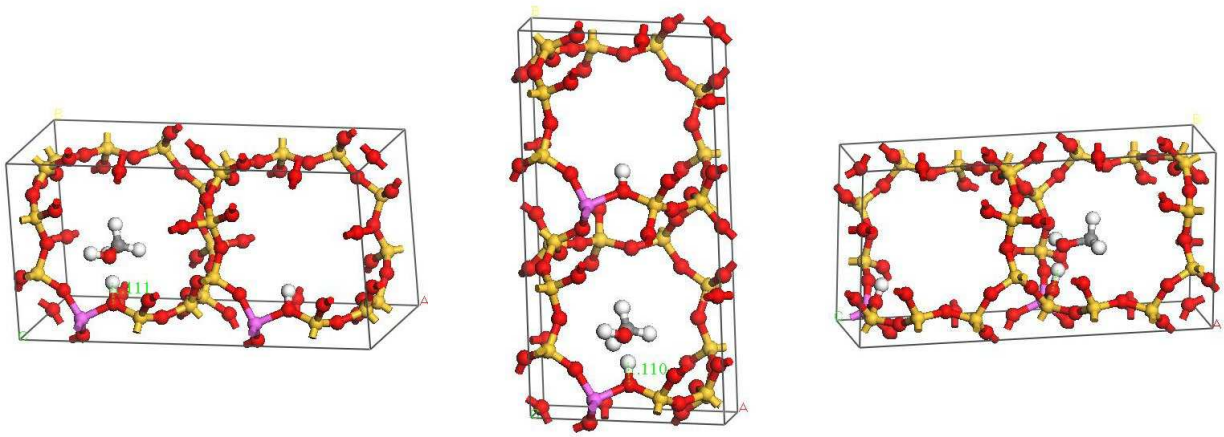

(a) ((2x1x1) **(b)** (1x2x1) **(c)** (1x1x2)

Figure 8.3: the super-cells consisting of two basic unit cells in the (a) x, (b) y and (c) z -directions. One methanol per unit cell.

out. Also eight times (doubling the size in all three directions) was tried, but these calculations were computationally too demanding (14 days on the fastest machine available). Calculations with super-cells consisting of two unit cells and one methanol were performed in all three directions (Fig. 8.3). Doubling the unit cell in the three different directions had a negligible effect on the adsorption energy, varying from +0.1 to -0.7 kJ/mol.

Increasing the super-cell in one more dimension, but keeping the "concentration" of methanol fixed, gave a 1 kJ/mol weaker adsorption (adsorption energy 1 kJ/mol less negative). Decreasing the concentration to 1/4 methanol per unit cell gave an adsorption energy 10 kJ/mol smaller compared to using only one unit cell. Thus, increasing the separation of the methanol molecules in the periodic calcu-

lations gives a weaker adsorption. There are two possible main reasons for this. In the bigger unit cell more atoms are left to relax freely. This should not have a great influence since the methanol and the H-SSZ-13 used in the adsorption calculations always were calculated in the same unit cell as the adsorption complex. The second reason for the drop in adsorption energy could be that the molecules are so close to on another as to influence each other across the periodic boundary. It is important to remember that not only the crystal lattice is described periodically (as it should) in such calculations, but also the adsorbed methanol atoms. These results show that geometry optimizations of bigger cells are to be preferred in such calculations. It would be interesting to see the effect of increasing the cell even further, in order to determine how big the cell must be, but the available computer resources did not permit such calculations. Furthermore the calculations with four unit cells where already too demanding. Also increasing the unit cell in only one direction wa s computationally demanding, and the benefit was very small compared to the cost. It would also be difficult to determine in which direction the cell should be prolonged. Thus it was decided to continue using only the smallest unit cell. In comparing the two different materials chabazite and H-SAPO-34 this choice should not compromise the results, since the topologies and thereby also the unit cells are equal. Relative differences should therefore still be comparable.

Calculations of adsorption of methanol were also performed comparing the use of different k-point sets (Table 8.2). The choice of k-point grid used in a calculation defines the accuracy of the Brillouin zone sampling. DMol^3 uses the Monkhorst-Pack k-point division. This essentially means that the sampling k-points are distributed homogeneously in the Brillouin zone, with rows or columns of k-points running parallel to the reciprocal lattice vectors that span the Brillouin zone. A detailed description of the choice of k-point set is beyond the scope of this thesis. Geometry optimizations

Table 8.2: Adsorption energies for the adsorption of methanol on the acid site in the O1 position of H-SSZ-13 (SSZ-O1), calculated with different k-point sets.

k-point set	calculation	adsorption energy (kJ/mol)
(1x1x1)	GeomOpt	-99.23
(2x2x2)	GeomOpt	-98.20
(3x3x3)	GeomOpt	-98.12

with bigger k-point sets give slightly weaker adsorption. The variations were within 1 kJ/mol, which

is a very small difference and less than other sources of error already determined such as for instance the periodicity of methanol. Only the Γ-point (the origin in reciprocal space) was used in further calculations. Thus adsorption of methanol on the acid sites of H-SAPO-34 and H-SSZ-13 were performed with one unit cell and one k-point.

8.2.2 Results and discussion

Different adsorption geometries and energies were obtained on the four acid sites for H-SSZ-13, while only one adsorption geometry per site was investigated for H-SAPO-34. Several adsorption angles were tried on H-SSZ-13 and showed that it was difficult to determine which was the most stable, as it was easy to find different stable adsorption geometries (Figure 8.7).

Figure 8.4 shows the placement of methanol in the SSZ-O1 (2). Three different representations are chosen, inside the unit cell, and inside the cage from two angles. The figure shows that the ring in one unit cell corresponds to the ring that is like a ”belt” around the cage (12-ring) and not the rings that connect the cages (8-rings). Other methanol geometries are only shown in the unit cell.

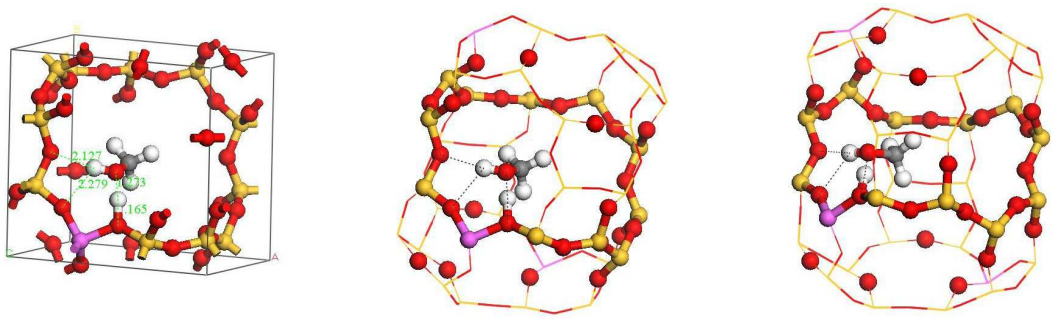

(a) **(b)** **(c)**

Figure 8.4: Placement of methanol in the unit cell (a) and the cage (b and c) for the H-CHA-1(2) calculation. Figure (b) is the cage oriented as the unit cell in (a), while (c) shows a better view of the cage.

Shah et al. reported periodic DFT calculations for the adsorption of methanol in H-SSZ-13 and H-SAPO-34, and they found adsorption within the 8-ring of the framework to be most stable (Fig. 8.5)

The geometry in Fig. 8.5 shows that methanol is adsorbed so that O and H from methanol, together with framework Al, H and two O’s, form a 6-ring. It is not very well defined which hydrogen belongs

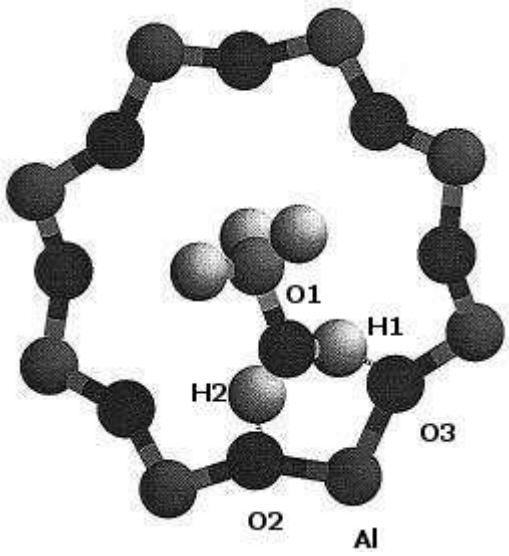

O1-H1 (Å)	1.04
O1-H2 (Å)	1.06
O3-H1 (Å)	1.54
O2-H2 (Å)	1.43
∠H2-O1-H1 (°)	95
C-O1 (Å)	1.45
Al-O2 (Å)	1.71
Al-O3 (Å)	1.70

Figure 8.5: The most stable adsorption configuration found by Shah et al. Methanol lies in an 8-ring of the chabazite structure [61]. Bond lengths and angles are given in Å and °.

to methanol, but the bond lengths indicate that one hydrogen (H2) is slightly closer to the framework while the other (H1) is slightly closer to the methanol.

In the present calculations methanol positioned within the 8-ring of the structure was not obtained. In all cases, parts of, or the whole molecule prefered to move into the cage (Fig. 8.6).

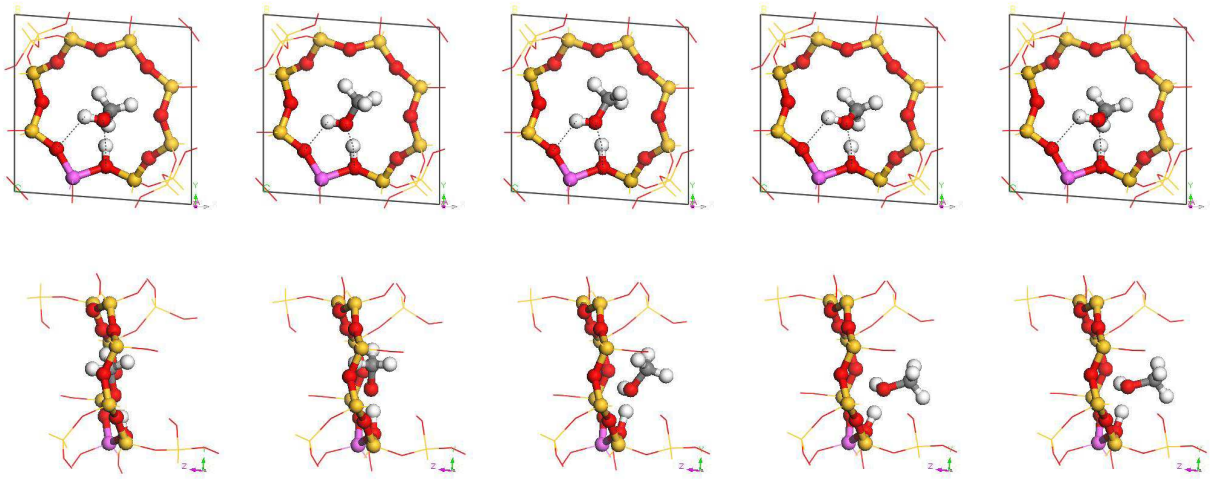

Figure 8.6: Methanol moved away from the ring in all calculations where it was initially placed in an 8-ring of the framework. When looking directly at the ring this cannot be seen, but along the cage this is clear. Since the 8-ring windows connect the cages, this means that the methanol preferentially points into the cage. This example is the CHA-1 (5) calculation. It converged in 30 iterations, and from left to right the figures show the geometry after 1, 13, 17, 24 and 30 iterations.

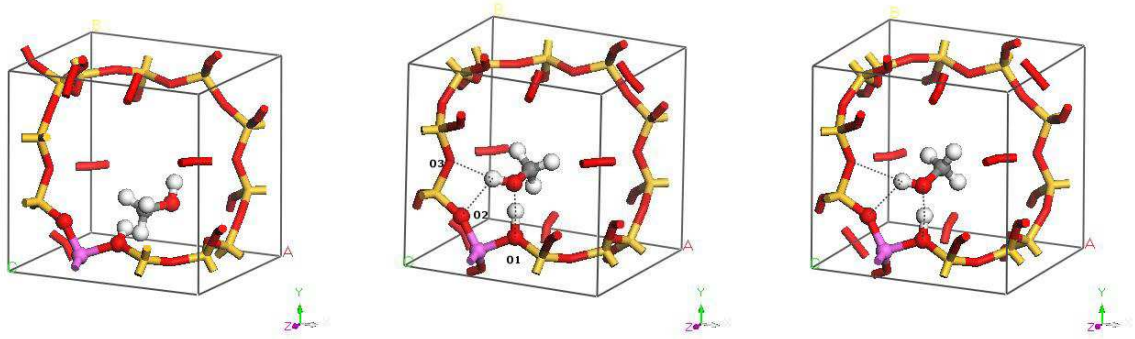

(a) SSZ_O1
$E_{ads} = -14.9\ kJ/mol$

(b) SSZ_O1 (2)
$E_{ads} = -96.4\ kJ/mol$

(c) SSZ_O1 (3)
$E_{ads} = -89.3\ kJ/mol$

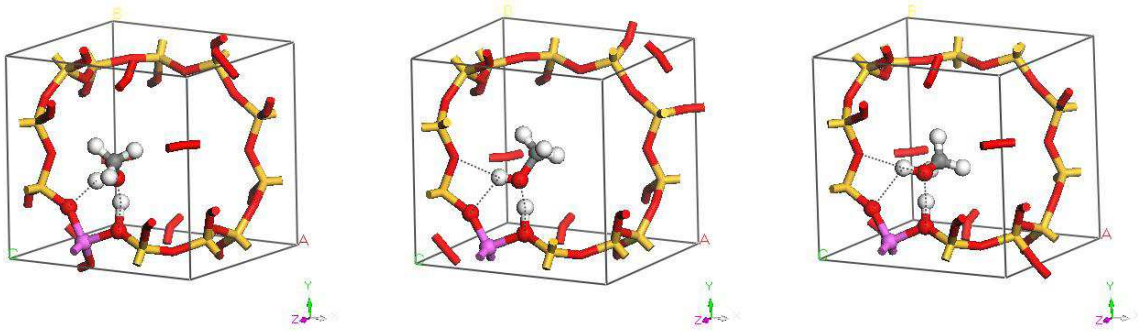

(d) SSZ_O1 (4)
$E_{ads} = -94.4\ kJ/mol$

(e) SSZ_O1 (5)
$E_{ads} = -95.9\ kJ/mol$

(f) SSZ_O1 (6)
$E_{ads} = -99.2\ kJ/mol$

Figure 8.7: The different adsorption geometries obtained with methanol on H-SSZ-13 with proton adsorbed on O1.

Six different adsorption geometries for methanol on the O1 site of H-SSZ-13 were obtained (Fig.8.7). Geometry (a) was not adsorbed on the acid site, and methanol was positioned further into the cage. This geometry also had a very ewak adsorption energy. The other five structures had the oxygen from methanol clearly coordinated to the framework hydrogen. The O-H hydrogen in methanol did not form a clear bond to the O2 framework oxygen connected to Al. The hydrogen was almost equally distanced from O2 and O3 further out in the ring, and even closer to O3 in the most stable geometry (number 6) as seen in Table 8.3. In all cases methanol points into the cage, except for geometry number 4. In this case the CH_3-group points into the ring, while the OH-group points into the cage together with the framework hydrogen. The bond lengths for the different geometries are reported in Table 8.3 and show that especially the bonds between the different oxygens and hydrogens are quite similar for all geometries.

Table 8.3: Bond lengths and angles for methanol adsorbed in various ways on O1 in H-SSZ-13. The number in parenthesis corresponds to the numbering in Fig. 8.7. Structure one is not included since this was not an adsorption on the acid site.

	(2)	(3)	(4)	(5)	(6)	Average
O_{MeOH}-H_{MeOH} (Å)	0.986	0.980	1.003	0.981	0.984	0.986±0.009
O_{MeOH}-H_{acid} (Å)	1.273	1.368	1.134	1.255	1.339	1.27±0.09
O1-H_{acid} (Å)	1.165	1.101	1.313	1.184	1.125	1.17±0.08
O2-H_{MeOH} (Å)	2.279	2.246	1.775	2.086	2.376	2.2±0.2
O1-H_{acid} (Å)	2.127	2.500	2.446	2.213	2.21	2.3±0.1
O1-Al-O2 (°)	97.4	99.6	99.3	99.9	97.8	98.8±1.1
H_{MeOH}-O_{MeOH}-H_{acid} (°)	105.3	103.8	96.9	110.6	106.6	104.6±5.0

Also two different geometries for the adsorption of methanol on H-SSZ-13 in the O2 position were tried (Fig. 8.8). In this case methanol had a very strong affinity for both protons. In Figure 8.8(b) this is clearly shown with the left hydrogen, which was originally on the framework. Also, the O-H bond length in methanol increased and the methanol proton moved towards the O1 framework oxygen. The resulting geometry can thus be considered as an adsorption of methanol on the O1 site. The other adsorption on the O2 site was tried across the Si atom and not aluminum. This methanol proton does not form a bond to a framework oxygen in this case.

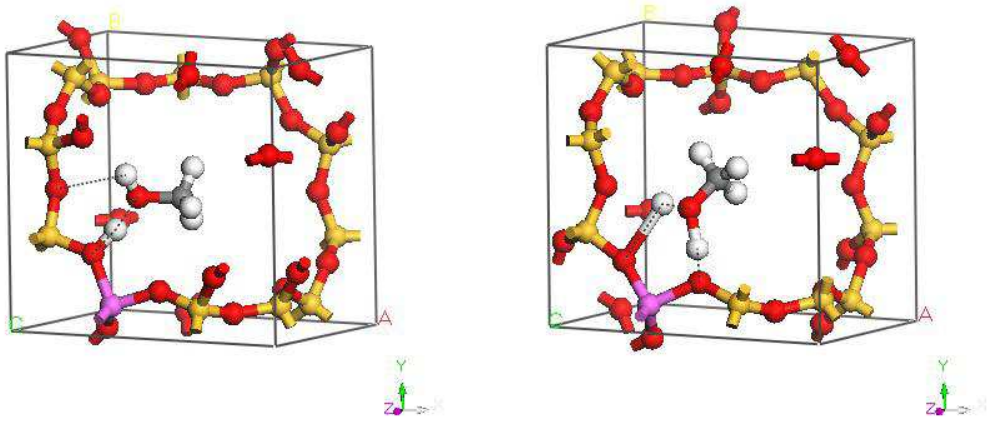

(a) SSZ_O1
$E_{ads} = -80.6\ kJ/mol$

(b) SSZ_O2 (2)
$E_{ads} = -95.6\ kJ/mol$

Figure 8.8: The different adsorption geometries obtained with methanol on H-SSZ-13 with proton adsorbed on O2.

Figure 8.9 shows two adsorptions of methanol on the O3 site in H-SSZ-13 and on the O4 site. In

these cases it is even more evident that the 6-ring geometries reported by Shah et al. have not been observed in the present calculations, but rather an 8.ring geometry. This ring consists of O-H from methanol and H, Al, Si and 3 O from the framework.

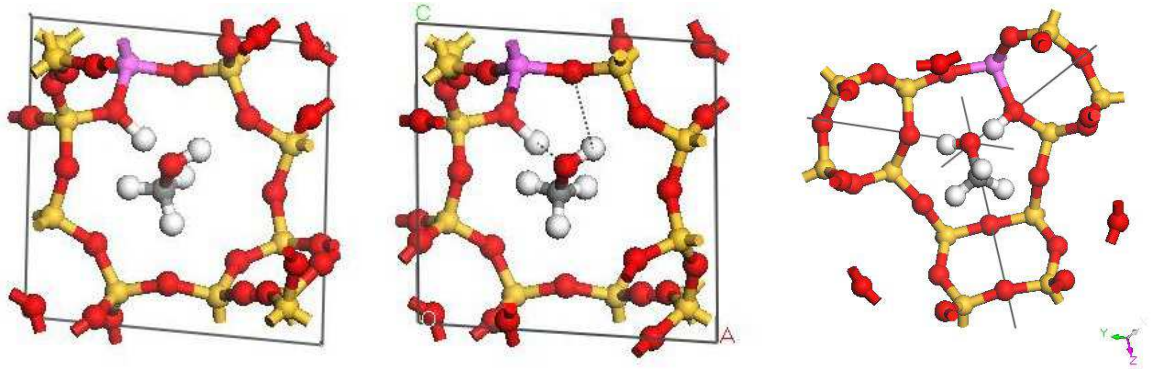

(a) SSZ_O3
$E_{ads} = -92.5\ kJ/mol$

(b) SSZ_O3 (2)
$E_{ads} = -91.6\ kJ/mol$

(c) SSZ_O4
$E_{ads} = -90.0\ kJ/mol$

Figure 8.9: The different adsorption geometries obtained with methanol on H-SSZ-13 with proton adsorbed on O3 and one geometry on O4. It is important to remember that methanol does not lie in the ring in any of the structure but it points into the cage

The major difference between these calculations and those reported by Shah et al. is that the same geometries within the 8-ring were not found. A possible reason for this is the use of different chabazite starting structures.

One methanol adsorption geometry for each acid site in H-SAPO-34 was chosen for comparison with H-SSZ-13. Figure 8.10 shows the resulting geometries and the adsorption energies.

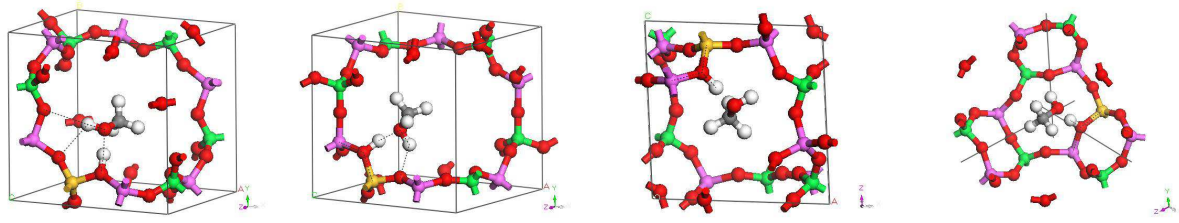

(a) SAPO_O1
$E_{ads} = -90.1\ kJ/mol$

(b) SAPO_O2
$E_{ads} = -66.8\ kJ/mol$

(c) SAPO_O3
$E_{ads} = -87.9\ kJ/mol$

(d) SAPO_O4
$E_{ads} = -91.6\ kJ/mol$

Figure 8.10: The adsorption geometries obtained with methanol on H-SAPO-34 for all four acid sites.

The adsorption energies on the four acid sites for both materials are given in Table 8.4. All the stable adsorption geometries found in H-SSZ-13 are reported, and the four H-SAPO-34 calculations are

reported on the same line as the corresponding adsorption geometry in H-SSZ-13. For methanol adsorbed on the O1 position the adsorption energies varied by 10 kJ/mol, while for O2 it was 15 kJ/mol. The first calculation reported is then not taken into account, as this was done with methanol far away from the adsorption site, and hence had a very small adsorption energy. The two O3 calculations are very similar. The most stable adsorption geometry found by Shah et al. had an adsorption energy of 82 kJ/mol, which is around 10 kJ/mol lower than most of adsorption energies found in this work. One configuration was tried with methanol far away from the acid site, which gave an adsorption energy of only 14 kJ/mol, which clearly shows how the acid sites stabilized adsorption. As previously stated, the present results are very different from those of Shah et al. with respect to the position of the methanol molecule. Shah et al. found methanol inside the 8-ring, while methanol is in these results pointing into the cage. Even though the methanol moved into the cage, it stayed adsorbed on the Brønsted site, with adsorption energies between 80 and 100 kJ/mol.

Table 8.4: Adsorption energies for methanol on the four different sites of H-SSZ-13 and H-SAPO-34. In SSZ-OX and SAPO-OY does X and Y denote the oxygen site on which H is bonded. Several geometries for H-SSZ-13 were tried, and these are numbered by the number in parenthesis. H-SAPO-34 and H-SSZ-13 on the same row have methanol equally positioned in the unit cell.

material and position	E_{ads} (kJ/mol)	material and position	E_{ads} (kJ/mol)
SSZ-O1	-14.9		
SSZ-O1 (2)	-96.4	SAPO.O1	-90.1
SSZ-O1 (3)	-89.3		
SSZ-O1 (4)	-94.4		
SSZ-O1 (5)	-95.9		
SSZ-O1 (6)	-99.2		
SSZ-O2	-80.6		
SSZ-O2 (2)	-95.6	SAPO-O2	-66.8
SSZ-O3	-92.5		
SSZ-O3 (2)	-91.6	SAPO-O3	-87.9
SSZ-O4 (2)	-90.0	SAPO-O4	-91.6

The adsorption energies on H-SAPO-34 were generally lower than for H-SSZ-13. The biggest difference was found on O2 where the adsorption was 30 kJ/mol weaker in H-SAPO-34. On O2 and O3 the difference was around 4 kJ/mol while on O4 the adsorption was 2 kJ/mol stronger on H-SAPO-34. The results indicate that methanol interacts more weakly on H-SAPO-34, but not necessarily by very much. More adsorption geometries should be investigated on both structures in order to gain a better understanding of this.

8.3 CO-adsorption

8.3.1 Choice of setup

For the adsorption of CO, the same computational setup was used as for the adsorption of methanol, but with the RPBE functional. RPBE was chosen as functional becasue it has been shown that RPBE is a better functional than PBE for spectroscopic studies of the adsorption of CO on mordenite [62]. As in the adsorption of methanol, periodic CO was used as reference, although the difference between one gaseous molecule and periodic CO with an infinitely large unit cell was only 0.2 kJ/mol.

The frequencies are calculated within the harmonic approximation. The choice of atoms involved in construction of the Hessian matrix decides which atoms are moved for calculating bond forces and stretching frequencies. In the present calculations the C-O and O-H stretch frequencies were of major interest, as the lattice is assumed to be quite stiff. It might therefore not be necessary to compute frequencies with all atoms included in the Hessian, but restrain the calculation to only the atoms involved. Three different calculations were performed for comparison, and the results where identical. This showed that it is safe to employ only the smallest set of atoms in the frequency calculations.

CO was adsorbed on the acid site of H-SAPO-34 and H-SSZ-13 through the carbon end. Adsorption through the oxygen end was tried, but the adsorption was much less stable the adsorption through the carbon end.

8.3.2 Relevant experimental results from literature

Bordiga et al. investigated the relative acidities of H-SAPO-34 and H-SSZ-13 by monitoring the adsorption of CO with IR spectroscopy [8]. The experimental results, to which the present calculations are compared, are listed in table 8.5.

Upon adsorption of CO in H-SSZ-13 the high frequency (HF) Brønsted acid O-H peak shifted from 3616 cm^{-1} to 3300 cm^{-1}. The low frequency (LF) Brønsted acid peak at 3584 was shifted to the same

Table 8.5: Experimental values for the adsorption of CO on H-SAPO-34 and H-SSZ-13 from[8]. Only the values related to the Brønsted sites are reported. High frequency (HF) and low frequency (LF) refer to the bands in the untreated sample.

Species	CO vib (cm^{-1})	OH stretch (cm^{-1})	CO shift (cm^{-1})	OH shift(cm^{-1})
Liquid-like CO	2138			
H-SSZ-13		3616 (HF) 3584 (LF)		
H-SAPO-34		3627 (HF) 3603 (LF)		
H-SSZ-13–CO	2177	3300	38	-316 (HF)
H-SAPO-34–CO	2173	3357 (HF) 3340 (LF)	35	-270 (HF) -263 (LF)

value, which means that they found the presence of only one red-shifted component. This suggests that the two families of Brønsted sites are equivalent. It is possible to differentiate between the two families of Brønsted sites only when CO is not adsorbed on the protons. In H-SAPO-34 the HF and LF bands were shifted to different values, which suggests a lower acidic character of the sites with the LF component.

It should be noted that the difference between the HF and LF bands for H-SSZ-13 and H-SAPO-34 is only 32 and 24 cm^{-1}, respectively. Although Bordiga et al. found that both bands have the same acidity towards CO, the LF site starts to interact with CO only at higher pressures. This is consistent with one acid site being exposed to only one cage, while the three other acid cites are exposed to two cages and therefore require a lower CO pressure for interaction with the base.

8.3.3 Results of calculations and discussion

Table 8.6 shows adsorption angles, bond lengths and energies for the adsorption of CO on the different acid sites for both H-SAPO-34 and H-SSZ-13. Different adsorption geometries on each site were not found. CO was bent from the O-H line by between 2 and 8° (Table 8.6). For both materials the adsorbed CO was least bent in the O4 position. H-SAPO-34 was most bent in the O3 position while for H-SSZ-13 CO in the O2 and O3 positions were equally bent. The bending was strongest in H-SAPO-34 except for in the O4 position.

The OH-CO angle reported in the above table is the angle between the lines formed by the OH atoms and the CO atoms, and is calculated as follows. $\vec{a}$ and $\vec{b}$ are the vectors corresponding to the bonding

Table 8.6: Adsorption energies and geometries calculated for adsorption of CO on the acid site of H-SSZ-13 and H-SAPO-34. Calculations performed with RPBE functional.

Topological site	O-H bond-length (Å) H-SSZ-13	H-SAPO-34			
O1	0.976	0.974			
O2	0.978	0.975			
O3	0.976	0.975			
O4	0.977	0.976			
Free CO	1.147				
H-SSZ-13–CO	Bond length (Å)			∠ OH-CO	Adsorption energy
Position of H	C-O	H-C	O-H	(°)	(kJ/mol)
O1	1.138	1.991	0.995	2.9	-28.3
O2	1.140	2.027	0.995	5.8	-23.3
O3	1.139	1.930	0.996	5.4	-22.6
O4	1.140	2.069	0.992	2.5	-25.4
H-SAPO-34–CO	Bond length (Å)			∠ OH-CO	Adsorption energy
Position of H	C-O	H-C	O-H	(°)	(kJ/mol)
O1	1.139	2.024	0.989	4.3	-25.9
O2	1.141	2.06	0.990	4.3	-20.8
O3	1.140	2.083	0.990	8.4	-4.9
O4	1.141	2.092	0.989	1.7	-24.8

lines.

$$\vec{a} \cdot \vec{b} = |a|\,|b| \cos\theta_{ab} \tag{8.1}$$

gives

$$\theta_{ab} = \frac{\vec{a} \cdot \vec{b}}{|a|\,|b|} \tag{8.2}$$

Upon adsorption, the CO bond-length decreases compared to gaseous CO. The decrease is of only between 0.006 and 0.009 Å, and the adsorbed CO in H-SAPO-34 is consistently 0.001 Å longer than in H-SSZ-13. It is also 0.001 Å less in H-SAPO-34 compared to H-SSZ-13, but this difference is too small to be significant. Correspondingly the O-H bond-length in H-SSZ-13 increases by 0.018(±2) Å in H-SSZ-13 and 0.015(±1) Å in H-SAPO-34. There are only small variations for the different topological sites, as seen by the standard deviation given in parenthesis.

Also the different acid sites gave different energies of adsorption. Although the differences in adsorp-

tion energies were quite small, the O3 position had the lowest adsorption energy for both structures, so that the most bending corresponds to the lowest stabilization. The adsorption energies where lower for H-SAPO-34 on all four positions, but the difference was generally only between 1 and 3 kJ/mol. The exception to this is the O3 position. The adsorption on O3 in H-SAPO-34 was very little stable with an adsorption energy of 4 kJ/mol. This corresponds with the biggest angle between the CO and OH lines.

Table 8.7 gives the calculated O-H stretch frequencies of H-SSZ-13 and H-SAPO-34 with and without CO adsorbed on the Brønsted site. The frequency of free CO was 2076 cm^{-1} which is quite distant from the experimental 2138 cm^{-1} considering that the shifts are around 30 cm^{-1}. It also differs from the value of Bučko et al. of 2118 cm^{-1}, who also used the RPBE functional but with plane-wave basis set instead of atom-centered basis functions [62]. Their value is reported for the free CO molecule and not in a periodic structure. This good agreement between experiment and computational work was not reproduced here. The CO frequency of the free molecule is even lower in the present calculations, only 2064 cm^{-1}. When increasing the unit cell no difference in frequency was found, and also the C-O bond length was alway the same 1.147 Å (Bučko obtained 1.149 Å). It should be noted however, that CO easily gave different frequencies (variation of 5 cm^{-1}) when the geometry optimization was started with different C-O lengths, even though they always converged to the same 1.147 Å. This could be due to the length of the step that DMol^3 uses for calculating the fitted parabola for the frequencies. The harmonic frequencies were computed with finite differences of 0.010 Bohr = 0.0053 Å, which is default in DMol^3. This is not easily manipulated in the MaterialStudio interface and there was not time to investigate further into this.

Table 8.7: Calculated O-H and C-O frequencies for with and without adsorbed CO on H-SSZ-13 and H-SAPO-34. Frequencies are given in cm^{-1}.

Position of Brønsted site	O-H frequency		Shifted O-H frequency		C-O frequency	
	H-SSZ-13	H-SAPO-34	H-SSZ-13	H-SAPO-34	H-SSZ-13	H-SAPO-34
Free CO	-	-	-	-	2076	
O1	3689	3720	3290	3394	2195	2192
O2	3665	3703	3316	3389	2180	2177
O3	3686	3701	3274	3408	2186	2186
O4	3686	3696	3370	3410	2178	2177

Table 8.7 also gives the calculated O-H and C-O frequencies with adsorption of CO on the four different Brønsted acid sites of H-SSZ-13 and H-SAPO-34. The O-H frequency is the frequency without C-O adsorbed, and for both materials these frequencies are divided into two distinct groups. In H-SSZ-13 the O-H frequencies on O1, O3 and O4 range from 3686 to 3689 cm^{-1}, while O2 gives 3665 cm^{-1} which is around 20 cm^{-1} lower. Similarly, in H-SAPO-34 the O2-H frequency is lowest, with a gap of 16 cm^{-1} from highest (O1) to lowest frequency. However O3 and O4 are evenly distributed within this gap, and it is not so straight forward to group O1, O3 and O4 together. Bordiga et al. identified two O-H peaks in the IR spectra, differing of 32 cm^{-1}. That two distinct groups are less obvious in the calculations of H-SAPO-34 correspond to experiment which show that the two peaks are closer for H-SAPO-34 (24 cm^{-1}).

Table 8.8: Calculated frequency shift for O-H and C-O upon adsorption of CO on the Brønsted site of H-SSZ-13 and H-SAPO-34. Frequency shifts are given in cm^{-1}.

Position of	O-H frequency shift		C-O frequency shift	
Brønsted site	H-SSZ-13	H-SAPO-34	H-SSZ-13	H-SAPO-34
O1	-399	-326	119	116
O2	-349	-314	104	101
O3	-412	-293	110	110
O4	-316	-286	102	101
Experiment	-316	-270/-263	38	35

The calculated frequency shifts for CO given in Table 8.8 are larger than observed by experiment. The CO shift is from 50 to 80 cm^{-1} too large, while instead the OH shift varies from 90 cm^{-1} to 100 cm^{-1} higher than expected. However the trends are still accounted for. A smaller CO shift in both experiment and calculations for H-SAPO-34 indicates CO interacts less with the Brønsted site in this material. Likewise a smaller shift in the O-H stretch indicates the same effect.

Note that the frequencies are calculated within the harmonic approximation, which in general overestimates the frequency. Shah et al. estimated the anharmonic effect to reduce the frequencies of their calculations with 200 cm^{-1}. Looking at the O-H frequencies, it is correct that the frequencies are overestimated, but only by about 50-100 cm^{-1} if we compare to the experimental values.

The above results indicate that H-SAPO-34 is a weaker acid than H-SSZ-13 in accordance with

the results from Bordiga et al. However, the differences between the two materials is not large. That H-SAPO-34 is less acidic was experimentally concluded in another work by the same group by adsorbing hydrogen at low temperatures [9]. DFT analysis adsorbing hydrogen is not possible since contemporary density functionals do not model dispersion forces, as another method is required for such a study.

Appendix A

Calculations

A.1 Calculation of feed

In this thesis a saturation evaporator has been used to ensure the right feed of methanol to the catalyst in the reactor. Helium gas has been bubbled through the saturation evaporator which was held in a temperate water bath. In the experiments the water bath was 20°C which gives a vapour pressure of 12.99 kPa, calculated by using the Clausius Clapeyron equation

$$ln\frac{p}{p*} = \frac{\Delta_{vap}H}{R}(\frac{1}{T} - \frac{1}{T*}) \tag{A.1}$$

and data from the NIST Standard Reference Database85.

The total flow of gas was 35 mL/min, which gives a methanol flow of

$$35\text{mL /min} \cdot \frac{12.99\text{kPA}}{101.325\text{kPa}} = 4.49\text{mL/min} \tag{A.2}$$

By use of the ideal gas equation

$$\text{PV} = \text{nRT} \tag{A.3}$$

the mass of the catalyst passing over the catalyst per minute is calculated: 6.0 g MeOH/min.

Weight Hourly Space Velocity (WHSV) is a measure of how much methanol has passed over the catalyst per unit time

$$\text{WHSV} = \frac{\text{mass methanol}}{\text{mass catalyst} \cdot \text{hour}} \tag{A.4}$$

With 60 mg catalyst WHSV is 6.0 hr^{-2}.

A.2 Effluent analyses with GC

The effluent was analyzed by Gas Chromatography and Mass Spectrometry.

The Flame Ionization Detector (FID) was assumed to have the same response for all non-oxygenate hydrocarbons. The hydrocarbon response factor was set to 1 and the response factors for MeOH and DME were calibrated to 0.766 and 0.598, respectively. This means that the corrected area for methanol was

$$\text{Area}_{\text{corr}}(MeOH) = \frac{\text{Area}(MeOH)}{0.766}, \tag{A.5}$$

while for DME

$$\text{Area}_{\text{corr}}(DME) = \frac{\text{Area}(DME)}{0.598} \tag{A.6}$$

The corrected areas are thus proportional to the concentration of each product. It is important to remember that the FID signal is (almost) proportional to the concentration of carbon-atoms, not number of molecules. This means that the same concentration of butane and methane will give a butane peak which is four times as big as the methane peak.

The conversion was calculated as:

$$\text{conversion} = \frac{\sum_{\text{all compounds}} \text{Area}_{\text{corr}} - \text{Area}_{\text{corr}}(MeOH) - \text{Area}_{\text{corr}}(DME)}{\sum_{\text{all compounds}} \text{Area}_{\text{corr}}} \cdot 100\% \tag{A.7}$$

This assumes that no carbon atoms are left in the catalyst (i.e. no coke or hydrocarbon pool formation).

The product selectivity (PS) for product i is calculated as

$$PS_i = \frac{\text{Area}_i}{\sum_{\text{products}} \text{Area}_j} \cdot 100\% \tag{A.8}$$

This means that the product selectivity is based on carbon atom count. If the product selectivity for methane and butane is the same, the number of butane molecules is 1/4 the number of methane molecules.

The C_2/C_3 and C_2/C_4 ratios are then given as the ratios of the selectivities.

A.3 Effluent analysis with MS

Since the MS samples much quicker than the GC, the effluent was analyzed with both instruments. This enables monitoring of the effluent between the GC-analyses that were taken at 20 minute intervals. The mass spectrometer was calibrated to the GC.

Conversion from the Mass Spectrometer is calculated somewhat differently as

$$\text{Conversion} = \frac{n_{MeOH,in} - "n_{MeOH,out}"}{n_{MeOH,in}} = C_{MeOH,in} \cdot V_{in} - "C_{MeOH,out}" \cdot V_{out} C_{MeOH,in} \cdot C_{in} \quad (A.9)$$

Helium is the carrier gas and is not converted in the reactor, so that $n_{He,in} = n_{He,out}$ and thus $C_{He,inn} \cdot V_{in} = C_{He,out} \cdot V_{out}$. Rearranging this equation and inserting it into equation A.9 gives

$$\text{conversion} = \frac{\frac{C_{MeOH,in}}{C_{He,in}} - \frac{"C_{MeOH,out}"}{C_{He,out}}}{\frac{C_{MeOH,in}}{C_{He,out}}} \quad (A.10)$$

Methanol coming out is put in quotation marks to indicate that both DME and methanol are considered reactants, $"C_{MeOH,out}" = C_{MeOH,out} + C_{DME,out}$, where concentration is defined as concentration of carbon atoms from the specified compound.

The number of counts, T, in the MS is proportional to the concentration

$$C_x = T_x \cdot k_x \quad (A.11)$$

which gives the final equation for calculating conversion

$$\frac{\frac{T_{MeOH,in}}{T_{He,in}} - \frac{T_{MeOH,out} + T_{DME,out} \cdot \frac{k_{DME}}{k_{MeOH}}}{T_{He,out}}}{\frac{T_{MeOH,in}}{T_{He,in}}} \quad (A.12)$$

Equation A.11 enables calibration of the MS by using concentration ratios from the GC

$$\frac{k_{DME}}{k_{MeOH}} = \frac{C_{DME} \cdot T_{MeOH}}{C_{MeOH} \cdot T_{DME}} \quad (A.13)$$

The methanol going in is analysed through an empty reactor after each analysis. This means that when hydrocarbons are deposited on the catalyst (coke formation and build-up of hydrocarbon pool) the conversion calculated from the MS should be higher than for the GC. This however depends on the GC point chosen to calibrate the MS signal, which should be best after deactivation of the catalyst

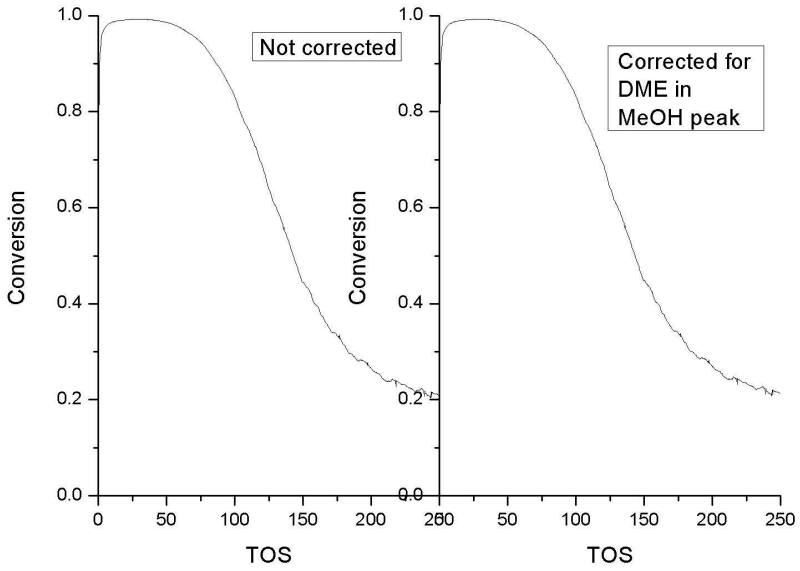

Figure A.1: Conversion of methanol over H-SSZ-13 at 350 degree calculated from MS data. To left without taking into account the contribution from DME in the 31 peak, and to the right with correction. There is no visible difference.

due to the fact that there is still conversion to DME when hydrocarbon products are no longer present in the effluent stream.

The 31 peak was taken as the methanol signal while 46 was used for DME. DME can defragmented into a 31-ion and according to the NIST database this 31/46 ratio is 34/607 = 0.092. This means that the 31-peak is a superposition of the 31 signal from methanol and that from DME. This gives that the actual methanol signal, T, is

$$T_{31}(\text{MeOH}) = T_{31} - T_{31}(\text{DME}) \qquad = T_{31} - 0.056013T_{46}(\text{DME}) \tag{A.14}$$

This difference is too small to have any effect on the calculations for the conversion as seen in figure A.1

A.4 Equilibration of methanol and dimethyl ether

Methanol is condensed to dimethyl ether in the catalyst and both these oxygenates may take part in the reaction. The condensation reaction is $2\,CH_3OH \longrightarrow CH_3OCH_3 + H_2O$.

From the relations

$$\ln K_p = -\frac{\Delta G^\circ}{R \cdot T} \tag{A.15}$$

and

$$K_p = \frac{p_{\mathrm{DME}} \cdot p_{\mathrm{H_2O}}}{p^2_{\mathrm{MeOH}}} \tag{A.16}$$

it is possible to find the MeOH/DME ratio at equilibrium (Table A.1).

Table A.1: Equilibrium ratios for methanol and DME at 1 atm and relevant temperatures, when pressure of methanol in feed is 13 kPa (20°C)

Temperature (K)	$\frac{P_{MeOH}}{P_{DME}}$
298	8.21^3
300	8.72^3
400	8.34^2
500	2.91^1
600	5.87^1

Appendix B

List of catalytic tests presented in this thesis

Table B.1: List of Catalytic tests presented in this thesis

	Catalyst (batch)	Mass of catalyst	WHSV (hr^{-1})	Time of Quench	Temperature (° C)
Stability tests	H-SAPO-34 (ABA217)	100 mg	6.0	5 hours	300, 350, 400, 450
	H-SSZ-13 (KP)	100 mg	6.0	5 hours	400
Short TOS	H-SAPO-34 (ABA217)	60 mg	6.0	5, 10, 15, 20 , 25 min	300, 325, 350, 375, 400
	H-SSZ-13 (CHA07)	60 mg	6.0	+ one test until deactivation	300, 325, 350, 375, 400
Varying WHSV	H-SAPO-45 (ABA217)	30 mg	12.0	one test until deactivation	350, 375, 400, 425, 450, 475
	Temperature(°C)	Catalysts (batch)	WHSV (hr^{-1})	Time of feed	Minutes of flushing
Flushing experiments	300	H-SSZ-13 (CHA09)	6.0	15 min	0, 5, 15, 30, 60
	350	H-SSZ-13 (CHA09)	6.0	20 min	0, 5, 60
	350	H-SAPO-34 (MHN06)	6.0	20 min	0, 1, 2, 5, 60

Glossary

BEA The structure of zeolite beta.

CHA The chabazite zeolite structure.

DFT Density Functional Theory.

DMol^3 Program used for density functional theory calculations.

GGA Generalized Gradient corrected Approximation for the exchange functional in DFT.

H-SAPO-34 SAPO-34 on protonated form.

H-SSZ-13 SSZ-13 on protonated form.

LDA Local Density Approximation for the exchange functional in DFT.

MFI The structure of ZSM-5: Mobile FIve.

MOGD Methanol-To-Gasoline-and-Distillates.

MTH Methanol-To-Hydrocarbons.

MTO Methanol-To-Olefins.

MTP Methanol-To-Propylene.

PBCs Periodic Boundary Conditions.

PBE Exchange functional used in DFT with correlation from Perdew-Burke-Ernzerhof.

RPBE Exchange functional used in DFT - Revised PBE.

SAPO-34 SilicoAluminumPhOsphate-34 a zeotype material with the chabazite (CHA) structure.

TIGAS Haldor Topsøe's Integrated Gasoline Synthesis.

TOS Time On Stream.

WHSV Weight hourly space velocity.

ZSM-5 Zeolite Socony Mobil - Five.

Abbreviations for chemical compounds

CPD Cyclopentadiene.

DME Dimethyl ether.

HeptaMB$^+$ Heptamethylbenzenium ion.

HMB Hexamethylbenzene.

MeOH Methanol.

pentaMB Pentamethylbenzene.

TetraMB Tetramethylbenzene.

TriMB Trimethylbenzene.

References

[1] Chorkendorff, I.; Niemantsvedriet, J. W. *Concepts of Modern Catalysis and Kinetics*; WILEY-VCH GmbH & Co. KGaA, 2003.

[2] Haw, J. F. *Phys. Chem. Chem. Phys.* **2002**, *4*, 5431–5441.

[3] *Introduction to zeolite science and practice*, 2nd ed.; van Bekkum, H., Flanigen, E., Jacobs, P., Jansen, J., Eds.; Elsevier, 2001.

[4] Barrer, R. M. *J. Soc. Chem. Ind.* **1945**, *64*, 130–135.

[5] Barrer, R. M. *J. Chem. Soc.* **1948**, 2158–2163.

[6] Barrer, R. M. *J. Chem. Soc.* **1948**, 127–132.

[7] Baerlocher, C.; McCusker, L. B.; Olson, D. H. *Atlas of zeolite framework types*; Elsevier, 2007.

[8] Bordiga, S.; Regli, L.; Cocina, D.; Lamberti, C.; Bjørgen, M.; Lillerud, K. P. *J. Phys. Chem. B* **2005**, *109*, 2779–2784.

[9] Bordiga, S.; Regli, L.; Lamberti, C.; Zecchina, A.; Bjørgen, M.; Lillerud, K. P. *J. Phys. Chem. B* **2005**, *109*, 7724–7732.

[10] Haw, J. F.; Song, W.; Marcus, D. M.; Nicholas, J. B. *Acc. Chem. Res.* **2003**, *36*, 317–326.

[11] Chang, C. D.; Silvestri, A. J. *J. Catal.* **1977**, *47*, 249–259.

[12] Haw, J. F.; Marcus, D. M. *Topics in Catalysis* **2005**, *34*, 41–48.

[13] Stöcker, M. *Microporous Mesoporous Mater.* **1999**, *29*, 3–48.

[14] Hutchings, G. J.; Watson, G. W.; Willock, D. J. *Microporous Mesoporous Mater.* **1999**, *29*, 67–77.

[15] Dahl, I. M.; Kolboe, S. *J. Catal.* **1994**, *149*, 458–464.

[16] Dahl, I. M.; Kolboe, S. *J. Catal.* **1996**, *161*, 304–309.

[17] Goguen, P. W.; Xu, T.; Barich, D. H.; Skloss, T. W.; Song, W.; Wang, Z.; Nicholas, J. B.; Haw, J. F. *J. Am. Chem. Soc.* **1998**, *120*, 2650–2651.

[18] Mikkelsen, O.; Rønning, P. O.; Kolboe, S. *Microporous Mesoporous Mater.* **2000**, *40*, 95–113.

[19] Haw, J. F.; Nicholas, J. B.; Song, W.; Deng, F.; Wang, Z.; Xu, T.; Heneghan, C. S. *J. Am. Chem. Soc.* **2000**, *122*, 4763–4775.

[20] Svelle, S.; Rønning, P. O.; Olsbye, U.; Kolboe, S. *J. Catal.* **2005**, *234*, 385–400.

[21] Kolboe, S. *Applied Catalysis A* **1986**, *A 40*, 711–713.

[22] Mole, T.; Whiteside, J. A.; Seddon, D. *J. Catal.* **1983**, *82*, 261–266.

[23] Mole, T.; Bett, G.; Seddon, D. *J. Catal.* **1983**, *84*, 435–445.

[24] Arstad, B.; Kolboe, S. *J. Am. Chem. Soc.* **2001**, *123*, 8137–8138.

[25] Arstad, B.; Kolboe, S. *Catal. Lett.* **2001**, *71*, 209–212.

[26] Bjørgen, M.; Olsbye, U.; Svelle, S.; Kolboe, S. *Catal. Lett.* **2004**, *93*, 37–40.

[27] Arstad, B.; Kolboe, S.; Swang, O. *J. Phys. Chem. A* **2005**, *109*, 8914–8922.

[28] Arstad, B.; Kolboe, S.; Swang, O. *J. Phys. Org. Chem.* **2006**, *19*, 81–92.

[29] Arstad, B.; Nicholas, J. B.; Haw, J. F. *J. Am. Chem. Soc.* **2004**, *126*, 2991–3001.

[30] Svelle, S.; Rønning, P. O.; Kolboe, S. *J. Catal.* **2004**, *224*, 115–123.

[31] Svelle, S.; Joensen, F.; Nerlov, J.; Olsbye, U.; Lillerud, K.-P.; Kolboe, S.; rgen, M. B. *J. Am. Chem. Soc.* **2006**, *128*, 14770–14771.

[32] Bjørgen, M.; Svelle, S.; Joensen, F.; Nerlov, J.; Kolboe, S.; Bonino, F.; Palumbo, L.; Bordiga, S.; Olsbye, U. *J. Catal.* **2007**, *249*, 195–207.

[33] Svelle, S.; Arstad, B.; Kolboe, S.; Swang, O. *J. Phys. Chem. B* **2003**, *107*, 9281–9289.

[34] Svelle, S.; Kolboe, S.; Swang, O.; Olsbye, U. *J. Phys. Chem. B* **2005**, *109*, 12874–12878.

[35] Svelle, S.; Kolboe, S.; Swang, O. *J. Phys. Chem. B* **2004**, *108*, 2953–2962.

[36] Engler, E. M.; Farcasiu, M.; Sevin, A.; Cense, J. M.; v. R. Schleyer, P. *J. Am. Chem. Soc.* **1973**, *95*, 5769–5771.

[37] Anderson, J. R.; Chang, Y.-F.; Western, R. J. *J. Catal.* **1990**, *124*, 259–267.

[38] Yuen, L.-T.; Zones, S. I.; Harris, T. V.; Gallegos, E. J.; Auroux, A. *Microporous Mater.* **1994**, *2*, 105–117.

[39] Dahl, I. M.; Mostad, H.; Akporiaye, D.; Wendelbo, R. *Microporous Mesoporous Mater.* **1999**, *29*, 185–190.

[40] Song, W.; Marcus, D. M.; Fu, H.; Ehresmann, J. O.; Haw, J. F. *J. Am. Chem. Soc.* **2002**, *124*, 3844–3845.

[41] Bjørgen, M.; Olsbye, U.; Kolboe, S. *J. Catal.* **2003**, *215*, 30–44.

[42] Bjørgen, M.; Olsbye, U.; Petersen, D.; Kolboe, S. *J. Catal.* **2004**, *221*, 1–10.

[43] World Wide Web page: http://www.chem.unl.edu/uic/gc-fid.html, (accessed November 2007).

[44] Harris, D. C. In *Quantitative chemical analysis*, 6th ed.; W. H. Freeman and Company, 2003; Chapter 24 - Gas Chromatography.

[45] World Wide Web page: http://www.mhhe.com/physsci/chemistry/carey/student/olc/ch13ms.html (accessed November 2007).

[46] Harris, D. C. In *Quantitative chemical analysis*, 6th ed.; W. H. Freeman and Company, 2003; Chapter 22 - Mass Spectroscpy.

[47] Jørgensen, S. KJM4010 - SEM module, UiO, Lecture Notes, spring 2007.

[48] *Handbook of analytical methods - Scanning electron microscopy*, World Wide Web page: http://www.mee-inc.com/sem.html (accessed November 2007).

[49] Moulijn, J.; Makkee, M.; van Diepen, A. *Chemical Process Technology*; John Wiley & Sons Ltd, 2001.

[50] Olsbye, U. KJM4800 - Petrochemistry, UiO, Lecture Notes, autumn 2006.

[51] World Wide Web page: http://en.wikipedia.org/wiki/Fluidized_bed_reactor, (accessed November 2007).

[52] Hanna, M. W. *Quantum mechanics in chemistry*; The Benjamin/Cummings Publishing Company, Inc., 1981.

[53] Jensen, F. In *Introduction to computational chemistry*; Wiley, 1999; Chapter 6.

[54] Kock, W.; Holthausen, M. C. In *A Chemist's Guide to Density Functional Theory*; Wiley-VCH, 2000; Chapter 5.

[55] Perdew, J. P.; Burke, K.; Ernzerhof, M. *Phys. Rev. Lett.* **1996**, *77*, 3865.

[56] Hammer, B.; Hansen, L. B.; Nørskov, J. K. *Phys. Rev. B* **1999**, *59*, 7413–7421.

[57] Cramer, C. J. In *Computational Chemistry, Theories and Models*, 2nd ed.; John Wiley & Sons, Ltd, 2006; Chapter 8, p 293.

[58] Groß, A. *Surf. Sci* **2002**, *500*, 347–367.

[59] Jacobsen, C. J. H.; ren Dahl, S.; Boisen, A.; Clausen, B. S.; e, H. T.; Logadottir, A.; rskov, J. K. N. *J. Catal.* **2002**, *205*, 382–387.

[60] Shah, R.; Gale, J. D.; Payne, M. C. *Chem. Commun.* **1997**, 131–132.

[61] Shah, R.; Gale, J. D.; Payne, M. C. *J. Phys. Chem.* **1996**, *100*, 11688–11697.

[62] Bučko, T.; Hafner, J.; Benco, L. *J. Phys. Chem. B* **2005**, *109*, 7345–7357.

[63] Robson, H.; Lillerud, K. P. In *Verified synthesis of zeolitic materials*, 2nd ed.; Elsevier, 2001; Chapter CHA, pp 123–131.

[64] Bordiga, S. Private communication.

[65] Yuen, L.-T.; Zones, S.; Harris, T.; Gallegos, E.; Auroux, A. *Microporous Mesoporous Mater.* **1994**, *2*, 105–117.

[66] Wilson, S.; Barger, P. *Microporous Mesoporous Mater.* **1999**, *29*, 117–126.

[67] Dahl, I. M.; Wendelbo, R.; Andersen, A.; Akporiaye, D.; Mostad, H.; Fuglerud, T. *Microporous Mesoporous Mater.* **1999**, *29*, 159–171.

[68] Delley, B. *J. Phys. Chem.* **1990**, *92*, 508–517.

[69] Greatbanks, S. P.; Hillier, I. H.; Burton, N. A.; Sherwood, P. *J. Phys. Chem.* **1996**, *105*, 3770–3776.

[70] Gale, J.; Shah, R.; Payne, M.; Stich, I.; Tekura, K. *Catalysis Today* **1999**, *50*, 525–532.

[71] Shah, R.; Payne, M. C.; Lee, M.-H.; Gale, J. D. *Science* **1996**, *271*, 1395–1397.